ÇUKUROVA UNIVERSITY
INSTITUTE OF NATURAL AND APPLIED SCIENCES

Ph.D. THESIS

Bülent YANIKTEPE

ORIGIN AND CONTROL OF VORTEX BREAKDOWN OF UNMANNED COMBAT AIR VEHICLES

DEPARTMENT OF MECHANICAL ENGINEERING

ADANA, 2006

ÇUKUROVA ÜNİVERSİTESİ
FEN BİLİMLERİ ENSTİTÜSÜ

ORIGIN AND CONTROL OF VORTEX BREAKDOWN OF UNMANNED COMBAT AIR VEHICLES

Bülent YANIKTEPE

DOKTORA TEZİ

MAKİNA MÜHENDİSİĞİ ANABİLİMDALI

Bu Tez …../…../2006 Tarihinde Aşağıdaki Jüri Üyeleri Tarafından Oybirliği/Oyçokluğu ile Kabul Edilmiştir.

İmza: ……	İmza:……	İmza…….
Prof. Dr. Beşir ŞAHİN	Doç.Dr.Ahmet PINARBAŞI	Doç. Dr. Hüseyin AKILLI
DANIŞMAN	ÜYE	ÜYE

İmza: ……	İmza: ……
Prof.Dr. Recep YURTAL	Yrd.Doç. Dr. Muammer ÖZGÖREN
ÜYE	ÜYE

Bu Tez Enstitümüz Makina Mühendisliği Anabilim Dalında Hazırlanmıştır.

Kod No:

Prof.Dr. Aziz ERTUNÇ
Enstitü Müdürü

Bu çalışma Çukurova Üniversitesi Bilimsel Araştırma Projeleri Birimi tarafından desteklenmiştir. Proje No:FBE.2002.D181.

Not: Bu tezde kullanılan özgün ve başka kaynaktan yapılan bildirişlerin, çizelge, şekil ve fotoğrafların kaynak gösterilmeden kullanımı, 5486 sayılı Fikir ve Sanat Eserleri Kanunundaki Hükümlere tabidir.

ABSTRACT

Ph.D.THESIS

ORIGIN AND CONTROL OF VORTEX BREAKDOWN OF UNMANNED COMBAT AIR VEHICLES

Bülent YANIKTEPE

DEPARTMENT OF MECHANICAL ENGINEERING
INSTITUTE OF NATURAL AND APPLIED SCIENCES
UNIVERSITY OF ÇUKUROVA

Supervisor : Prof. Dr. Beşir ŞAHİN
Year : 2006, Pages:129
Jury : Prof. Dr. Beşir ŞAHİN
Assoc. Prof. Dr. Ahmet PINARBAŞI
Assoc. Prof. Dr. Hüseyin AKILLI
Prof. Dr. Recep YURTAL
Assist. Prof. Dr. Muammer ÖZGÖREN

The instantaneous and averaged flow structures past a delta wing of low sweep angle are investigated using a technique of high-image-density particle image velocimetry. Three different UCAV planforms have been used. The UCAV planforms were subjected to static variations of angle-of-attack, with the aim of understanding the underlying flow physics and methods for their control. It was also subjected to perturbations for the case of basic delta wing in order to control the vortex breakdown or stall phenomenon.

At all values of angle-of-attack up to the fully stalled condition for the basic delta wing, the averaged vorticity layer exhibits an elongated form; a large-scale concentration of vorticity within the leading-edge vortex of a highly swept wing is not present. At low angle-of-attack α, this elongated, averaged layer can exhibit, however, well-defined concentrations of vorticity. These elongated vorticity layers are accompanied by narrow recirculation zones adjacent to the wing surface. Control in the form of a small amplitude perturbation of the basic wing, at a frequency corresponding to the subharmonic of the spectral component in the initial region of development of the separated layer, can restabilize the time-averaged patterns of streamline topology and vorticity, such that they resemble those occurring at lower angle-of-attack α.

Elongated layers of vorticity in the crossflow plane exhibit well-defined time-averaged and instantaneous concentrations of vorticity for the case of diamond and lambda planforms. Flow features are interpreted in conjunction with patterns of streamline topology, as well as images of root-mean-square velocity fluctuation and velocity spectra obtained from space-time imaging.

Keywords: UCAV, Delta Wing, PIV, Vorticity, Turbulent Flow

ÖZ

DOKTORA TEZİ

İNSANSIZ KEŞİF UÇAKLARDA GİRDAP ÇÖKMESİ VE KONTROLÜ

Bülent YANIKTEPE

ÇUKUROVA ÜNİVERSİTESİ
FEN BİLİMLERİ ENSTİTÜSÜ
MAKİNA MÜHENDİSLİĞİ ANABİLİM DALI

Danışman : Prof. Dr. Beşir ŞAHİN
Yıl : 2006, Pages:129
Jüri : Prof. Dr. Beşir ŞAHİN
Doç. Dr. Ahmet PINARBAŞI
Doç. Dr. Hüseyin AKILLI
Prof. Dr. Recep YURTAL
Yrd. Doç. Dr. Muammer ÖZGÖREN

Parçacık görüntülemeli hız ölçme tekniği (PIV) kullanılarak düşük süpürme açısına sahip bir delta kanat üzerindeki anlık ve ortalama akış yapısı incelenmiştir. Üç farklı insansız keşif uçak gövde modeli kullanılmıştır. Bu çalışmada (UCAV) modeller statik konumda tutularak değişik akış hücum açılarında akışın fiziğinin anlaşılması ve akış kontrol yöntemlerinin belirlenmesi amaçlanmıştır. Girdap çökmesi ve ayrılmış akış durumlarını kontrol etmek için temel delta kanada salınım hareketi verilmiştir.

Tamamen ayrılmış akışın oluştuğu hücum açılarında delta kanat için ortalama girdap tabakası uzamış bir durum sergilemektedir. Yüksek süpürme açısına sahip bir kanatta hücum kenarının oluşturduğu girdap akış alanında yüksek yoğunluklu tekil girdaplara rastlanmamıştır. Düşük hücum açılarında, kanadın eni doğrultusunda uzayan zaman ortalama girdap tabakası oluşmakla birlikte girdap yoğunluğu daha belirgin görülmektedir. Kanadın eni doğrultusunda uzamış girdap tabakaları kanat yüzeyinin yakınlarında dar dönüşümlü bölgeler oluşturmaktadır. Delta kanada, düşük genlikde ve girdapların doğal frekans katlarında sinüzoidal salınım hareketi verilerek, ayrılma yüzeyinin gelişmesindeki ilk bölgede akış yapısının kararlı hale geldiği gözlenmiştir. Bu salınım sayesinde yüksek hücum açısında oluşan akış yapısı düşük hücum açısında oluşan akış yapısına benzemektedir.

Baklava biçimi ve lamda modellerinde, akış düzlemindeki uzamış girdap tabakaları, zaman ortalama ve anlık girdap oluşumları daha belirgin bir şekilde görülmektedir. Akış özellikleri, anlık görüntülerden elde edilen hız spektralarına, hız çalkantılarının karelerinin kare köküne ve akım çizgileri dağılımlarına bakılarak yorumlanmıştır.

Anahtar Kelimeler: İnsansız Keşif Uçak, Delta Kanat, PIV, Girdap, Türbülanslı Akış

TEŞEKKÜR

"İnsansız Keşif Uçaklarda Girdap Çökmesi ve Kontrolü" konulu doktora tezimde yapılan çalışmaların her aşamasında bilimsel katkıları ile bana samimi yardım ve desteği için danışman hocam Sayın Prof. Dr. Beşir ŞAHİN'e en derin saygılarımı ve içten teşekkürlerimi ifade etmek isterim. Beyin göçünü önlemek ve ülkemizdeki genç bilimadamlarının yetişmesine, PIV deney düzeneğini Çukurova Üniversitesine kurarak vesilede olduğu için danışman hocam Sayın Prof. Dr. Beşir ŞAHİN'e ayrıca teşekkür etmek isterim.

Araştırma süresince büyük yardımlarını gördüğüm, bilgi ve deneyimlerinden yararlandığım Doç Dr. Hüseyin AKILLI ve Yrd. Doç. Dr. Muammer ÖZGÖREN'e en derin sevgi ve saygılarımı ifade etmek isterim.

Çalışma sırasında motivasyon, destek ve yardımlarından dolayı jüri üyelerim Doç. Dr. Ahmet PINARBAŞI ve Prof. Dr. Recep YURTAL'a teşekkür ediyorum.

Amerika Birleşik Devletleri, Lehigh Üniversitesi Makine Mühendisliği ve Mekanik Bölümü Akışkanlar Mekaniği Laboratuarında doktora tezimi gerçekleştirebilme fırsatını bana sağladığı için, finansal desteklerinden dolayı tecrübe ve bilgilerinden yararlandığım Prof. Dr. D. ROCKWELL'e teşekkür ederim.

Ayrıca, Amerila Birleşik Devletlerinde göstermiş oldukları arkadaşlık yanlısı tutumlarından ve sürekli moral desteklerinden dolayı Yrd. Doç. Dr. Ali KAHRAMAN, Dr. M.M. YAVUZ, Dr. M. ELKHOURY, Ç. SEVER, ve Dr. E. ÇELİK' e ayrıca teşekkür ederim.

Çukurova Üniversitesi Mühendislik Mimarlık Fakültesi Makine, Mühendisliği Bölümü tüm akademik ve idari görevlilerine, ayrıca maddi manevi desteklerini hiçbir zaman esirgemeyen Makine Mühendisi Sami AKBAY, Araştırma Görevlisi İbrahim Ö. Deneme, Yrd. Doç Dr. Metin Hakan SEVERCAN ve İnşaat Mühendisi Kubilay AKÇAÖZOĞLU'na sonsuz teşekkürlerimi ifade etmek isterim.

Yüksek Lisans ve doktora süresince ev arkadaşlığını yaptığım, hayatımın en yoğun iş dönemlerinde tezimin başlangıcından yazım aşamasına kadar doktora öğrenimimin her aşamasında bana yardımını esirgemeyen, mutluluğu, üzüntüyü ve

güzel günleri paylaştığım değerli arkadaşım Dr. Coşkun ÖZALP'e sonsuz teşekkürlerimi sunarım.

Hayatımın en zor anlarında desteklerini daima yanımda bulduğum, maddi ve manevi her türlü desteğini asla benden esirgemeyen ağbim Mustafa ve eşi Ayşegül YANIKTEPE'ye, eniştem Ökkeş ve eşi F. Filiz ÖZDEMİR'e ve tabiki ellerinden öpülesi annem Neziha YANIKTEPE'ye en içten teşekkürlerimi ve şükranlarımı sunarım.

Doktora çalışmam süresince yurtdışında kendisinden ayrı kaldığım zamanlarda benden ayrı kalmak pahasına beni sabırla bekleyip bana sevgi, anlayış ve cesaret dolu desteklerinden dolayı eşim Ayşe YANIKTEPE'ye, hayatımın sevgi kaynakları kızım Neziha ve oğlum Mustafa KAAN YANIKTEPE'ye en içten dileklerimi ifade etmek isterim.

Sonuç olarak, bölgesinde lider ülke olmak isteyen Ülkemize bu çalışmanın faydalı olmasını temenni ediyorum.

NOMENCLATURE

C = Root chord (mm)

C' = Root chord of leading (delta wing) portion of planform (mm)

f = Frequency (Hz)

f_o = Frequency of spectral peak of velocity fluctuation (Hz)

S = Local semi-span of wing (mm)

S_w = Spectrum of w component of velocity fluctuation

T = Period of perturbed angle-of-attack α (degrees)

U = Freestream velocity (mm/sec)

v' = Instantaneous velocity fluctuation in direction parallel to surface of wing (mm/sec)

V = Magnitude of velocity vector (mm/sec)

w' = Instantaneous velocity fluctuation normal to surface of wing (mm/sec)

w_{rms} = Root-mean-square of velocity fluctuation (mm/sec)

x = Distance from apex measured along plane of symmetry of wing (mm)

x_b' = Distance from apex measured along axis of leading-edge vortex (mm)

y = Distance from apex measured normal to plane of symmetry of wing (mm)

$< >$ = Time-averaged value of quantity

α = Angle-of-attack (degrees)

$\Delta\alpha$ = Perturbation of angle-of-attack α (degrees)

Greek Symbols

λ = Wavelength between vorticity concentrations (mm)

Λ = Sweep angle (degrees)

ψ = Stream function (mm^2/s)

ω = Vorticity (1/sec)

Operators

$\langle . \rangle$:Time-averaging

~ :Fluctuations

TABLE OF CONTENTS Page

ABSTRACT…… I

ÖZ..... II

TEŞEKKÜR…… III

NOMENCLATURE…… V

TABLE OF CONTENTS……..…….. VII

LIST OF FIGURES……...…….. X

1. INTRODUCTION……...…….. 1

2. LITERATURE SURVEY AND OUTLINE OF PRESENT STUDY... 10

2.1. Unsteady Loading of Aerodynamic Surface…… 10

2.2. Models of Buffet-Loading of Aerodynamic Surface…… 19

2.3. Global, Instantaneous Flow Patterns: Relation to Motion and Loading of Aerodynamic Surfaces……. 21

2.4. Control / Attenuation of Buffeting of Aerodynamic Surfaces……..... 23

2.5. Buffet-Induced Loading on the Basis of Unsteady Flow Patterns……... 30

2.6. Small-Scale Patterns of Flow Structure Including Highly Sweep Wings……. 31

2.7. Flow Structure on Delta Wings of Moderate and Low Sweep Angle…….. 33

2.8. Unresolved Issues …… 35

2.9. Objectives of Present Investigation……..... 37

2.10. Outline of Dissertation……... 39

3. EXPERIMENTAL SYSTEM AND TECHNIQUES……..... 40

3.1. Measurement Techniques…… 40

3.1.1. Overview of Correlation Process…… 41

3.2. Experimental Arrangement…… 42

3.2.1. Water Channel System……. 42
3.2.2. Experimental System……... 44
3.3. Image Acquisition…… 52
4. RESULT AND DISCUSSIONS……..... 55
4.1. Flow Structure on a Delta Wing of Low Sweep Angle……..... 55
4.1.1. Dye Visualization……. 55
4.1.2. Averaged Velocity and Streamline Topology……. 58
4.1.3. Patterns of Averaged Vorticity and Fluctuating Velocity…… 59
4.1.4. Instantaneous Patterns of Vorticity…….. 61
4.1.5. Spectra Along Separated Vorticity Layer…… 63
4.1.6. Effect of Controlled Perturbations on Averaged and Instantaneous Structure……. 65
4.2. Flow Structure on Diamond and Lambda Planforms: Trailing Edge-Region……. 76
4.2.1. Dye Visualization of Flow Patterns……. 76
4.2.2. Patterns of Averaged Velocity and Streamline Topology…….. 78
4.2.3. Patterns of Averaged Vorticity and Fluctuating Velocity…… 80
4.2.4. Patterns of Averaged Vorticity and Streamline Topology: A Comparison……. 82
4.2.5. Patterns of Instantaneous Vorticity…….. 82
4.2.6. Spectra of Fluctuating Velocity……... 83
4.3. The Effect of Reynolds Number on the Vortex Breakdown Location…….. 96
5. CONCLUSIONS AND RECOMMENDATIONS…….……..…….. 102
5.1. Summary of Primary Findings……... 102
5.1.1. Flow Structure on a Delta Wing of Low Sweep Angle…… 102

5.1.2. Flow Structure on Diamond and Lambda Planforms: Trailing - Edge Region……..... 104
5.2. Suggestions for Future Studies……... 105
REFERENCES…… 107
CIRRICULUM VITAE……... 119
APPENDIX A: Vorticity Evaluation.....…….. 120
APPENDIX B: Bilinear Interpolation……...…….. 122
Gaussian Smoothing……... 123
APPENDIX C: Averaged Flow Structure……...…… 124
APPENDIX D: Spectral Analysis……...…….…….... 126

LIST OF FIGURES Page

Figure 1.1.	Types of vortex breakdown in a tube……..	2
Figure 1.2.	a) Symmetrical vortex breakdown over a delta wing b)Vortex breakdown flow visualization around NASA's F-18 High Angle of Attack Research Vehicle (HARV) using smoke to seed the vortex emanating from the nose of the aircraft at $\alpha=20^0$ incidence……	3
Figure 1.3.	Different types of UCAV planforms with small sweep angle are shown……	8
Figure 2.1.1.	Schematic of simple delta wing showing onset of vortex breakdown and stall…….....	10
Figure 2.1.2.	Generic trailing edge configurations of UCAV planforms alteration due to fuselage/forebody….....	11
Figure 2.1.3.	Delta Wing Flowfield……..	15
Figure 2.4.1.	The effect of different flow control techniques (a) Obstacle downstream b) Suction c) Blowing opposite the axial velocity of the vortex core d) along the core blowing Werle (1960).……..	27
Figure 3.2.1.	Schematic of the water channel with experimental apparatus…….....	43
Figure 3.2.2.	Generic planforms of Unmanned Combat Air Vehicles showing basic classes of trailing edge configurations alteration due to fuselage/forebody…….	45
Figure 3.2.3.	Instrumentation and test chamber……...	46
Figure 3.2.4.	Schematic of experimental arrangement showing delta wing, laser sheet location, and definition of key parameters……...	48

Figure 3.2.5. Simplified schematic of experimental arrangement of diamond planform……... 49

Figure 3.2.6. Direct comparison of diamond and lambda planforms and locations of laser sheets employed for quantitative imaging…… 50

Figure 4.1.1. Dye visualization at three representative angles-of-attack. For images α = 7° and 13°, dye is injected through two discrete ports at the apex of the wing, while at α = 17°, dye is injected along the leading-edge on the windward side of the wing. For the perturbed wing, the perturbation amplitude and period are α_o = 1° and T = 0.5 sec……..... 56

Figure 4.1.2. Comparison of dye visualization of Yaniktepe and Rockwell (2004) and the computational streakline of Gordnier and Visbal (2003)…… 57

Figure 4.1.3. Patterns of averaged velocity $< V >$ and streamline $< \Psi >$ topology at four values of angle-of-attack α = 7°, 13°, 17° and 25°. Laser sheet is located at *x/C* = 0.8. Spanwise extent of wing corresponds to 0.82 *S* at α = 7° and 13° and 0.94 S at α = 17° and 25°, in which *S* is the semi-span of the delta wing at the location of the laser sheet, *x/C* = 0.8…… 68

Figure 4.1.4. Patterns of averaged vorticity $< \omega >$, contours of constant vertical (transverse) velocity fluctuation w_{rms}/U and Reynolds stress correlation $< v'w' > / U^2$. Angles-of-attack are α = 7°, 13°, 17° and 25°. Laser sheet is located at x/C = 0.8. For contours of averaged vorticity, minimum and incremental values are $[< \omega >]_{min}$ = –0.3 sec^{-1} and $\Delta[< \omega >]$ = –0.15 sec^{-1}. For contours of constant velocity fluctuation, are $[w_{rms}/U]_{min}$ = 0.025 and

$\Delta[w_{rms}/U]$ = 0.005. For contours of constant Reynolds stress correlation, $[<v'w'>/U^2]_{min}$ = –0.0004 and $\Delta[<v'w'>/U^2]$ = –0.0002. Spanwise extent of wing corresponds to 1.0 *S*, in which *S* is the semi-span of the delta wing at the location of the laser sheet *x/C* = 0.8……. 69

Figure 4.1.5. Patterns of instantaneous vorticity ω at two randomly selected instants from a cinema sequence. Angles-of-attack are α = 7°, 13°, 17° and 25°. Minimum and incremental values are ω_{min} = –1.5 sec^{-1} and $\Delta\omega$ = –0.25 sec^{-1}. Spanwise extent of wing corresponds to 1.0 *S*, in which *S* is the semi-span of the delta wing at the location of the laser sheet *x/C* = 0.8……..... 70

Figure 4.1.6. Spectra S_w of velocity fluctuation at selected locations in separated shear layer. Each spectrum is referenced to the indicated location in the pattern of constant contours of w_{rms}/U. Parameters for these contour levels are given in Figure 4. Spanwise extent of wing corresponds to 1.0 *S*, in which *S* is the semi-span of the delta wing at the location of the laser sheet, *x/C* = 0.8…….... 71

Figure 4.1.7. Effect of small perturbations of wing on time-averaged patterns of velocity $<V>$ and streamlines $<\Psi>$, relative to the case of he stationary wing. Perturbation amplitude is α_o = 1° and mean angle-of-attack is $\overline{\alpha}$ = 17°. Perturbation is applied according to $\alpha(t) = \overline{\alpha} + \alpha_o \sin(2\pi t/T)$. Values of perturbation period *T* are *T* = 0.5, 1.0 and 1.5 sec. Spanwise extent of wing corresponds to 1.0 *S*, in which *S* is the semi-span of the delta wing at the location of the laser sheet, *x/C* = 0.8…..... 72

Figure 4.1.8. Consequence of small-amplitude perturbation on patterns of averaged vorticity $< \omega >$, root-mean-square of vertical (transverse) velocity fluctuation w_{rms}/U and Reynolds stress correlation $< v'w' > / U^2$. For patterns of vorticity, $< \omega >_{min}$ = –0.4 sec^{-1} and $\Delta[< \omega >]$ = –0.2 sec^{-1}. For contours of constant w_{rms}/U, $[w_{rms}/U]_{min}$ = 0.04 and $\Delta[w_{rms}/U]$ = 0.01. For contours of constant Reynolds stress correlation, $[< v'w' > / U^2]_{min}$ = –0.001 and $\Delta[< v'w' > / U^2]$ = –0.0005. Spanwise extent of wing corresponds to 1.0 *S*, in which *S* is the semi-span of the delta wing at the location of the laser sheet *x/C* = 0.8……. 73

Figure 4.1.9. Comparison of representative patterns of instantaneous vorticity ω for the stationary wing and the wing subjected to small amplitude perturbations according to $\alpha(t) = \bar{\alpha}$ sine (ωt) in which $\bar{\alpha}$ = 17°, α_o = 1° and $\omega = 2\pi t/T$. Minimum and incremental values of vorticity are ω_{min} = –1.5 sec^{-1} and $\Delta\omega$ = –0.25 sec^{-1}. Spanwise extent of wing corresponds to 1.0 *S*, in which *S* is the semi-span of the delta wing at the location of the laser sheet *x/C* = 0.8... 74

Figure 4.1.10. Flow visualization for a stationary and small amplitude ($\Delta\alpha$ = 1^o) pitching wing for various reduced frequencies fC/U, α = 25^o, Λ=50^o (Gursul et al. (2005))…….... 75

Figure 4.2.1. Dye visualization at angles-of-attack α = 7° and 13°. At α = 7°, dye is injected from two localized ports at the apex of the wing, while at α = 13°, it is injected along the leading-edge on the windward side……. 77

Figure 4.2.2. Patterns of time-averaged velocity $< V >$ at α = 7°, 13°, 17° and 25°. For both the diamond and lambda planforms, laser sheet is located at x/C' = 1.4,

immediately downstream of abrupt change of sweep angle. Scale shown above planform cross-section is y/S, in which y/S = 1.0 corresponds to plane of symmetry of wing; S is the semi-span at $x/C' = 1.4$…….. 86

Figure 4.2.3. Patterns of time-averaged streamline $< \Psi >$ topology at angles-of-attack $\alpha = 7°$, 13°, 17° and 25° for the diamond and lambda planforms. For both planforms, the laser sheet is located at $x/C' = 1.4$, immediately downstream of abrupt change of sweep angle. Spanwise extent of each planform cross-section is same as in Figure 4.2.2…..
87

Figure 4.2.4a. Patterns of time-averaged vorticity $< \omega >$ and corresponding patterns of root-mean-square velocity fluctuation w_{rms}/U (normal to the wing). At angle-of-attack $\alpha = 7°$, minimum and incremental values of vorticity contours are $[< \omega >]_{min} = -0.2\ sec^{-1}$ and $\Delta[< \omega >] = -0.15\ sec^{-1}$. At $\alpha = 13°$, $[< \omega >]_{min} = -0.35\ sec^{-1}$ and $\Delta[< \omega >] = -0.15\ sec^{-1}$. For patterns of root-mean-square velocity, minimum and incremental values at $\alpha = 7°$ are $[w_{rms}/U]_{min} = 0.02$ and $\Delta[w_{rms}/U] = 0.01$. For $\alpha = 13°$, $[w_{rms}/U]_{min} = 0.04$ and $\Delta[w_{rms}/U] = 0.01$. For both the diamond and lambda planforms, laser sheet is located at $x/C' = 1.4$, immediately downstream of abrupt change of sweep angle. In each image, spanwise extent of planform cross-section corresponds to the semi-span S of the wing at $x/C' = 1.4$…… 88

Figure 4.2.4b. Patterns of time-averaged vorticity $< \omega >$ and corresponding patterns of root-mean-square velocity fluctuation w_{rms}/U (normal to the wing). At angle-of-attack $\alpha = 17°$, minimum and incremental values of

vorticity contours are $[<\omega>]_{min} = -0.35$ sec^{-1} and $\Delta[<\omega>] = -0.15$ sec^{-1}. At $\alpha = 25°$, $[<\omega>]_{min} = -0.2$ sec^{-1} and $\Delta[<\omega>] = -0.15$ sec^{-1}. For contours of root-mean-square vertical velocity, at $\alpha = 17°$, $[w_{rms}/U]_{min} = 0.03$ and $\Delta[w_{rms}/U] = 0.01$. For $\alpha = 25°$, $[w_{rms}/U]_{min} = 0.02$ and $\Delta[w_{rms}/U] = 0.01$. For both the diamond and lambda planforms, laser sheet is located at $x/C' = 1.4$, immediately downstream of abrupt change of sweep angle. In each image, spanwise extent of planform cross-section corresponds to the semi-span S of the wing at $x/C' = 1.4$…….. 89

Figure 4.2.5. Superposition of patterns of averaged vorticity $<\omega>$ and streamline $<\Psi>$ topology at $\alpha = 17°$ for the diamond and lambda planforms. The laser sheet is located at $x/C' = 1.4$……. 90

Figure 4.2.6. Comparison of patterns of instantaneous velocity V and vorticity ω at angles-of-attack $\alpha = 7°$ and 25° for the diamond planform. At $\alpha = 7°$, minimum and incremental values of vorticity are $\omega_{min} = -1.5$ sec^{-1} and $\Delta\omega = -0.5$ sec^{-1}. At $\alpha = 25°$, minimum and incremental values of vorticity are $\omega_{min} = -0.5$ sec^{-1} and $\Delta\omega = -0.5$ sec^{-1}. For both the diamond and lambda planforms, laser sheet is located at $x/C' = 1.4$, immediately downstream of abrupt change of sweep angle. Spanwise extent of each planform cross-section extends from y/S = 0 to 0.62 (α = 7º) and to 1.0 (α = 25º)…… 91

Figure 4.2.7a. Patterns of instantaneous vorticity ω at angles-of-attack α = 7° and 13° for the diamond and lambda planforms. At α = 7º, values of minimum and incremental levels of

vorticity are $\omega_{min} = -1.5$ sec^{-1} and $\Delta\omega = -0.5$ sec^{-1}. At α = 13º, values of minimum and incremental levels of vorticity are $\omega_{min} = -0.5$ sec^{-1} and $\Delta\omega = -0.5$ sec^{-1}. For both the diamond and lambda planforms, laser sheet is located at $x/C' = 1.4$, immediately downstream of abrupt change of sweep angle. At α = 7º (diamond and lambda planforms), spanwise extent of planform cross-section extends from y/S = 0 (leading-edge) to y/S = 0.62. For all other images, it extends from y/S = 0 to y/S = 1.0, where S is the semi-span at $x/C' = 1.4$…… 92

Figure 4.2.7b. Patterns of instantaneous vorticity ω at angles-of-attack α = 17° and 25° for the diamond and lambda planforms. Values of minimum and incremental levels of vorticity are $\omega_{min} = -0.5$ sec^{-1} and $\Delta\omega = -0.5$ sec^{-1}. For both the diamond and lambda planforms, laser sheet is located at $x/C' = 1.4$, immediately downstream of abrupt change of sweep angle……. 93

Figure 4.2.8. Spectra $S_w(f)$ of the vertical velocity fluctuation w at locations corresponding to maxima of the root-mean-square value of the transverse (vertical) velocity fluctuation w_{rms}/U at angles-of-attack α = 7° and 25° for the diamond and lambda planforms. The laser sheet is located at $x/C' = 1.4$…….. 94

Figure 4.2.9. Global representations of peak spectral amplitude $<S_w(f_o)>$ at α = 7°. The laser sheet is located at $x/C' = 1.4$. for the diamond planforms…….. 95

Figure 4.3.1. Flow visualization at angle-of-attack, $\alpha = 7^o$, Re = 5 000 ~12 5000…….. 99

Figure 4.3.2. Strake and wing vortex core trajectories at angle-of-attack, α = 10 and Re = 15000, 45 000, 75 000 (from

Hebbar et al. (2000))…….. 100

Figure 4.3.3. Extremes of vortex breakdown location Λ= 50 deg. wing at α = 7.5 deg. for selected numbers (from Ref. Taylor et al. (2003))…… 101

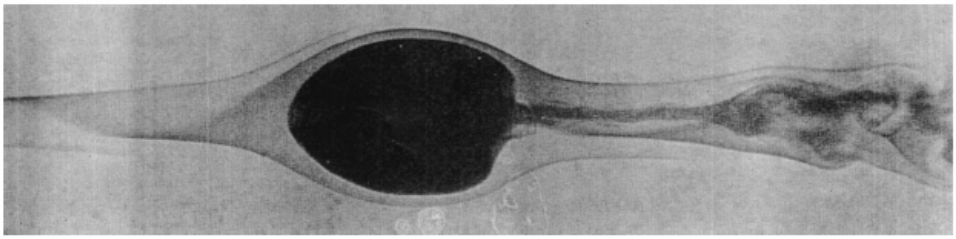
1. INTRODUCTION

Aircraft maneuverability is the key element in the successful missions accomplishment of a combat aircraft. Delta wing vortex dynamics and the effects on aircraft performance have become an important role. Several variables influence delta wing vortex dynamics. Some of these variables include angle-of-attack, leading edge geometry, wing thickness, sweep angle, free stream conditions and Reynolds number. Reynolds number depending on the delta wing geometry has to be defined more precisely due to the effect of vortex breakdown location.

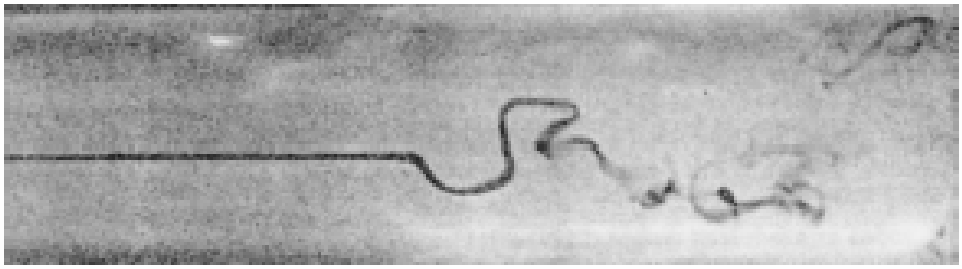
A phenomenon of more importance to vortical flows is vortex breakdown. The flow over delta wing is just one example of a flow where vortex breakdown is observed. Lambourne and Bryer (1961) showed that two unique types of vortex breakdown were observed over a delta wing, the spiral and the bubble, as shown in Figure 1.1 (Sarpkaya, 1971a). Experimental studies were performed by Sarpkaya (1971a) which identified the existence of multiple types of breakdown of columnar vortices as well as an inexplicable shift from one mode to another, the breakdown may move from one type to another, e.g. from a spiral to a bubble and then back to spiral. Based on his study of swirling flow in a tube, Sarpkaya (1971a) classified three types of vortex breakdown, the bubble, the spiral, and the double helix. Upon revisiting the subject, on the same experimental apparatus, Sarpkaya (1995) has developed the investigation and added a fourth type vortex breakdown form, which he defined this type as conical vortex breakdown. The four types of vortex breakdown as defined by Sarpkaya are shown in Figure 1.1. Faler and Leibovich (1978) and Leibovich (1978) indicated that the flow in the breakdown region of a columnar vortex to have a strong dominant frequency using one-dimensional Laser Doppler Velocimetry (LDV). Faler and Leibovich (1978), has developed new insight on the vortex breakdown phenomenon, using an apparatus identical to that Sarpkaya (1971a) added two other classifications to include some of the transients forms, bringing the total number of vortex breakdown types of six.

Of all these, most frequently investigations were carried out for the case of swirling flows in tubes, and most often emulated by theoreticians. Detailed reviews

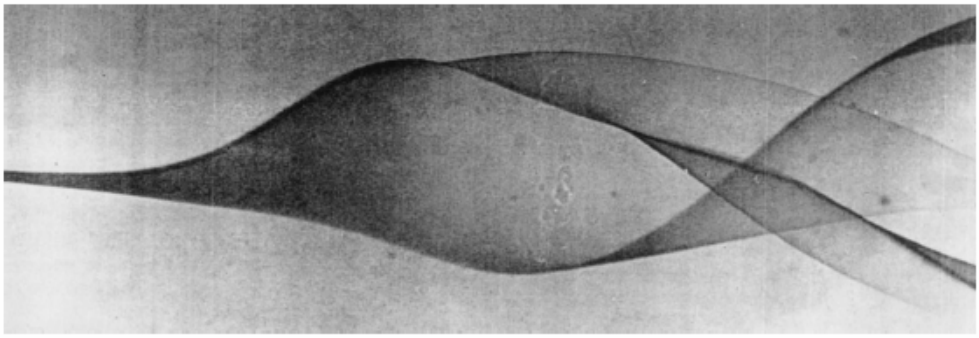
of Leibovich (1984) and Escudier (1988) described the experimental studies of columnar vortex breakdown



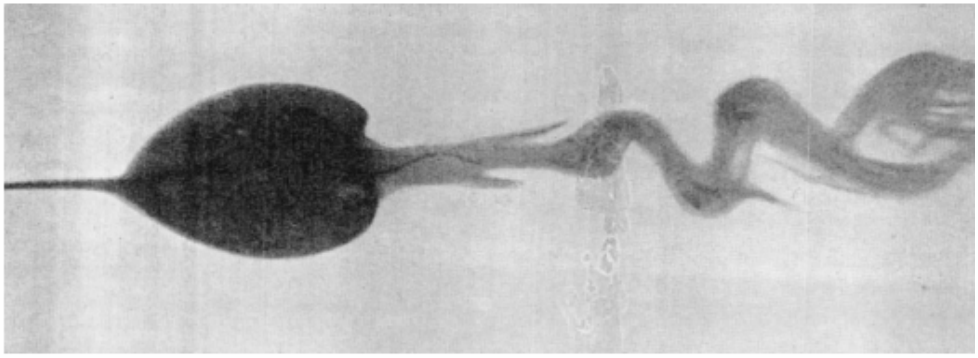
a) Bubble type breakdown



b) Spiral type breakdown



c) Double helix breakdown



d) Bubble breakdown followed by a spiraling tail

Figure 1.1 Types of vortex breakdown in a tube

Vortex breakdown phenomenon is the most important source of buffeting causing large structural vibrations and severe fatigue damage. General view of vortex breakdown over a delta wing is shown in Figure 1.2. It has long been recognized that high angle-of-attack aerodynamics is a key element in airplane design.

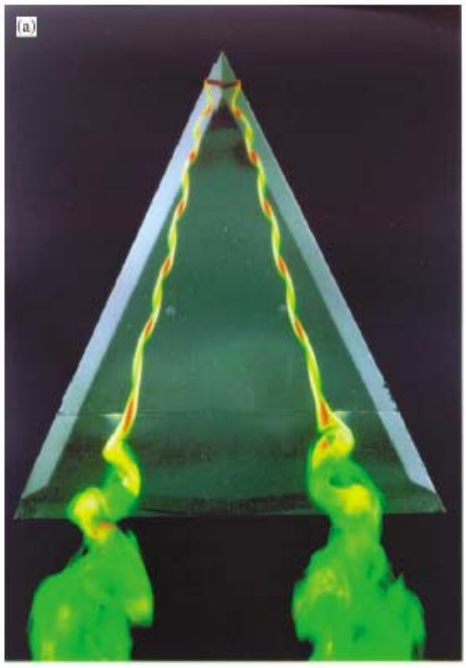




Figure 1.2. a) Symmetrical vortex breakdown over a delta wing b)Vortex breakdown flow visualization around NASA's F-18 High Angle of Attack Research Vehicle (HARV) using smoke to seed the vortex emanating from the nose of the aircraft at $\alpha=20^0$ incidence.

Vortex breakdown is also observed in swirling flows in tubes (Sarpkaya, 1971a, 1995), in tornado-like flows, free swirling jets, in trailing vortex systems, in rotors and in combustion chambers (Visbal, 1995).

Rockwell (1998) has recently assessed the flow physics associated with unsteady loading of aerodynamic surfaces and related configurations. Buffet loading can arise from vortex breakdown, shear layer instabilities from a leading- edge, and stall on an aerodynamic surface at high angle-of-attack. Lee (2000) provided a review of models of buffet loading and response of aircraft wings and tails/fins. Representative characterizations of unsteady surface pressure fluctuations on wings, primarily associated with vortex breakdown, are provided by, for example, Mabey (1973), Roos and Kegelman (1990) and Menke and Gursul (1997). Certain aspects of the unsteady loading of wing surfaces have analogies with the buffet loading of tails, fins, and plates, also reviewed by Rockwell (1998) and Lee (2000), and simulated numerically by Gordnier andVisbal (1997).

As always, the vortex breakdown phenomenon can be beneficial or detrimental, depending on the required applications. For beneficial applications, where one tries to destroy hazardous vortices such as those emanating from the tip of the large transport aircraft, or enhancing fuel–air mixing in a combustion chamber. Rockwell (1998) examined the-vortex body interactions. He assessed that substantial unsteady loading, sound generation and vibration in a variety of engineering applications can occur due to the affect of vortices incident upon bodies, more specifically cylinders, foils, fins, corners of cavities or protrusions. Some of engineering applications are tubes in energy conversion systems, helicopter blades, tails of aircraft, and combustion systems in aeronautics.

The rapid swirling motion of the vortices over a delta wing at high incidences induces a depression on the wing surface, producing important additional lift. However, most consider vortices forming on the system to be detrimental because they are inducing a performance loss. On the other hand, the breakdown of the vortices over the highly swept wings of a combat aircraft maneuvering at high incidence has been identified as a source of performance loss (reduced lift) and dangerous vibrations.

The significant problems due to the vortices formed are classified as given below;

a)Intense noise production at high speed

b)Uncontrollability of trailing aircraft during take off or landing

c)Heightened structural fatigue failure because of the effect of strong pressure fluctuations.

In addition, since breakdown rarely occurs symmetrically over each wing, the difference in lift loss can induce a roll moment compromising aircraft stability. Vortex breakdown can also affect the vortices forming on the fuselage, nose and/or canards of combat aircraft at very high incidence thus creating an unwanted roll moment or side force. These same consequences of vortex breakdown can also have a positive aspect since by provoking an asymmetric breakdown it should be possible, in principle, to increase the maneuvering speed of a combat aircraft (Mitchell, M. A., and Delery, J. (2001)).

Vortex breakdown is also of some concern in internal aerodynamics where the breakdown of a vortex swallowed by an air-intake can provoke strong flow distortion and unsteadiness detrimental to the engine. Whatever the objectives and the situations, it soon appeared profitable to control the vortex breakdown of very intense vortices, either to avoid or delay the phenomenon.

In aeronautics, leading-edge vortices shed from a delta wing induce a velocity field that results in increased lift and stability of the wing. However, under certain conditions related to the angle of attack of the wing, these vortices can undergo a sudden and drastic change in structure, which can adversely alter the aerodynamic characteristics of the wing. A similar bursting phenomenon has been observed for trailing wing-tip vortices, which is, this time, desirable as these vortices represent a hazard to smaller aircraft in areas of dense air traffic.

Swirling flows are observed in natural flows, such as tornadoes and typhoons, and have been widely used, for many years, in technical applications, such as aeronautics, heat exchange, spray drying, separation, combustion, etc. Their importance and complexity have preoccupied research investigations for decades. In combustion systems, such as in gas turbine engines, diesel engines, industrial

burners, and boilers, swirling flows were originally used to improve and control the mixing rate between fuel and oxidant streams in order to achieve flame geometries and heat release rates appropriate to the particular process application (Weber et al. (1986)). At sufficient degree of swirl, an internal recirculation zone is generated, which allows high rate of heat release, as products of combustion are recirculated and ignite the incoming fuel/oxidant streams. This provides a stable, compact flame (Swithhenbank J and Chigier NA (1969)), with a good performance for difficult carboneous materials and poor quality gases (Syred N and Beer JM (1974)).

One important feature of swirling flows was put forward by Ranque GJ (1933) who discovered the ability of vortex tubes to separate compressed air into hot and cold air streams, located near the periphery and the tube centreline, respectively. This has resulted in a large number of engineering applications utilising this flow behaviour, such as separation of gases of different molecular weight, Ranque-Hilsch vortex tube for a refrigeration scheme, cyclone separation, gas turbine cyclone, combustion chamber, and spray dryers. Despite its simplicity, the mechanism of the Ranque-Hilsch effect has been a matter of long-standing dispute. Swirl, defined as the ratio of the axial flux of momentum to the axial flux of axial momentum times the equivalent exit radius, has been shown to have large-scale effects on flow fields (Gupta et al. (1984)). Introducing swirl in turbulent jets causes an increase in jet growth, rate of entrainment and rate of decay of the jet. These effects increase with increasing level of swirl.

Vortex breakdown remains a significant and intriguing phenomenon that can have detrimental effects when it occurs over a highly swept or delta wing, in an air intake (ingestion of a vortex induced by a front lifting surface), or inside a turbo machine (vortices form at blade tips). However, there are circumstances where vortex breakdown can be beneficial; for example, they can be used as a way to promote the dissipation of the intense tip vortices of large transport aircraft, to stabilize the flame in a combustion chamber, or to increase the maneuvering capacity of a combat aircraft. Thus, there is a strong need to both better understand the phenomenon and to control it, either to prevent breakdown or to promote it. For the past 50 years, multiple flow control techniques have demonstrated the ability to

manipulate the vortex breakdown location over slender delta wings at high angles of attack. An extensive historical review of these diverse control methods, mechanical and pneumatic, has been presented and discussed; however, none of these techniques has clearly demonstrated a superior efficiency or effectiveness in controlling either the vortical flow structure or the vortex breakdown location. Each technique, does; on the other hand, provide a unique approach to the control of the vortex breakdown depending on the desired outcome (Mitchell, M. A., and Delery, J. (2001)).

An understanding of the vortical structures and vortex breakdown is essential for the development of highly maneuverable and high angle of attack flight. This is primarily due to the physical limits these phenomena impose on aircraft and missiles at extreme flight conditions.

The delta wing flow field is dominated by vortical structures, the most prominent called leading-edge vortices. As angle of attack increases, these leading-edge vortices experience a sudden disorganization, known as vortex breakdown which can be described by a rapid deceleration of both the axial and swirl components of the mean velocity and, at the same time, a dramatic expansion of the vortex core.

Unmanned Combat Air Vehicles (UCAVs) capable of undergoing severe maneuvers would be a major tactical advantage. Future configurations of the UCAVs are presented in Figure 1.3. The assumption is that the maneuverability of all these configurations will be limited by the onset of vortex breakdown and stall phenomenon, which, in turn, dictates both the overall forces and moments on the aircraft. Moreover, with the current trend towards lighter aircraft, an increasingly important limitation will be the onset of vibration and potential failure of aerodynamic surfaces of the UCAV arising from buffeting.



Figure 1.3. Different types of UCAV planforms with small sweep angle are shown.

In recent years, considerable insight has been gained into the averaged and unsteady structure on delta wings having relatively large sweep angle. In contrast to wings having relatively large sweep angle, which have been investigated extensively in the past, relatively little is known of the unsteady flow structure on wings with small sweep angle. Recent interest in unmanned combat air vehicles, i.e, UCAVs, has stimulated an interest in characterizing the flow structure on delta wings having

low and moderate values of sweep angle, as well as on planforms that represent the actual UCAV configuration or simplifications thereof.

The focus of the proposed investigation is the unsteady flow structure, which serves as an origin of buffeting in regions of vortex breakdown and stall, with emphasis on the configurations of UCAVs planforms. The flow structure on a delta wing of low sweep angle exhibits a number of distinctive characteristics, relative to the extensively investigated case of a slender, highly-swept delta wing. Emphasis in the present investigation has been on crossflow planes where vortex breakdown and stall phenomena occur; these phenomena are known to be important origins of unsteady buffet loading of the wing.

2. LITERATURE SURVEY AND OUTLINE OF PRESENT STUDY

2.1. Unsteady Loading of Aerodynamic Surface

The onset of vortex breakdown and stall phenomenon for all classes of aircraft, which are related to the overall forces and moments on the aircraft, can produce localized buffeting. Figure 2.1.1 shows the simplest case of a delta wing of relatively small sweep angle. The onset of vortex breakdown is indicated in an idealized fashion. Also illustrated is the occurrence of large-scale stall-like regions at the wing surface, which arise in regions between the leading-edge vortices at higher angles of attack. A summary of representative trailing-edge geometries of UCAV configurations is indicated in Figure 2.1.2

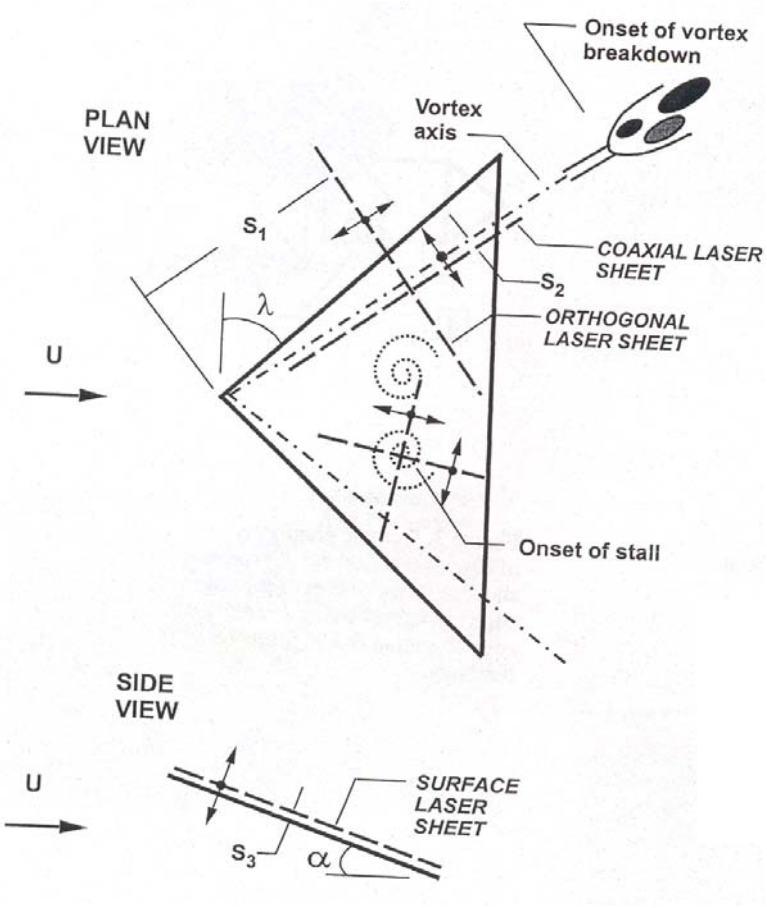


Figure 2.1.1. Schematic of simple delta wing showing onset of vortex breakdown and stall.

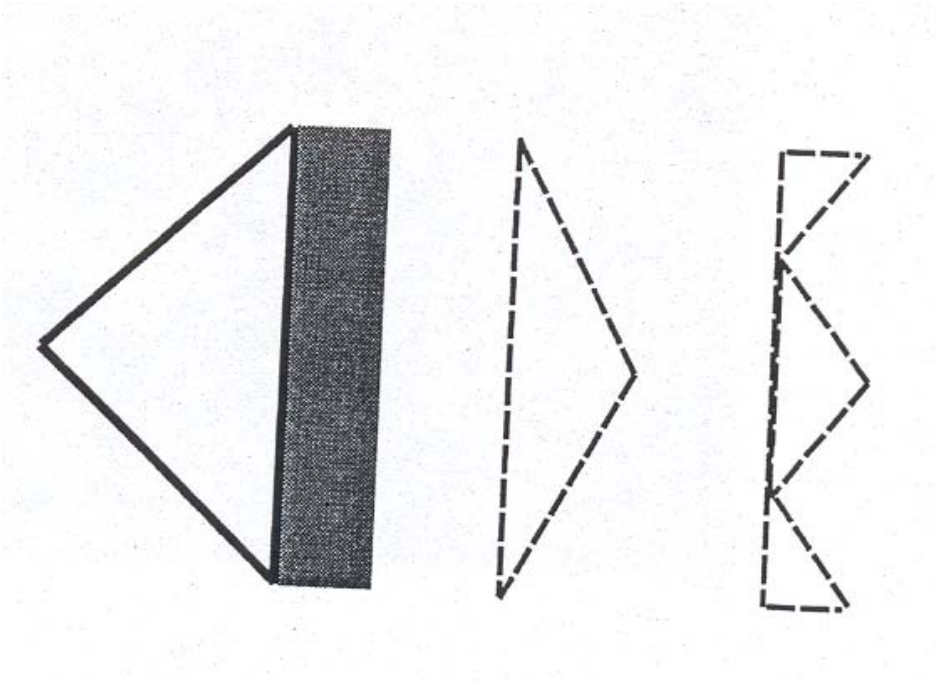


Figure 2.1.2. Generic trailing edge configurations of UCAV planforms alteration due to fuselage/forebody.

In the following subsections, brief synopses of previous related investigations are provided, with emphasis on the basic physical features associated with the onset of regions of vortex breakdown and stall.

a) Vortex breakdown

During the past four decades, substantial advances, both in theoretical and numerical investigations, have furthered our understanding of the criteria and mechanisms for the onset of vortex breakdown in basic types of flow configurations, which include flow past a highly swept delta wing, swirling flow in a tube, and in a cylindrical vessel. Overviews of these advances, as well as descriptions of both theoretical and numerical investigations, are provided by Sarpkaya (1971a,b; 1974), Leibovich (1978, 1984), Escudier (1988), Brown and Lopez (1990), Lopez and Perry (1992), Delery (1994) and Wang and Rusak (1997). These diverse and valuable contributions provide a framework for the present investigation. Of particular interest for our present purposes is information on the spectral content of

regions of vortex breakdown and stall. This aspect has received relatively little attention. Certain features of the vortex unsteadiness at locations downstream of breakdown are described by Garg and Leibovich (1979), Lopez and Perry (1992) and Gursul and Yang (1995). Immediately following the onset of vortex breakdown, a pronounced spectral peak is usually evident, then in regions further downstream, a number of peaks are identifiable as part of a degeneration to a broader-band spectral content.

b) Sensitivity of vortex breakdown to conditions in downstream regions of the flow

The process of vortex breakdown, which usually serves as a prelude to regions of stall on swept wings, is not simply determined by the approach flow and local flow conditions. Rather, it is by now recognized as a global phenomenon, which can be strongly influenced by downstream boundary conditions or geometrical irregularities. For example, when vortex breakdown occurs in the vicinity of the trailing-edge of a delta wing, small changes in angle-of-attack can yield substantial changes in the location of vortex breakdown. Akilli et al. (2001) have investigated the sensitivity of vortex breakdown. They have studied that a small wire oriented orthogonally to the axis of the leading-edge vortex on a delta wing at high angle-of-attack generates substantial changes in the vortex structure, which is characterized using a technique of high-image-density particle image velocimetry. They have used a wire having a diameter two orders of magnitude smaller than the diameter of the leading-edge vortex prior to the onset of vortex breakdown. They concluded that a wire can substantially advance the onset of breakdown by as much as fifteen vortex diameters. They have found that depending upon the dimensionless diameter of the wire and wire location along the axis of the vortex, the onset of vortex breakdown can occur either upstream or downstream of the wire. They also showed that contours of constant velocity indicating the rate of decrease of streamwise velocity along the centerline of the vortex is substantially enhanced, even for locations well upstream of the wire, relative to the case of vortex breakdown in absence of a wire. They also conclude that patterns of instantaneous vorticity in presence of the wire

typically exhibit a form characteristic of either a spiral- or bubble-like mode of breakdown that occurs in absence of the wire.

Furthermore, blowing from the trailing-edge of the wing can have a dramatic upstream influence on alteration of the onset of vortex breakdown, Shin and Ding (1996). The effects of trailing-edge jet entrainment on the streamwise vortices over a delta wing were examined by Helin and Watry (1994). They visualized the location of vortex breakdown with respect to trailing-edge jet velocity using a 60 deg delta wing model in a water tunnel with dye to mark the vortex core. However, the influence of the trailing-edge jets on vortex bursting and asymmetry was examined for a delta wing at various angles of attack. All of these observations suggest that spanwise variations of the trailing-edge geometry, as well as use of thrust vectoring, will have very substantial effects on the occurrence of vortex breakdown and the eventual onset of regions of stall.

From a theoretical standpoint, approaches over the years have suggested the role of upstream influence when describing the onset of vortex breakdown. The survey of Leibovich (1984) were interested in the stability and breakdown of isolated incompressible vortices at high Reynolds numbers; instabilities arising from interactions between two or more vortices were not considered. A vortex can be unstable without breakdown, and it appears that axial flow reversals can be created in swirling flows without any sign of hydrodynamic instability to infinitesimal disturbances. A breakdown event causes significant modifications of the vortex structure, so and experiments at high Reynolds number reveal that the flow downstream of it is always more unstable than that of upstream. Breakdown acts as a switch that marks the onset of transition to a turbulent flow downstream if the upstream flow is laminar, or transition to a flow with a higher level of turbulent fluctuations in the downstream if the vortex upstream of breakdown is already turbulent. Leibovich (1984) noted that the size of vortical core formed by roll up of a vortex sheet was independent of Reynolds number (although the radius of the viscous subcore decreases with increasing Reynolds number). The center of a leading-edge vortex was generally located on the order of a core diameter above the lifting surface, and the core diameter might not be negligibly small compared to the

local semi span of the lifting surface. He reviewed a variety of theoretical concepts that describe the onset of vortex breakdown, including criticality criteria. He also referred to the highly relevant works of Squire (1962) and Benjamin (1962) and underscored the importance of considering the streamwise evolution of the vortex core, rather than simply assuming that the core is of the columnar type.

The consequence of an evolving vortex core is to allow disturbances to spread upstream of a source located in the downstream region of the flow. That is, it is possible for a downstream disturbance to generate upstream traveling waves, the longest of which will move the most rapidly and can reach the critical location in the region of vortex breakdown. More recently, the theoretical assessment of Wang and Rusak (1997), along with their previous investigations cited therein, as well as the study of Rusak, Wang and Whiting (1998), provide a framework for describing an upstream influence. In essence, provided the swirl ratio of the vortex falls within a defined range, it is possible for disturbances to propagate upstream and, in the steady state, they are associated with a stable state of vortex breakdown.

c) Vortex breakdown along wing surfaces

A range of experimental investigations has addressed the interrelationship between the induced pressure fluctuations on aerodynamic surfaces and the unsteadiness of vortex breakdown above the surface. Pressure fluctuations at defined locations beneath vortex breakdown on a delta wing are provided by Mabey (1973), Roos and Kegelman (1990), and Gursul (1994). It is possible to classify the pressure fluctuations on the surface of the delta wing in terms of dimensionless frequencies which, in turn, represent various features of the flow unsteadiness, including the onset of vortex breakdown. This aspect is addressed in the series of investigations of Gursul and Yang (1994, 1995). Gursul and Yang (1995) were studied the relationship between the helical mode instability and the unsteadiness of vortex breakdown location. Flow visualization techniques and velocity measurements using Laser Droppler velocimetry (LDV) were carried out over a delta wing. The results of this investigation showed that the fluctuations of vortex breakdown location occurred

at much lower frequencies than the frequency of the hydrodynamic instability of the flow in the wake of the vortex breakdown in their investigation. And, they recommended that the helical mode instability does not affect the unsteady nature of breakdown location.

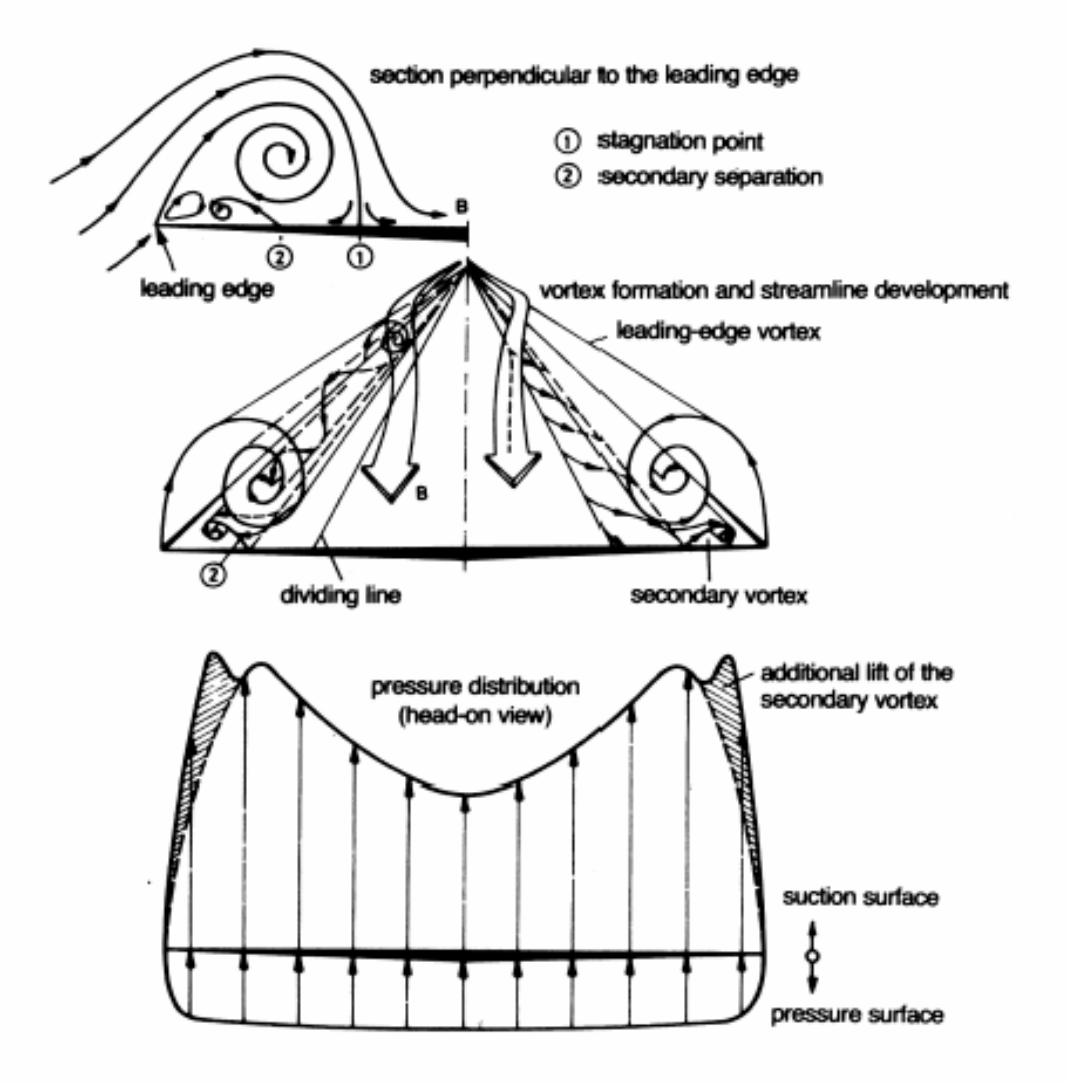


Figure 2.1.3. Delta Wing Flowfield

The shear layers proceed to roll into a pair of counter-rotating vortices which contain a viscous core with large axial velocities surrounded by spiraling flow, as shown in Figure 2.1.3 (Hunecke, 1987).

The spectrum of unsteady flow phenomena over delta wings as a function of dimensionless frequency is a necessary part of the onset of the instability. For the related point of view, the investigations of the unsteady behavior of vortex breakdown location obtained from flow visualization were provided by Menke et al. (1996). The source of small scale fluctuations was also investigated. It was obtained that the peak observed in the spectrum of fluctuations of vortex breakdown location is due to the antisymmetric motion of breakdown locations for left and right vortices, which suggests an interaction between these vortices. The frequency of this organized motion is much smaller than the frequency of any other known instabilities. The most probable frequency for the high-frequency small amplitude fluctuations of breakdown location is in the same range as the frequency of Kelvin-Helmholtz instability.

In essence, several possible classes of unsteadiness can give rise to surface loading of the wing. They include: random displacements of the vortex core (Menke and Gursul, 1997); helical mode instability of the vortex breakdown flowfield (Garg and Leibovich, 1979; Gursul, 1994) and fluctuations of the vortex breakdown location in the streamwise direction (Gursul and Yang, 1995).

d) Interaction of vortex breakdown with aerodynamic surfaces

Unsteady loading, i.e, buffeting, of surfaces of a wing, as described in the previous section, involves flow physics that have certain features in common with vortex breakdown incident upon aerodynamic surfaces such as tails and fins of aircraft. It is appropriate to review briefly the investigation of vortex breakdown impinging on various types of bodies, including tails and wings of aircraft. A general overview was given by Rockwell (1998).

For the class of interactions involving a streamwise-oriented region of vortex breakdown incident upon a tail or fin, the major emphasis, in practical investigations, has been on measurement of time-averaged and unsteady forces, moments and surface pressures, as well as surface acceleration, as described in the investigations of Triplett (1983), Brown, Lee and Tang (1990), Lee, Brown, Ziglea and Poirel

(1990) and Lee and Brown (1992). Flow visualization of the structure of the vortex, as it impinges upon a fin or tail, is provided by Erickson, Hall, Banks, Del Frate, Schreiner, Henley and Pulley (1989), and Fisher, Del Frate and Richwine (1989). Measurements of the fields of velocity fluctuations, on the basis of pointwise techniques, have focused on the region in the vicinity of vertical tails. These studies include those of Sellers, Meyers and Hepner (1988), who performed measurements on a model of a YF-17 aircraft, and showed that large amplitude velocity fluctuations can occur in the vicinity of the tails. Komerath, Liou, Schwartz and Kim (1992a, 1992b) performed measurements in the vicinity of the tails of a model of an F-15 aircraft; they found peaks in the velocity spectra at locations on the inboard and outboard sides of the vertical tails at sufficiently high angle-of-attack.

Breitsamter and Laschka (1994) undertook extensive data acquisition of the pointwise velocity fluctuations in the vicinity of a fin in a delta-canard configuration. Even though the Reynolds number had a relatively high value, i.e. Re = 10^6, they observed sharply defined peaks in the spectra of the velocity field. These findings reinforce the view that the occurrence of vortex breakdown and the associated fluctuating velocity field are predominantly inviscid. In turn, hot wire measurements are in general accord with remarkable visualization of the instability of vortex breakdown on a full-scale research version of the F-18 aircraft at high angle-of-attack, as reported by Fisher, Del Frate and Richwine (1989).

Global, quantitative characterization of the flow can lead to new understanding of vortex-plate and vortex-tail interactions. Moreover, these techniques are also directly applicable considering with the onset and development of vortex breakdown and stall along wings of various planforms. Global instantaneous and averaged representations of the flow pattern were given by Mayori and Rockwell (1994), Canbazoglu et al. (1995), Sahin et al. (2001) and Ozgoren et al. (2002b). This series of investigations represents the first quantitative imaging of vortex breakdown-surface interactions and provides a foundation for the next studies.

Fluctuating flow-field adjacent to the surface of the fin that becomes a reason rising to the unsteady loading is relatively less known. The characterization of the incident vortex-fin interaction for the simplified configuration of a delta wing was

investigated by Canbazoglu et al. (1995). It was given that global instantaneous and averaged representations of velocity field, streamline patterns, vorticity contours related with root-mean-square representations of vorticity fluctuations and instantaneous vorticity correlations provide a rational basis for the corresponding spectra of surface pressure at crucial locations on the surface on the fin typical of that found on F-series aircraft.

The fact that the fluctuating loading causes flow-induced vibration on aerodynamic surfaces. Maneuverability and control of high performance aircraft is constrained due to this vibration. The investigation of Wolfe et al. (1995) showed the relation the time-averaged and instantaneous structure of vortex breakdown incident upon a thin plate to spectra of surface pressure along the plate. They indicated that the dominant freaquency of the surface pressure on the plate is insensitive to offset of the vortex axis relative to the leading-edge of the plate. On the other hand, global fluctuation at the entire region of vortex breakdown is sensitive to the offset of incident vortex. Alternately, an effective imaging approach involves use of planar Doppler velocimetry which, in the investigation of Beutner, Baust and Meyers (1995), has yielded time-averaged representations of vortex-fin interaction, including root-mean-square distributions of fluctuation parameters.

All of the foregoing experimental investigations are complemented by numerical studies, including those of Rizk and Gee (1992), Gee, Merman and Schiff (1995), Kandil, Sheta and Massey (1995), and Rizzetta (1996), These studies have simulated selected features of the vortex breakdown-tail interaction and, in most cases, have related them to the corresponding loading characteristics and tail. The importance of upstream influence of aeroelastic deflections of the tail on the onset of vortex breakdown is pointed out in the numerical study of Kandil, Sheta and Massey (1995).

Recently, numerical computations by Gordnier and Visbal (1997) give detailed, instantaneous and time-averaged three-dimensional flow patterns due to the impingement of a vortex pair, originally from a delta wing, upon a flat plate. Using this approach, Gordnier and Visbal (1997) showed the existence of three-dimensional patterns of separation on both sides of the plate, which results from spanwise

variation of the effect of angle-of-attack which, in turn, is induced by the incoming vortex system.

2.2. Models of Buffet-Loading of Aerodynamic Surfaces

A first step in modeling, or scaling, the unsteady loading of a wing or aerodynamic surface, due to vortex breakdown or stall, is to determine the predominant frequencies of these phenomena. Then, it is desirable to formulate a framework for guiding interpretation of the surface loading in terms of the flow physics. Such a framework does not exist for severely separated flows such as breakdown or stall. With the aim of working towards such a framework, it is desirable to review existing models for buffet loading of aerodynamic surfaces.

a) Scaling of vortex breakdown-wing interactions: predominant frequencies

When vortex breakdown occurs above the wing, it typically gives rise to a predominant spectral peak of the surface pressure fluctuation, which is well above the broadband background. The predominant frequency corresponds to the helical mode of instability of the flow downstream of the occurrence of vortex breakdown, as investigated by Garg and Leibovich (1979) and Gursul (1994). The spectral distributions of surface pressure fluctuations on a wing have the same general form as those due to vortex breakdown impinging upon a tail of a simulated aircraft, as measured by Wolfe et al. (1995). In fact, Wolfe et al. (1995) showed that a simple scaling parameter could be employed for the frequency of the predominant spectral peak. This scaling is valid over a wide range of Reynolds and Mach numbers, In fact, the case of a near miss encounter of a streamwise, broken down vortex along a plate is directly analogous to the naturally occurring vortex breakdown of the leading-edge on a delta wing at high angle-of-attack. Generally speaking, the unsteadiness on a delta wing must also include contributions due to random displacements of the vortex core and fluctuations of the position of vortex breakdown, as shown respectively by Menke and Gursul (1997) and Gursul and Yang (1995).

b) Prediction of buffet-induced loading

A review of models of the buffet loading and response of aircraft wings and tails/fins is given by Lee (2000). The transient response of the wing to non-stationary buffet loads is given by Lee (1980), whereby a variety of maneuvers of the aircraft are accounted for. Furthermore, Lee (1979) revealed that if the loading on the wing arises from fluctuating forces from a variety of uncorrelated sources, it is possible to represent the buffet load spectra using a series representation. In turn, the total response is due to the sum of the individual responses to each term in the series (Lee, 2000). For the related problem of buffeting of fins and appendages, prediction techniques have been developed by Lan and Lee (1986) Lee and Dunlavy (1992).

For modern high performance fighters, the ability to fly to high angles of attack is of prime importance. The combination of leading-edge extention (LEX) and vertical tail placement leads to the aircarft's excellent high angle of attack performance. The LEX maintains lift at high angles of attack by generating a vortex that trails aft over the top of the aircraft. And, the vortex entrains air over the vertical tails to maintain the stability of the aircraft. The entrained flow produces severe buffet and has led to premature fatique failures of the empennage. For empennage buffet, one of the investigation was examined by Zimmerman et. al. (1989). Their investigation was to develop methods that could be used to decribe the empennage buffet environment and to predict empennage buffet loads for use in aircraft design.

All of the foregoing models do not consider the nature of the flow adjacent to the wing surface or the tail/fin surface. In fact, most required measured surface pressure as an input. Recently, Breitsamter and Laschka (1998) have devised a buffet model, which is based on time-averaged pointwise velocity measurements of the flow in the absence of the adjacent aerodynamic surface. The major assumptions in this study are that the presence of the surface does not alter the unsteady flow pattern that gives rise to the buffet loading, and that flow separation does not occur. Yet, the evolution of vortex breakdown/stall along the surface of the wing, or its impingement upon a plate or tail/fin typically involves significant, and in some cases very substantial, distortion of the flow. It is therefore most appropriate to determine the

sequence of the patterns of instantaneous vortex distortion, which eventually can be employed to determine the physical origin of the buffet loading. Furthermore, at high angle-of-attack, severe flow separation can occur, and must be accounted for.

2.3. Global, Instantaneous Flow Patterns: Relation to Motion and Loading of Aerodynamic Surfaces

In order to understand the origin of buffet loading of aerodynamic surfaces, it is necessary to establish a relationship between the unsteady flow structure adjacent to the surface and the loading of the surface. The traditional experimental approach has been centered on use of force/pressure/acceleration transducers, sometimes in conjunction with qualitative flow visualization, i.e. smoke or dye. This general approach typically leads to a comparison of instantaneous qualitative flow patterns with time-averaged representations of the unsteady loading. Further approaches, which involve characterization of one or more fluctuating velocity components adjacent to the surface, typically involve point wise measurement techniques and, in most cases, yield time-averaged representations of the fluctuating flow fields.

Recent advances in the area of whole field imaging techniques, in particular the method of high-image-density particle image velocimetry of direct interest herein, has allowed determination of global, instantaneous patterns of the flow, which can lead to new types of insight into the unsteady loading of a wing, plate, or tail/fin. Magness et al. (1992, 1993a, 1993b) provided the first instantaneous patterns of vorticity and streamline topology of the leading-edge vortices on a delta wing subjected to unsteady pitching motion. Using this approach, it was possible to determine the existence of critical topological features such as unstable foci of leading-edge vortices and the relationship of this topology to the pronounced phase lag of the vortex evolution with respect to the motion of the wing.

Towfighi and Rockwell (1993) used a similar approach to yield the first instantaneous, wholefield images of vortex breakdown. Using this approach, it was possible to demonstrate that a crucial feature of the vortex breakdown region is switching of the sign of the instantaneous concentrations of azimuthal vorticity. This

finding was in accord with the theoretical model of Brown and Lopez (1990). A subsequent investigation of Lin and Rockwell (1995) interpreted the highly unsteady response of vortex breakdown on a delta wing subjected to transient motion; critical points of the breakdown region were related to patterns of azimuthal vorticity. The fact that self-excited, streamwise excursions of the vortex breakdown region are of central importance in determining the instantaneous flow topology was demonstrated by Cipolla and Rockwell (1998a). In the event that the leading-edge vortices at high angle-of-attack develop in presence of localized blowing at the trailing-edge, the streamline topology, as well as patterns of vorticity can be substantially altered, as shown by Shih and Ding (1996). A detailed characterization of the structure of the vortex breakdown in the leading-edge vortex is provided by Ozgoren et al. (2002a). It showed that the instantaneous patterns of vorticity in the central region of the vortex coexist with pronounced concentrations about the periphery of the vortex, apparently due to a centrifugal instability of the vortex sheet that rolls into the evolving leading-edge vortex.

Further investigations that also employ quantitative PIV imaging techniques have concentrate on the interactions of broken-down vortices with plates and tails/fins, as described by Mayori and Rockwell (1994), Canbazoglu et al. (1995). The latter two investigations characterized the relation between patterns of vorticity and the corresponding streamline topology due to distortion of vortex breakdown along the surface of the plate/tail and, moreover, related these quantitative features of the flow structure to the surface pressure fluctuations. Most recently, Akilli et al. (2001) related the instantaneous patterns of vorticity to spectra of the unsteady flow field, determined by a very large number of points using simultaneous records from a time sequence of global, instantaneous images. This cinema version of high-image-density PIV was originally developed by Lin and Rockwell (1994), who obtained highly-resolved, space-time images of patterns of streamwise vorticity. Such a space-time imaging approach has also provided a relation between the quantitative instantaneous flow structure and surface pressure fluctuations at leading-edges and corners, as described in the works of Lin and Rockwell (1999, 2001).

The fact that these types of quantitative imaging approaches can provide a meaningful basis for control of vortex development and vortex-surface interaction is described in a series of works. Impingement of coherent vortical structures upon airfoils, blades occurs in a different configuration, involving helicopters, wings and tails of aircrafts and blades of turbomachinery and wind turbines. The reason of pressure fluctuation, which causes unsteady loading and noise generation, is a vortex interaction with a surface. These unsteady loading and noise generation causes early failure of an airfoil or blade. Jefferies and Rockwell (1996) pointed out the detail structure of the interaction of an incident vortex with a leading edge that is oscillating at the frequency of the incident vortex street. Characterization of the mechanisms of interaction as a function of the timing, or phase shift of the incident vortex relative to the motion of the edge was indicated using instantaneous streamline patterns and vorticity distributions in this investigation.

Ozgoren et al. (2001) have studied on a delta wing which is subjected to small-amplitude perturbations over a range of periods, in order to simulate leading-edge control concepts. They pointed out that substantial modifications of the instantaneous and averaged structure of the leading-edge vortex are attainable, both with and without a downstream impingement plate. They also concluded that the location of the onset of vortex breakdown can either be advanced or retarded, and the attendant changes in vortex structure are interpreted in the context of buffeting of the impingement plate. They have found that comparison of the vortex structure with and without deployment of the plate shows a dramatic influence of the plate.

Furthermore, passive control, in the form of a transverse wire across the vortex, whereby the wire has a diameter that is two orders of magnitude smaller than the characteristic vortex diameter, can lead to remarkable alterations of the onset of vortex breakdown, as shown by Akilli et al. (2001).

2.4. Control / Attenuation of Buffeting of Aerodynamic Surfaces

Efforts to control the structure and trajectory of leading-edge vortices formed from leading-edge extensions, as well as actual leading-edges of wings, have

involved passive techniques, in the form of geometrical modifications at or upstream of the leading-edge and placement of a small wire within the leading-edge vortex; and active (open loop) approaches, which include blowing at the leading-edges of the wing and perturbations of the wing at very small amplitudes and high frequencies, in order to simulate leading-edge actuators. These approaches are briefly described in the following.

a) Geometrical modifications

Modifications of the leading-edge shape of a swept wing, as well as fences mounted on the leading-edge extension (LEX) of an aircraft, have aimed to attenuate the buffet-induced loading of a tail/fin. These concepts can, however, be considered for control of buffeting of a wing-surface, since they can potentially alter both the trajectory of streamwise vortex, as well as the location of vortex breakdown. Brown, Lee and Tang (1990) evaluated the effectiveness of a LEX on a CF-18 aircraft, and demonstrated a reduction in both the mean and unsteady loading of the fin. The penalty in performance characteristics was small, in that the aircraft lift and pitching moment showed only small changes. Shah (1991) explored modifications of the LEX on an F-A-18 model. He discovered that both the buffet-induced loading and the aerodynamics at high angle-of-attack were strong functions of the geometry of the LEX. Furthermore, the vortex flow showed changes in trajectory, strength, and the position of vortex breakdown. Martin and Thompson (Agard CP-497) also considered a model of an F-A-18 aircraft and observed that substantial attenuation of the unsteady pressure loading of the fin (tail) could be achieved by proper deployment of LEX. Taken together, all of the foregoing investigations indicate that small-scale geometrical modifications, which are properly deployed relative to the origin of a vortex, can have a substantial influence on the trajectory, strength and location of vortex breakdown.

b) Small wires

Akilli et al. (2001) have used a small wire oriented orthogonally to the axis of the leading-edge vortex on a delta wing at high angle-of-attack generates substantial changes in the vortex structure as explained in section 2.1.b. The effectiveness of this control technique is a strong function of the streamwise location along the axis of the vortex, thereby suggesting that the local swirl ratio of the vortex is a critical parameter for this type of control.

This type of control approach, which involves proper deployment of a very small, passive body within the vortex, shows considerable promise for extension to other types of bodies, with eventual application to a range of wing configurations.

c) Blowing at the leading-edge

Localized blowing at the leading-edge of a wing can produce substantial variations of the onset of vortex breakdown, as described by Gu et al. (1993). They have examined the control of flow past a half-delta wing at high angle-of-attack experimentally. They observed that the onset of vortex breakdown and stall were delayed substantially by applying of steady blowing, steady suction, or alternative suction-blowing in the tangential direction along the leading edge of the delta wing.

Blowing at the leading-edge has also been employed as a method for deflecting the leading-edge vortices, such that the magnitude of the tail buffet loading is reduced, as demonstrated by Bean and Wood (1996). In fact, they were able to attain both a reduction in strength of the leading-edge vortex and shift of its position in the inboard direction. For practical aircraft configurations of the F-15 type, Huttsell, Tinapple and Weyer (1997) have employed a scale model to examine the effect of localized tangential blowing, which was deployed at a number of different locations. It was found that blowing at the wing root was most effective in altering the bending and torsional response of the tail.

d) Blowing at trailing-edge

The onset of vortex breakdown is known to be a globally sensitive phenomenon, and is particularly receptive to conditions in the downstream region of the flow. For example, localized blowing from the trailing-edge of the wing has dramatically altered the vortex breakdown location in the investigations of Helin and Watry (1994), Shih and Ding (1996). Of course, thrust vectoring is a common feature of the UCAV configurations, which do not have a tail/fin, and the existence of this type of trailing-edge blowing is expected to produce a substantially altered onset of vortex breakdown and stall.

Werle (1960), at Onera, was the first to conduct experiments applying various flow control techniques to manipulate the vortical flow around a delta wing and to alter the vortex breakdown location. He showed the ability of four parameters or flow control techniques to influence the vortices and their breakdown locations by observations of colored dyes injected around delta wings in water tunnels. These four techniques for influencing vortices and the respective breakdown locations are shown in Figure 2.4.1.(a~d) and can be described as: an obstacle in the flow downstream of the delta wing's trailing edge, suction over the suction surface of the delta wing, along-the-core blowing over the suction surface and blowing against the axial velocity in the vortex core.

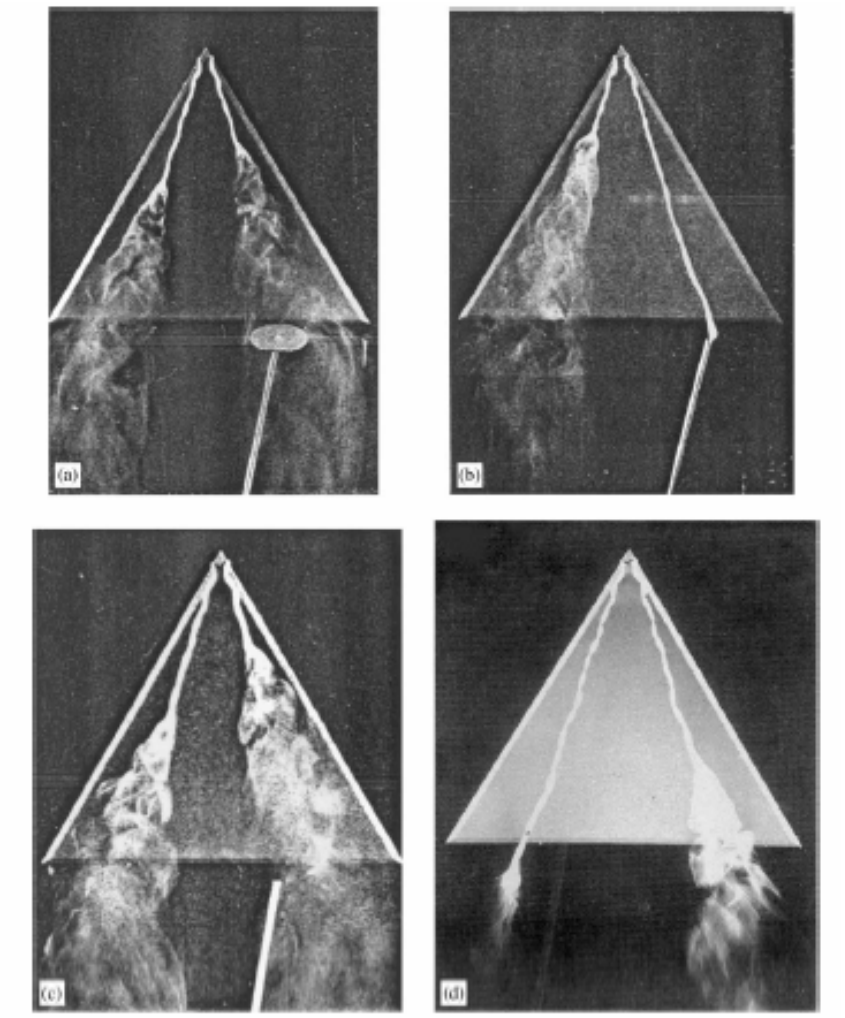


Figure 2.4.1. The effect of different flow control techniques (a) Obstacle downstream b) Suction c) Blowing opposite the axial velocity of the vortex core d) along the core blowing Werle (1960).

e) Simulated perturbations at the leading-edge.

The possibility of controlling the unsteady structure on a delta wing by application of small amplitude perturbations has been addressed by Gad-el-Hak and Blackwelder (1986), who demonstrated the consequence of small-amplitude pulsations of flow through the edge of a delta wing on the instability. Ozgoren, Sahin and Rockwell (2001) characterized the effect of perturbations of the entire wing on the time-averaged features of the multiple shear layer structure of the leading-edge

vortex, including the onset of vortex breakdown. They subjected a delta wing to very small amplitude oscillations in the pitching mode, but at a sufficiently high frequency such that the structure of the leading-vortex was substantially altered. These modified leading-edge vortices impinged upon a downstream plate, and the instantaneous and averaged features of the vortex-plate distortion showed that the buffet velocity field was considerably modified, relative to the case of a stationary wing without perturbations at, or of the leading-edge.

Rediniotis et. al. (1994) presented that the transient flow field over a delta wing during picth-up motions to very large angles of attack. Instantaneous pressure distributions on the suction surface of the model were obtained only by point measurements in order to get the effect of the growth and the eventual breakdown of leading edge vortices. The results showed significant differences of vorticiy content between the steady and the unsteady motions. They mentioned that the tip vortices retain a core with concentrated large values of vorticity and a strong axial velocity component for angles of attack as large as 48^0. Also, breakdown follows and eventually a bluff body wake patterns set in.

To date, the unsteady flow structure during transient pitching maneuvers has remained unidentified. One of the investigations about this was Magness et al. (1993b) who provided a new topological structure over a delta wing undergoing transient pitching maneuvers at high angle-of-attack. They observed the instantaneous streamline topology and vorticity patterns of leading-edge vortices over a delta wing subjected to unsteady pitching motion. It was shown that instantaneous structure differs substantially from the traditional topology observed for stationary wings at low angle-of-attack. The existence of critical topological features such as unstable foci at leading-edge vortices and phase lag of vortex evolution over a delta wing in maneuver.

Yaniktepe and Rockwell (2004) has demonstrated that the consequence of small amplitude perturbations of the leading-edge, at an appropriate frequency, on the time-averaged pattern of the separated shear layer adjacent to the wing surface. They pointed out that when the wing is subjected to small-amplitude perturbations, substantial alterations of both the instantaneous and time-averaged structure were

observed. They also concluded that the most effective frequency of excitation corresponds to the sub harmonic of the broadband fluctuations in the region of the shear layer closest to the leading-edge, though this criterion was not necessarily universal for other geometric and flow parameters.

All of the aforementioned investigations provide a basis for gaining an understanding of the flow structure on UCAV configurations and techniques for its control. Optimization of either active or passive control techniques, or perhaps a combination of them, based on a proper understanding of the flow physics past UCAV configurations, have been considered.

f) Stationary wing: surface patterns

As described by Lighthill (1963), and further addressed by Hunt, Abell, Peterka and Woo (1978), surface streamlines, i.e. patterns of streamlines immediately above the surface, are representative of skin friction lines at the surface, provided the viscosity of the external flow is small and/or the oil film is thin enough to be unaffected by the pressure gradient. The shear-stress lines indicated by oil streamlines at the surface will be aligned with the streamlines of the external flow very near to the surface. Lighthill (1963) suggests that because of this relationship, shear-stress lines may be called surface streamlines, or "limiting streamlines". Hunt et al (1978) further discusses the possibility of using patterns of surface streamlines (shear stress lines) to infer the off-surface characteristics of the external flow field. In fact, the literature demonstrates that this can be done quite successfully (Chapman and Yates, (1991); Peake and Tobak, 1982; Hornung and Perry 1984; Chong and Perry, 1986; Perry and Chong, 1987; Dallmann, Hilgenstsock and Reidelbauch, 1990).

All of these considerations correspond to the time-mean or time-averaged surface streamline pattern. Yet, these averaged surface streamlines will be a consequence of the sequence of global, instantaneous surface streamlines, which can be directly determined using high-image-density particle image velocimetry. The laser sheet indicated in the side view of Figure 2.1.1 was located sufficiently close to

the surface, in accord with the criteria of Lighthill (1963) and Hunt, Abell, Peterka and Woo (1978).

2.5. Buffet-Induced Loading on The Basis of Unsteady Flow Patterns

Pressure loading on the surface of the wing is a function of the flow fluctuations adjacent to its surface. The aforementioned characterizations of the flow unsteadiness, when properly interpreted using assessments of global images, can provide a basis for eventual formulation of models of buffeting of aircraft surfaces beneath regions of vortex breakdown and stall.

Breitsamter and Laschka (1998), and the literature cited therein, emphasize that models of the structural response of the aerodynamic surfaces rely on experimentally-determined surface pressures. Representative models of this type include those of Lee (1984) and Zimmerman et al. (1987). The fact that buffet spectra can be extrapolated to large ranges of model sizes and velocities is described by Zimmerman et al. (1987, 1989). Breitsamter and Laschka (1998) derived a model that relates the surface pressure loading to the turbulence intensities, power spectra, and cross-power spectra of the fluctuating flow adjacent to an aerodynamic surface. In their attempt to relate the surface pressure loading to the turbulence field above the surface, it was necessary for Breitsamter and Laschka (1998) to make crucial assumptions. The first is that the flow was not separated. Second, it was assumed that the turbulence was not distorted by existence of the aerodynamic surface. Both of these classes of assumptions were not appropriate for the highly separated, inherently three-dimensional flow fields associated with the onset and development of regions of vortex breakdown and stall above the surface of the wing.

2.6. Small-Scale Patterns of Flow Structure Including Highly Swept Wings

In recent years, considerable insight has been gained into the averaged and unsteady structure on delta wings having relatively large sweep angle. These investigations, which are described in the following, serve as a basis for interpretation of the flow structure on wings of moderate sweep angle, which is the focus of the present investigation.

The occurrence of small-scale vortical (sub-vortical) structures is well known. Their quantitative, time-averaged features have been assessed in detail by Riley and Lowson (1998), who undertook an extensive study, using Laser Doppler Anemometry (LDA), of the flow structure on a wing of sweep angle $\Lambda = 85°$. On the basis of averaged vorticity measurements, they revealed a system of steady, co-rotating, small-scale vortices. These sub-structures were observed in earlier investigations by Payne et al. (1988), Lowson (1988), and Reynolds and Abtahi (1989) using visualization techniques, and more recently by Washburn and Visser (1994) and Mitchell, Molton, Barberis and Delery (2000) via time-averaged measurements of the flow structure. Visbal and Gordnier (2003) and Gordnier and Visbal (2003) performed the first numerical simulations of the instantaneous structure on wings of relatively large and small sweep angle respectively. They demonstrated that steady substructures are apparent in the time-averaged (mean) patterns of the transitional turbulent shear layer from the leading-edge.

An experimental investigation of vortex breakdown on delta wings at high angle of attack was presented by Payne et. al. (1988). They considered a series of flat-plate delta wings having sweep angles of 70, 75, 80 and 85 deg for obtaining cross-sectional views of the leading-edge vortices using smoke visualization and the laser light sheet technique and measurements were performed using a LDA. They presented flow visualization that clearly confirms the existence of secondary structures developing in the leading-edge shear layer. However, the structure they observed appear stationary. Thus, velocity measurements on a 70 deg delta wing at 30 deg angle of attack showed that, when breakdown occurs, the core flow was transformed from a jet-like to wake-like flow.

In parallel with the investigation of the aforementioned steady sub-structures, Riley and Lowson (1998) addressed time-dependent instabilities from the leading-edge of a delta wing. These unstable structures were first observed by Gad-el-Hak and Blackwelder (1985). They examined the leading edge vortex on a delta wing in steady flight consists of a series of discrete smaller vortices, a perturbation of these discrete vortices. The flow was perturbed by impulsively injecting or withdrawing secondary fluid from a slot along the entire leading-edge of a delta wing. By perturbing the leading edge of the delta wing, the shedding and pairing of the discrete vortices were modulated. Leading edge perturbations dramatically affected the evolution of the bounded shear layer originating from the delta wing's leading edge.

The possibility of controlling the unsteady structure on a delta wing by application of small amplitude perturbations has been addressed by Gad-el-Hak and Blackwelder (1985), who demonstrated the consequence of small amplitude pulsations of flow through the edge of a delta wing on the instability. They found that maximum changes in the leading edge vortices occur when the perturbation frequency is a sub-harmonic of the natural shedding frequency of the unperturbed wing. Recently, Ozgoren, Sahin and Rockwell (2002a) provided an additional perspective on this instability. Lowson (1988), using smoke visualization, characterized both this unsteady type of instability, as well as the aforementioned steady, sub-vortical instability, and noted that their coexistence could result in interaction, and thereby interference between the two basic forms of instabilities. Lowson (1988) indicates that the unsteady structures can coalesce, or merge, in a similar spirit as for the classical two-dimensional mixing layer addressed by Winant and Browand (1974). Gordnier and Visbal (1991) performed the first computations of the unsteady sub-structures in the shear layer from the leading-edge, and Gordnier and Visbal (1994, 1995) further characterized features of the unsteady instability from the leading-edge; it was coupled with unsteady boundary layer separation from the leeward surface of the wing. Cipolla and Rockwell (1998b) demonstrated, via quantitative imaging, existence of small-scale structures consistent with the aforementioned simulations. Additional features of instabilities from the leading-edge are addressed by Visbal and Gordnier (2003) and Gordnier and Visbal (2003).

In a more general sense, several types of physical mechanisms can contribute to unsteadiness of the flow structure, at least for sufficiently large values of sweep angle. They include the helical mode instability of vortex breakdown, as characterized for an internal flow by Garg and Leibovich (1979) and flow past a delta wing of large sweep angle by Gursul (1994), as well as other mechanisms summarized and classified by Menke, Yang and Gursul (1999). At lower values of sweep angle-of-attack, Gordnier and Visbal (2003) have shown that pronounced unsteadiness can arise from periodic wandering of the vortex core, which is due to a complex interaction of vortices from the leading-edge and the leeward surface of the wing.

Recent interest in unmanned combat air vehicles (UCAVs) with present study, has stimulated investigation of the flow structure on delta wings having low and moderate values of sweep angle, as well as on planforms that represent the actual UCAV configuration or simplifications thereof.

2.7. Flow Structure on Delta Wings of Moderate and Low Sweep Angle

The distinctive features of the instantaneous and averaged flow structure on a delta wing of sweep angle $\Lambda = 50^{o}$ have been numerically computed by Gordnier and Visbal (2003). At low angle-of-attack, a dual primary vortex system is established, whereas at higher angles-of-attack, this dual structure gives way to a single, larger-scale vortex. Furthermore, the unsteadiness of the vortex core can involve a type of organized wandering at locations upstream of vortex breakdown. The form of vortex breakdown is more complex than for wings of relatively large sweep angle.

Honkan and Adreopoulos (1997) determined patterns of instantaneous vorticity on a delta wing of sweep angle $\Lambda = 45°$ via a pointwise technique, and identified the existence of stationary discrete vortical structures, within the feeding sheet and the primary vortex. Furthermore, they determined turbulence intensity in regions of shear layer attachment and secondary separation. Miau, et al. (1995) investigated the flow patterns on a wing of sweep angle $\Lambda = 50°$, with a focus on the consequences of leading-edge profile.

Ol and Gharib (2001, 2003) undertook an experimental investigation of wings of L = 50° and 65°. They characterized the onset of vortex breakdown using dye visualization and, via a stereo PIV technique, characterized various features of the leading-edge vortex structure, including a large-scale collapse of the rolled-up, leading-edge vortex. Taylor et al. (2003) characterized the vortex flow patterns on a wing of low sweep angle and in a further investigation.

Taylor and Gursul (2004) addressed the relationship between the vortex flow and buffeting of the wing surface. Yaniktepe and Rockwell (2004) considered a wing of sweep angle L = 38.7º and focused on the flow structure well into the region of vortex breakdown including, at high angle-of-attack, the onset of a large-scale region of disordered flow structure beneath a highly organized vorticity layer.

Gursul et al. (2002) summarized recent investigations of low aspect ratio wings and planforms and, furthermore, provide insight into the phenomena of vortex breakdown visualized by dye injection. The consequences of low sweep angle were clearly evident.

Elkhoury et al. (2004) have investigated to provide various measurements of the visualized dye patterns, including the degree of interaction of vortices, the onset of vortex breakdown, and the effective sweep angle of the wing root vortex, as a function of both Reynolds number and angle-of-attack

Elkhoury et al. (2005) has investigated about the Reynolds number dependence of the near-surface flow structure and topology on a representative UCAV planform using a technique of high-image-density particle image velocimetry, in order to complement classical dye visualization. He expressed flow Reynolds number is a critical effect on the double delta wing.

Yavuz et al. (2004) show regions of average vorticity exhibiting well-defined concentrations of like sign along the leading edge which are also distinguishable in instantaneous images of the flow. They state that these features indicate the existence of a co-rotating pattern of small scale vorticity concentrations.

Gursul et al. (2005) reviewed unsteady aerodynamics of nonslender delta wings, covering topics of shear layer instabilities, structure of nonslender vortices,

breakdown, maneuvering wings, and fluid/structure interactions. They compared experimental and computational results cited there in.

2.8. Unresolved Issues

Summaries of recent investigations, as well as unresolved issues, are given in the following.

a) Flow Structure on a Delta Wing of Low Sweep Angle

Averaged Structure of Shear Layer from Leading-Edge of Wing: Of primary interest in recent years has been the structure of leading-edge vortices from slender wings of relatively high sweep angle. For the case of a wing with low sweep angle (less than 40°), the averaged quantitative structure has received very little attention. The issue arises as to what degree a well-defined vortex core, in the form of a single-large-scale concentration of vorticity, can exist, particularly in regions where vortex breakdown and the onset of stall are prevalent, which is the focus of the present investigation. Correspondingly, the streamline topology and the possible existence and location of saddle points in the crossflow plane have not been pursued. At sufficiently high angle-of-attack, the manner in which this topology is altered, in relation to development of gross stall on the wing surface, remains unclarified. Such changes in the topological features are expected to influence the time-averaged forces and moments on the wing and thereby the steady-state performance characteristics.

Unsteady Features of Separated Layer Adjacent to Surface of Wing: It is anticipated that the vorticity layer adjacent to the surface of the wing will exhibit significant unsteadiness, especially when vortex breakdown/stall occur. The relationship between the patterns of fluctuating velocity amplitude and averaged vorticity over the crossflow plane has not been addressed for a wing of low sweep angle. These features are, of course, related to the instantaneous, wholefield patterns of discrete vortical structures, and whether they retain their identity or give way to larger-scale clusters. This instantaneous structure, in turn, will be related to the

spectral content of the velocity fluctuation(s) as a function of distance along the separated layer adjacent to the wing surface. These aspects have not been pursued. Knowledge of the successive, instantaneous states of the flow, and their assessment using spectral analysis techniques, can provide insight into the origin of unsteady buffet loading of the wing. This information could potentially be used in semi-empirical models that relate the flow structure above the wing to the unsteady pressure at its surface.

Control of Flow Structure by Leading-Edge Perturbation: The consequence of small amplitude perturbations of the leading-edge of low sweep angle, at an appropriate frequency, on the time-averaged pattern of the separated shear layer adjacent to the wing surface, has not been addressed. The perturbation that yields the largest change in the flow pattern should be defined, in relation to the inherent formation frequency of vortical structures from the edge. An understanding of this type of control concept could yield practical techniques for controlling the forces and moments on a wing by alteration of the flow structure.

b) Flow Structure on Diamond and Lambda Planforms: Trailing-Edge Region

The emphasis of the present investigation is on the unsteady flow structure, which serves as the origin of buffeting, with emphasis on the configurations of diamond and lambda planforms. A central, generic feature of these planforms is an abrupt change in sweep angle of the leading-edge, from a relatively low value to a value of 90º. The consequence of this sudden change on both the averaged flow structure and the flow unsteadiness has not been clarified. In particular, the following issues have not been addressed.

Crossflow topology on diamond and lambda planforms: The patterns of averaged streamline topology over crossflow planes on lambda and delta planforms are expected to be substantially different from those on a simple delta wing of low sweep angle. The possibility of a well-defined focus (apparent center) of a tightly wound spiral pattern of streamlines, which might be located at the leading-edge, rather than well inboard of it, would be an indication of the rapid flow distortion in

the leading-edge region. In addition, the possibility of a saddle point, i.e., an apparent intersection of streamlines, located outboard of the leading-edge, has not been pursued in relation to the detailed geometry of the diamond and lambda planforms, including the geometry of the trailing-edge.

Moreover, corresponding patterns of time-averaged vorticity, in relation to the streamline topology, have not been defined. It was also investigated, on the basis of investigations of a simple delta wing by Yaniktepe and Rockwell (2004), that an elongated layer of vorticity was formed adjacent to the wing. The possibility, however, of a highly concentrated region of vorticity at the leading-edge, which may be associated with the abrupt transformation of sweep angle, has not been addressed. Furthermore, the averaged patterns of vorticity may exhibit well-defined vortical substructures within the elongated layer from a diamond or lambda planform. For the case of a wing of relatively large sweep angle, where the flow pattern is dominated by a single large-scale vortex, the occurrence of such substructures is well established, as defined in the references given in the Introduction. The possibility that analogous, time-averaged vortical substructures may occur on wings with an abrupt change in sweep angle has not been pursued.

Instantaneous/unsteady flow structure: The time-averaged features described in the foregoing are, of course, a consequence of the instantaneous flow structure. In particular, the instantaneous patterns of vorticity adjacent to the surface of the wing, in relation to possible time-averaged structures, have not been addressed for the wing planforms of interest herein. An important consequence of the instantaneous patterns of vorticity, as well as sequences of them, is the root-mean-square velocity fluctuation along the separated region adjacent to the surface of the wing. These patterns of rms velocity, along with the corresponding spectra, define the physical origin of unsteady (buffet) loading of the wing surface.

2.9. Objectives of Present Investigation

This investigation focuses on flow structure of delta wings with having low sweep angle. The present investigation is to address the issues defined in the

foregoing using a technique of high-image-density particle image velocimetry, which allows whole field representations of both the time-averaged and instantaneous structure. Furthermore, a cinema mode of image acquisition allows, in effect, time records of the flow at a large number of locations, and thereby determination of the corresponding spectra of the fluctuating velocity field.

Beside this, the overall goal of this investigation is to determine the physical features of unsteadiness and to control of the vortex breakdown phenomenon on low sweep wings. These physical features were investigated via quantative space-time imaging in the form of high-image-density particle velocimetry (DPIV). This approach provides a basis for interpretation of unsteady loading, application of control techniques, and guidance for numerical simulations.

The following steps have been considered during the present experimental investigations.

- Three different UCAV planforms have been used, (wings with basic delta, diamond and lambda planforms).
- UCAV planforms was subjected to static variations of angle-of-attack, with the aim of understanding the underlying flow physics and methods for its control.
- It was subjected to perturbations for the case of basic delta wing in order to control the vortex breakdown or stall phenomenon.
- Recently advanced techniques of particle image velocimetry and image analysis have been employed to acquire and interpret sequences of instantaneous, quantitative images of both the surface and the flow patterns. These global assessments lead to an understanding of the origin of buffet loading of basic classes of UCAVs and optimization of control of vortex breakdown.
- Averaged velocity and streamline topology, patterns of averaged vorticity, fluctuating velocity and Reynolds stress correlation, instantaneous patterns of vorticity, spectra along separated vorticity layer of fluctuating velocity have been taken into consideration in order to understand of underlying flow physics and methods for its control.

- Spectral analysis has been employed in order to define the physical origin of unsteady (buffet) loading of the wing surface.

2.10. Outline of Dissertation

Introduction part of this thesis introduces briefly the practical application and importance of the present investigation.

Literature survey part summarizes the research on the physical aspects of vortex breakdown and stall, control of vortex breakdown on a pitching and perturbing delta wing. Unresolved issues which are deducted from the previous investigations and objectives for the present investigation are given.

Material and Method part describes the experimental system (water channel system, delta wing planforms) and measurement techniques.

Results and discussions part of present studies are divided into three parts.

- ✓ The first part reports flow structure (physical aspects of vortex structure, vortex breakdown and stall) on a delta wing of low sweep angle and effect of controlled perturbations on averaged and instantaneous flow structure.
- ✓ The second part of this investigation is to understand flow structure of diamond and lambda planforms, particularly at trailing edge-regions.
- ✓ The third part shows the effect of Reynolds Number on the vortex breakdown location.

Results and discussions part also present overall discussions of present investigation in relation with previous studies.

Finally conclusions and recommendations part summarize the main findings of the present study and provides recommendations for the future investigations as a future work.

3. EXPERIMENTAL SYSTEM AND TECHNIQUES

3.1. Measurement Techniques

Techniques of high image density velocimetry (PIV) will be employed throughout the investigations. Particle Image Velocimetry (PIV) is a Flow Measurement Technique which can be used to obtain the time dependent full field velocity distributions of single and multi-phase flows. Two-dimensional or three dimensional velocity field distributions can be obtained. The particle image velocimetry (PIV) technique provides, for the first time, a global view of the instantaneous flow field in a quantitative fashion. This allows the user to examine the presence of small flow structures and their influence, obtain vorticity fields quantitatively and, finally, obtain mean, turbulence and stresses globally. These unique capabilities provide a powerful diagnostic tool for solving problems, a unique insight into the nature of flows and the ability to improve the performance of fluid machinery and systems.

The PIV uses images of marker particles in a fluid flow to measure instantaneous velocity fields in experimental fluid mechanics. In general, the particles are illuminated by pulsed sheets of light at precise time intervals to produce images that are recorded on photographic film or on a video camera array. In practical application situations, according to the measurement requirements, the appropriate operating mode needs to be selected and specific system configurations are needed. In general, a PIV system consists of illumination, image acquisition, particle seeding, and image processing and data analysis sub-systems. Laser light is commonly used as the illumination source in the PIV systems. Ideal tracer particles should be very small and follow the flow field. Different flow fields need different seeding particles. The design of the seeding particles was discussed by Schmitt et al. (1995). According to spatial resolution requirements, either photographic or CCD video cameras can be used to record the particle images. If the resolution is high enough, CCD video cameras are preferred. To resolve velocity direction ambiguity during the image acquisition process, an image shifting technique is needed (Adrian

1986b). Image interrogation techniques include auto-correlation and cross-correlation image processing methods. The PIV started as a two dimensional velocity measurement method and is being developed to a three dimensional velocity measurement method.

3.1.1. Overview of Correlation Process

Particle Image Velocimetry processing basically determines the distance that the particles moved in the time between laser pulses. The most common methods to determine this distance are particle tracking or correlation. (Özgören 2000) These are Autocorrelation, One-Frame Cross-Correlation and Two-Frame Cross-Correlation. The differences in these correlation techniques are the image window areas for the first and second particle images. In autocorrelation, the same image window is used for both the first and second image window. In one-frame cross-correlation, the second image window is offset from the first image window on the same frame. In two-frame cross corelation, the first image window is on frame one and the second image window is on frame two. Each of these processing techniques has advantages for some applications.

Autocorrelation is for multiple exposure images where the particle motion and image shift together give less than ¼ of the interrogation spot image displacement. This is the classical PIV processing technique.

One-frame cross-correlation is also a multiple exposure technique. It is used when the image shift displacement is large relative to the particle motion displacement. By offsetting the second image window from the first by the mean particle image displacement, distance high-resolution measurements can be made. Otherwise, it would require prohibitively large interrogation spot sizes for autocorrelation processing. By offsetting the second image window by the mean particle image displacement, the interrogation spot size can be reduced and fewer lost pairs relative to autocorrelation will result.

Two-frame cross-correlation measures the distance which particles have moved between exposures on two image frames. Each of these frames has only one

pulse of light. By knowing the sequence of the first pulse images and the second pulse images, the processing signal-to-noise ratio relative to the single frame techniques is improved. Two-frame cross-correlation can measure zero displacements and reversing flows without image shifting. Two-frame cross-correlation can be used with image capture systems with an effective frame rate high enough so that the particle images on two successive frames give particle image displacements in the measurable range.

3.2. Experimental Arrangement

Experiments performed in a large-scale water channel, using particle image velocimetry, which yields global representation of the velocity and vorticity fields. The overall experimental system and quantitative measurement techniques are described in the following section.

3.2.1. Water Channel System

Experiments will be performed in a large scale water channel which located at Lehigh University, Fluid Mechanics Laboratory, U.S.A. Free-surface water channel having a test section 927 mm wide x 610 mm deep and 4928 mm length shown in Figure 3.2.1. The water flow speed was controlled by an Ingersoll-Rand radial flow pump. The water channel test section was constructed of transparent plexiglass with upstream and downstream PVC reservoirs. An arrangements of honeycombs and screens is located upstream of the contraction to minimized the free-stream turbulence. This test section was preceded by a settling tank, a honeycomb screen arrangement, and a 2:1 contraction. The turbulence intensity at the entrance to the test section for the present free stream velocity was less than 0.3%.

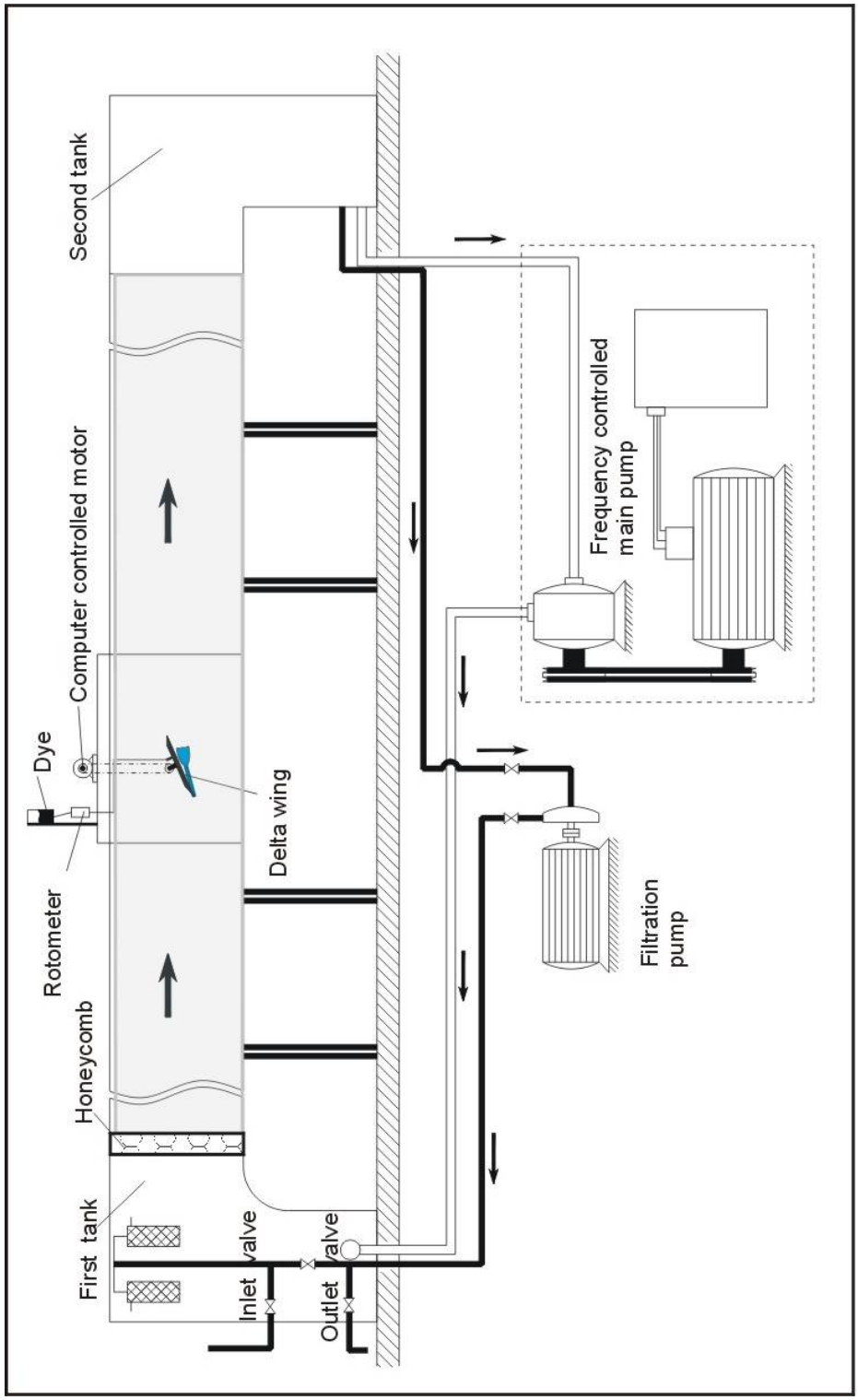


Figure 3.2.1. Schematic of the water channel with experimental apparatus

3.2.2. Experimental System

General planforms of Unmanned Combat Air Vehicles showing basic classes of trailing edge configurations alteration due to fuselage/forebody are presented in Figure 3.2.2. All of them typically have a low to moderate values of sweep angle. In the present study, The UCAVs except Boing model are examined in detail.Based on these considerations, the sweep angle of the wing was specified as Λ = 38.7°. The chord C was 101.6 mm and the total span at the trailing-edge was 254 mm. The thickness of the wing was 3 mm, and its leading-edges were beveled on the windward side at an angle of 30°. For all experiments, the value of Reynolds number based on chord C was maintained at 10,000, which corresponded to a freestream velocity U = 98.8 mm/sec. The wing was maintained in a nominally horizontal position by a slender support strut that extended vertically from the midchord of the wing. This strut had a width of 4 mm and a streamwise length of 35 mm. Assessment of this type of strut arrangement involved comparison with complementary experiments involving a nominally horizontal sting and comparison of the location of vortex breakdown for wings of different sweep angle. As a consequence, this strut arrangement had an insignificant effect on the flow structure on the leeward side of the wing. Experimental system considering with instrumentation and test chamber is clearly shown in Figure 3.2.3.

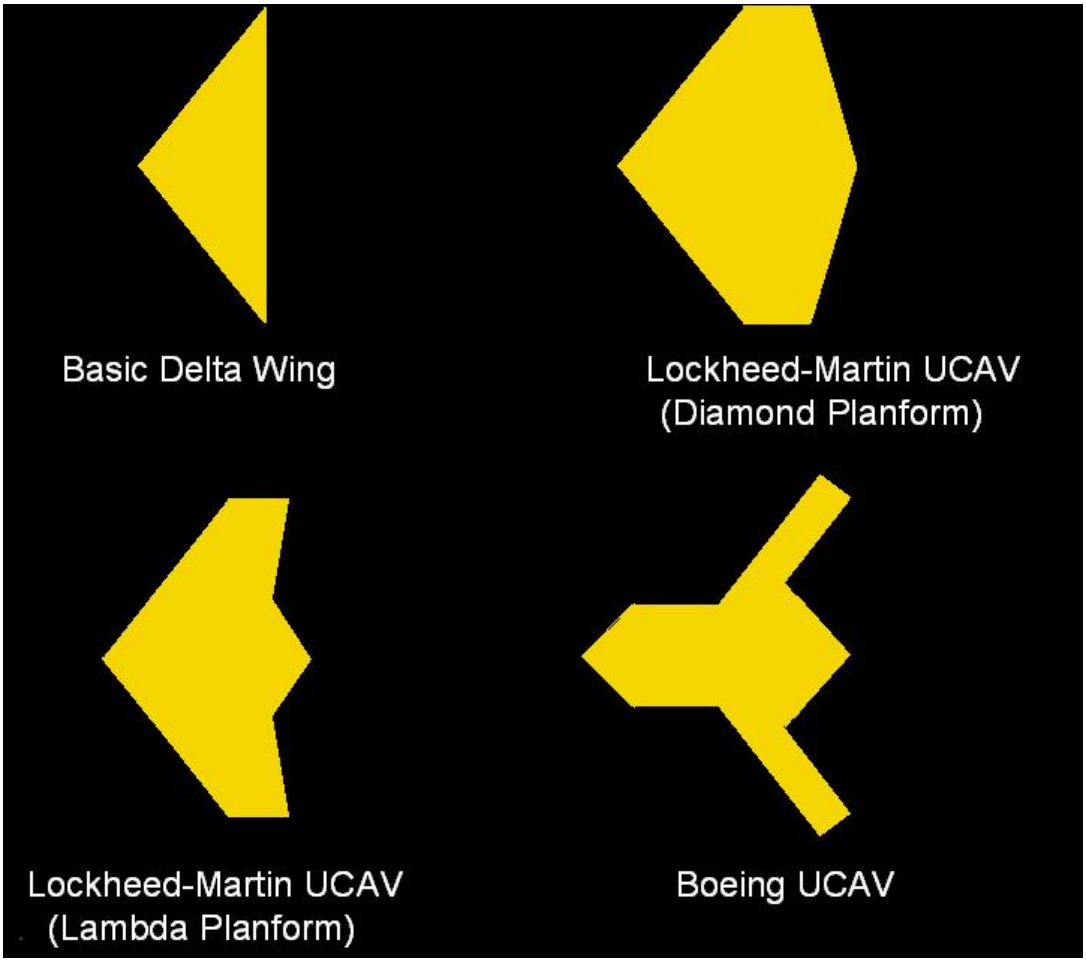


Figure 3.2.2. General planforms of Unmanned Combat Air Vehicles showing basic classes of trailing-edge configurations alteration due to fuselage/forebody.

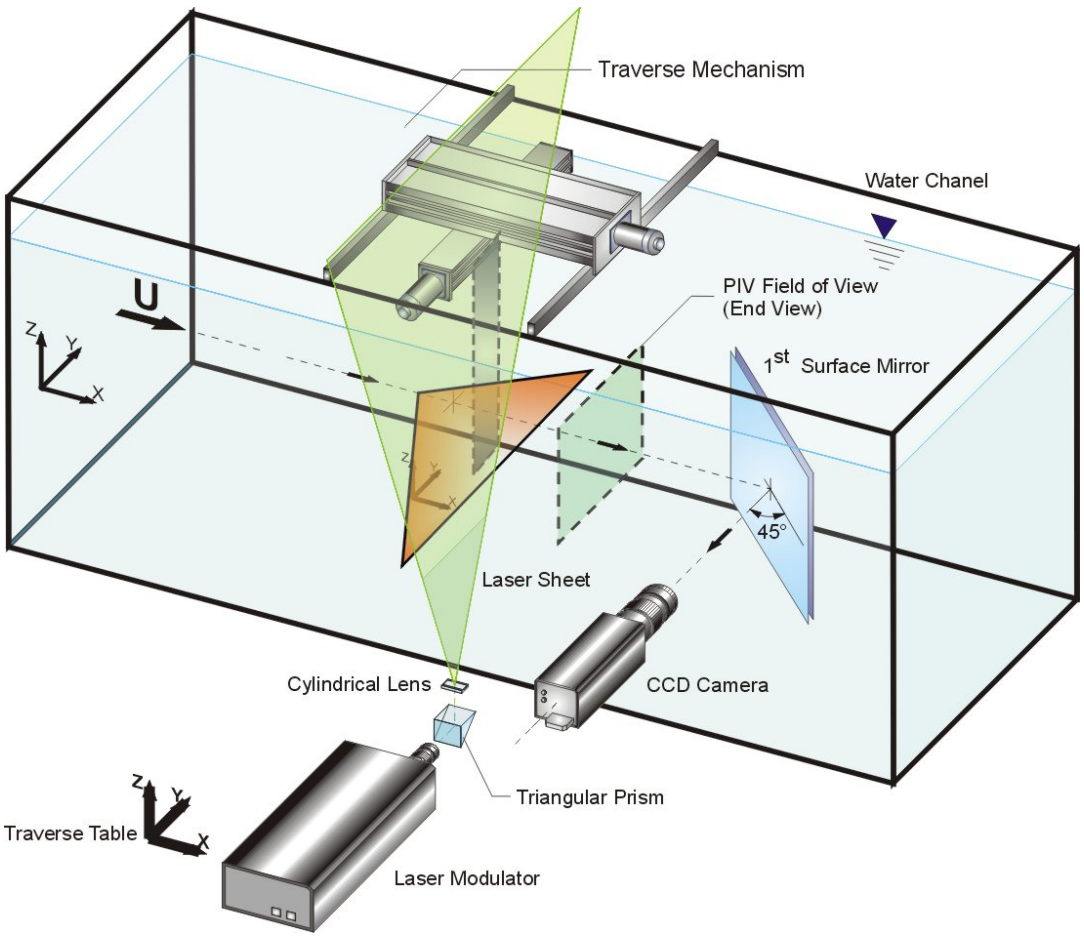


Figure 3.2.3. Instrumentation and test chamber

An overview of the laser sheet location, relative to the delta wing, is provided in Figure 3.2.4. For the present investigation, it was determined, on the basis of preliminary experiments with dye, that the major features of the flow structure could be the best determined at the streamwise location x/C = 0.8, and therefore this position of the laser sheet is employed in the present study. Furthermore, preliminary dye visualization, as well as initial PIV experiments, showed that the characteristic states of the flow structure were well represented by angles-of-attack α = 7°, 13°, 17° and 25°, and therefore these values were employed for detailed imaging. This dye visualization indicates that the axis of the vortex core region was at an angle of 30º with respect to the plane of symmetry of the wing. Therefore, the angle between the nominal axis of the vortex core region and the aforementioned plane of the laser sheet was therefore 60º, rather than an angle of 90º, which would correspond to perfect alignment of the axis of the vortex and the surface normal of the plane of the laser sheet. The patterns of flow topology characterized in the plane of the laser sheet must therefore be viewed as those on a skewed plane. This skew angle may alter the affected locations of certain critical points of the topology, relative to the locations deduced from viewing on a plane orthogonal to the axis of the vortex. A further aspect of the field of view corresponding to the plane of the laser sheet is that the flow structures was characterized over half the wing, rather than the entire spanwise extent of the wing, in order to maximize spatial resolution of the measurements. As a consequence, it is not possible to monitor time-dependent variations of the processes of vortex breakdown and stall on opposing sides of the wing.

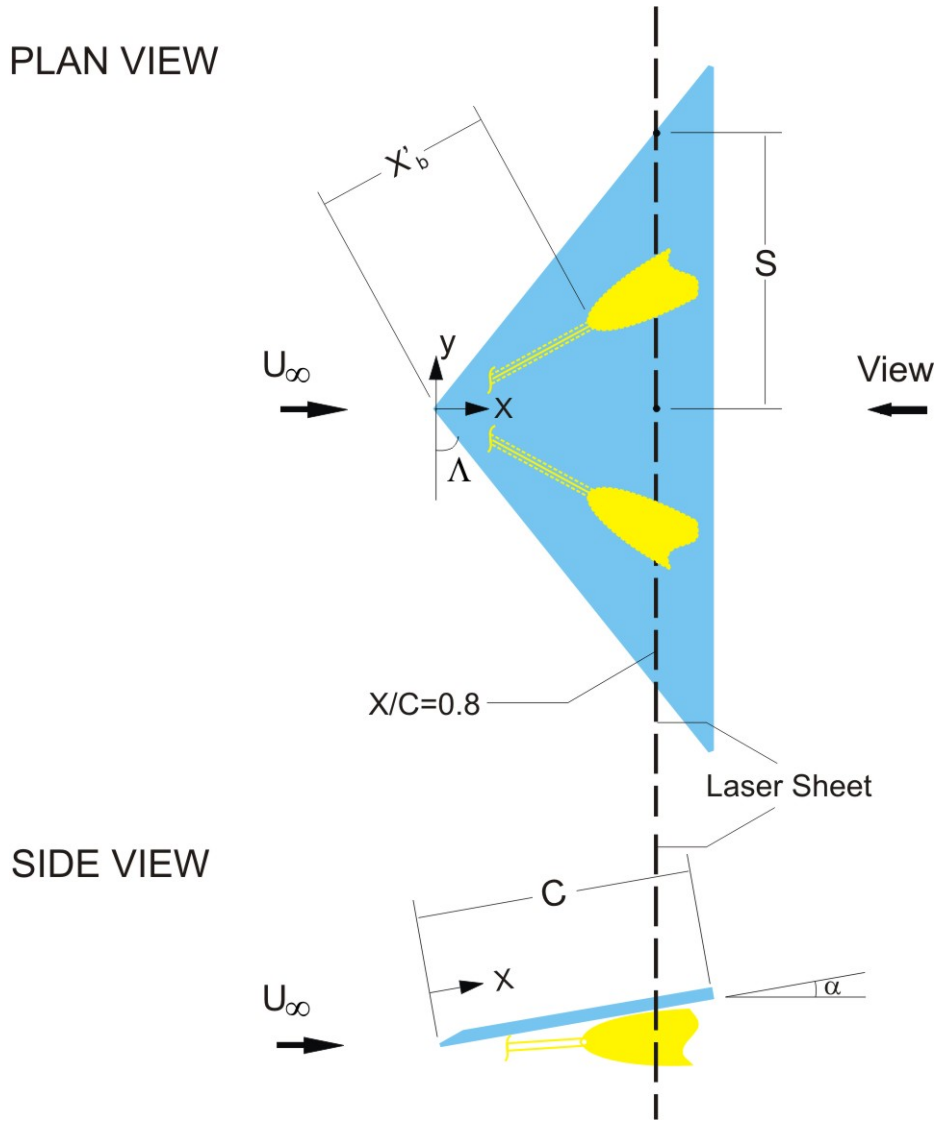


Figure 3.2.4. Schematic of experimental arrangement showing delta wing, laser sheet location, and definition of key parameters.

The wings involved two basic planforms designated as diamond and lambda; they are shown in Figures 3.2.5. and 3.2.6. These Figures show the system coordinates and critical length scales for each of the wings. The fore regions of the wings were matched. That is, the delta wing portion of the leading region of each wing, having a chord $C' = 101.6$ mm, was maintained the same for each planform, in order to allow a direct comparison of the consequence of trailing-edge configuration on the flow development. The chords C of the diamond and lambda wings had

values respectively of 195 mm and 167 mm. This dimension C allows determination of all other dimensions of the wing via the schematics of Figure 3.2.6. In addition, each wing had a thickness t of 3 mm, and was beveled on the windward side at an angle of 30°. The value of Reynolds number based on chord C was maintained at 10,000 for both wings. The corresponding values of free-stream velocity for the diamond and lambda wings were U_∞ = 51.4 mm/sec and U_∞ = 60.1 mm/sec respectively. The employed values of angle-of-attack were α = 7°, 13°, 17° and 25°.

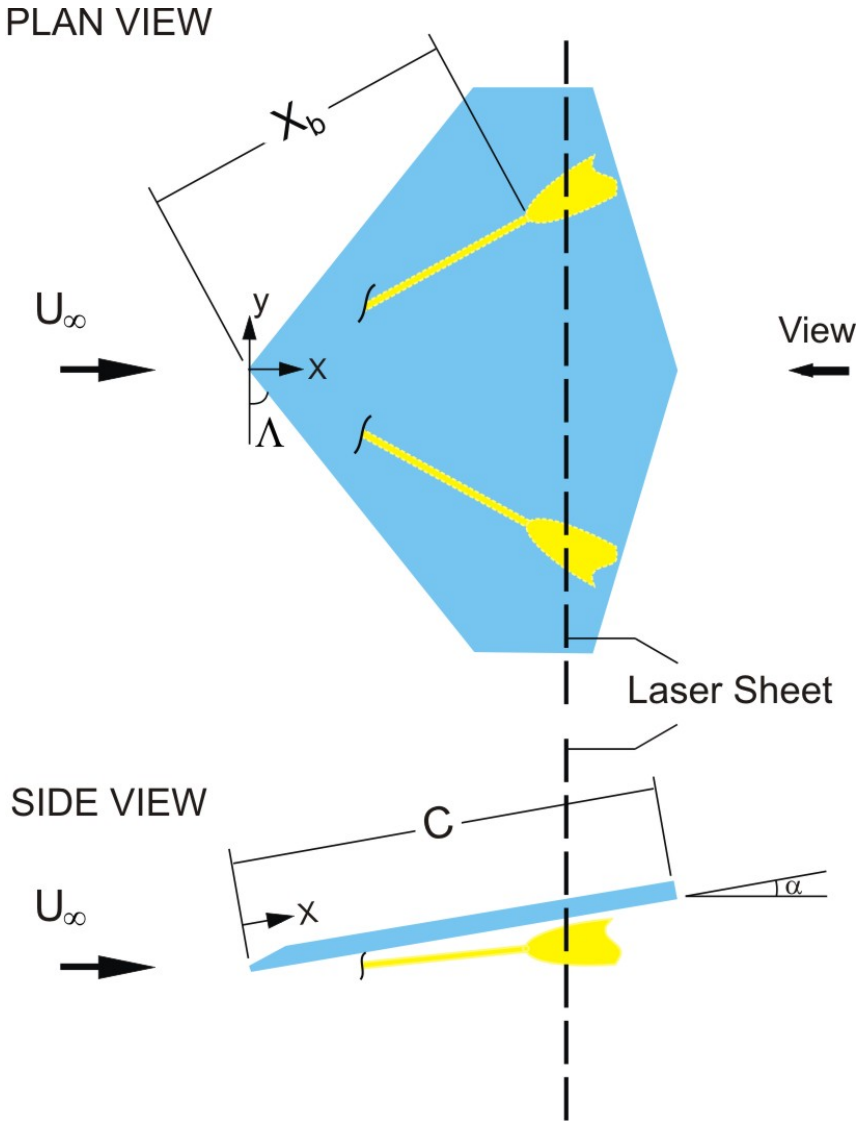


Figure 3.2.5. Simplified schematic of experimental arrangement of diamond planform.

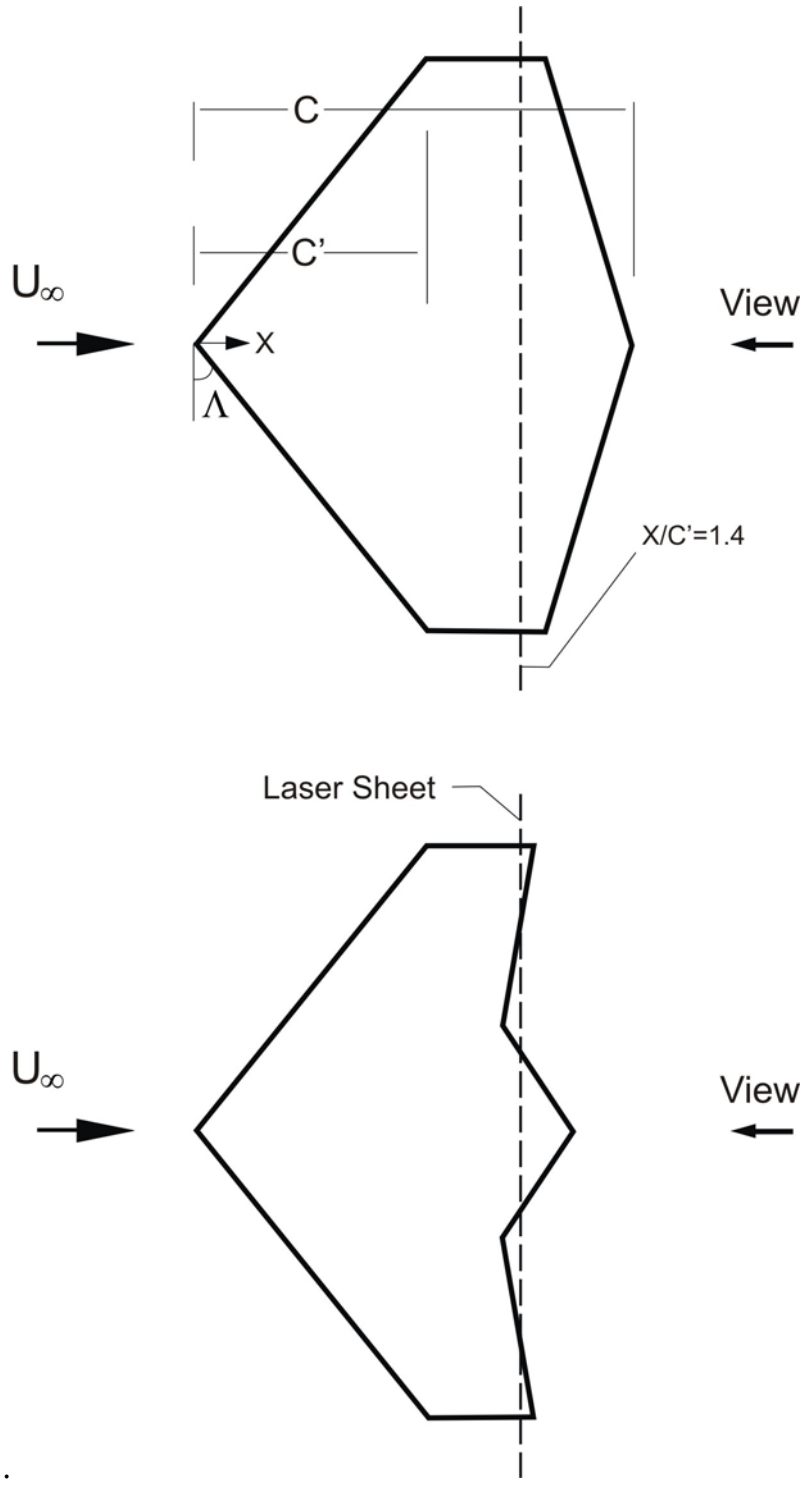


Figure 3.2.6. Direct comparison of diamond and lambda planforms and locations of laser sheets employed for quantitative imaging.

The colinear beam from this dual system was transmitted through a system of cylindrical and spherical lenses, in order to generate a vertical laser sheet, which illuminated a desired crossflow plane, as indicated in Figure 3.2.5. The laser sheet was located at the trailing-edge; in this region, it is anticipated that the unsteady (buffet) loading will be severe. This location corresponds to the streamwise distance $x / C' = 1.4$, in which C' is the chord of the leading delta wing configuration in each of the planforms, as designated in Figure 3.2.6. Based on preliminary dye visualization, it is estimated that the angle between the centerline of the predominant leading-edge vortex and the plane of the laser sheet is 60º. The flow was seeded with 12 micron, metallic-coated, hollow plastic spheres, which were essentially neutrally buoyant. Patterns of these particle images were recorded on a high-resolution camera, having 1,024 pixels × 1,024 pixels. The effective framing rate of the camera was 15 cycles per second. This framing rate, relative to the characteristic frequencies of the major events of the flow structure allowed a technique of cinema PIV for determination of spectra and cross-spectra of the fluctuating flow field.

The pattern of instantaneous velocity vectors was obtained by a cross-correlation technique involving successive frames of the patterns of particle images. Two sizes of interrogation windows were employed: 32 × 32 pixels and 16 × 16 pixels. In both cases, an effective overlap of 50% was employed, in order to satisfy the Nyquist criterion. The effective grid size for the larger interrogation window, in the plane of the laser sheet, was 2.65 mm. In order to ensure that the high-image-density criterion was satisfied, the number of particle images within the interrogation window was, at minimum, 15 to 20.

3.3. Image Acquisition

Quantitative visualization of the flow patterns was attained using a method of high-image-density particle image velocimetry. Illumination was in the form of a 1mm thick laser sheet which was generated from two Nd:Yag pulsed lasers fitted with a cylindrical–spherical lens system. Each laser of the dual system had a power rating of 90 mJ.

A time sequence of 200 images was acquired at a frequency of fifteen frames per second. This set of instantaneous images could be time-averaged or, by using a selected, coherent event of the instability adjacent to the plate, a phase-average of the flow pattern was acquired. Post-processing involved a combination of instantaneous time-averaged and phase-averaged representations of velocity, vorticity and Reynolds stress. Furthermore, by employing concepts of spectral and cross-spectral analysis of the sequence of PIV images, it was possible to obtain amplitude and phase distributions of the organized fluctuation across the shear flow.

The PIV images were recorded in the cinema mode, at an effective framing rate of 15 frames per second. Since the maximum frequency of interest in this investigation corresponded to a coherent oscillation at $f_0 \leq 1\,Hz$, it was possible to perform spectral analysis. At a specified location, xy in the flow field, it was possible to construct the time variation of the desired velocity fluctuation by considering a total of 200 PIV images, which represents 200 sample points. This single record, without averaging, was employed to determine the spectrum. A Hanning window was employed during the spectral analysis.

The flow is seeded with 12 micron, metallic coated hollow plastic spheres, which were essentially neutrally buoyant. The silvered coated hollow particles were mixed in a one liter container, then poured in to the water channel. Then, the water channel was run at maximum speed for a period of several minutes, in order to ensure that particles were uniformly dispersed throughout the water. TSI PIVCAM 10-30 CCD digital camera, having a resolution of 1024 × 1024 pixels, allowed acquisition of the patterns of particle images. The camera was equipped with NIKON AF Micro Nikkon 55 mm focal–length lens. The CCD camera and lasers were

connected to a PC via a TSI Laser pulse synchronizer control system which could control the timing of data acquisition. Patterns of particle images were acquired at a rate of 15 frames pairs per second. A Hart correlation technique was employed to determine the velocity fields. The basic principle of Hart Correlation is that each interrogation spot image is first compressed based on a threshold defined by the user as compression ratio. The intensity information on the compressed images is then put into an encoded form and correlation function is performed on the encoded information. The Hart Correlation is also applied in a progressive fashion to allow the reduction of interrogation spot size for high spatial resolution. A double correlation technique is also used to increase signal -to-noise ratio for the correlation function so that the correct velocity measurements can be made more robustly. The Hart Correlation allows interrogation spot size to be as small as 4 pixels to be analyzed so that vector field with very high spatial resolution can be obtained.

The pattern of velocity vectors was calculated by performing a cross-correlation of the patterns of particle images in each frame pair. During this interrogation, windows of 32 × 32 pixels and 16 × 16 pixels were employed. In order to ensure that the criterion for high-image-density was satisfied, the number of particle images within the interrogation window was, at minimum, 15 to 20. Furthermore, during the interrogation process, these windows were overlapped by 50% in order to satisfy the Nyquist criterion. The field of view for the velocity vectors is indicated in conjunction with each Figure.

The images were acquired using TSI's INSIGHT 3.0 software. The PIV images by the CCD camera were digitized by an image processing board, then transferred to a PC for image processing and display on a PC monitor.

Post processing refers to the analysis of the velocity vector field after the vectors have been extracted from the PIV image. Post processing consists of two basic functions vector editing, and computing flow properties. Vector editing is necessary because some wrong peaks may be chosen as the velocity peak. In vector fields with 1,000 points, ninety-nine percent correct vectors still gives 10 wrong vectors. During the image processing the signal-to-noise ratio at each spot must pass the threshold values to be considered a valid peak. Usually these thresholds are set to

filter out most of the bad points, but if the thresholds are too high to filter out all the bad points, many good points are also eliminated.

In post processing, the vectors are compared against the neighboring vectors. Vectors that vary by more than the validation tolerance from the neighborhood average are removed. This neighborhood check enforces continuity on the flow. Places that are left empty can be filled in by interpolating the neighboring vectors to get the best estimate of the velocity at that point. After the vector has been validated and the missing points filled in, the properties of the flow can be computed. Measuring the flow properties like vorticity from the accurate vector field data is one the key reasons for performing PIV measurements. The post-processing module computes vorticity, Reynolds stresses, and the velocity magnitude.

CLEANVEC PIV vector validation software, which is developed by Steven M. Soloff and Prof. Carl D. Meinhart is used for removing bad vectors. After the removing bad vectors, the Fortran program NFILVB (Lin 1994) interpolated between the vectors and fill the blank locations using interpolation. The velocity field was smoothed using a Gaussian filter having an exponent p = 1.3. These interpolation and filtering techniques are well known and described in detail by Landreth and Adrian. (1989). The sampled-averaged velocity field was obtained using in-house program NWENSAV2 (Lin, 1996)

4. RESULTS AND DISCUSSIONS

4.1. Flow Structure on a Delta Wing of Low Sweep Angle

4.1.1. Dye Visualization

Representative dye visualization is shown in Figure 4.1.1 for the case of the stationary wing at three values of angle-of-attack α. At the lowest two values of α = 7° and 13°, dye was injected from two localized ports on the windward surface located close to the apex of the wing. At α = 7°, the apparent centerlines of the leading-edge vortices are designated as in Fig. 4.1.1, and it is clear that initial disruptions of the marker can occur, at locations of the order of 0.3C to 0.5C, in which C is the chord of the wing. At locations sufficiently far downstream, at x/C = 0.6 to 0.8, a large-scale widening of the marker occurs. This two-stage process of vortex breakdown, i.e., an initial disruption, then a large-scale widening, has a remarkably similar form to the computations of Gordnier and Visbal (2003) for a wing of low sweep angle Λ = 50º. This overall pattern of vortex breakdown therefore appears to be an inherent feature of the flow structure on wings of low sweep angle.

At α = 13°, the streamwise extent of the organized portion of the dye marker emanating from the apex is very short. The central portion of the wing is unmarked by dye, since it is continuously swept downstream past the trailing-edge. On the other hand, the regions of the wing outboard of this central portion show a low velocity region of dye adjacent to the surface.

At 17°, the entire wing is filled with a region of low velocity dye, as shown in the lower left image of Figure 4.1.1. In presence of an applied, small-amplitude perturbation, shown in the lower right image, the flow structure of the visualized pattern at α = 17° resembles, in a general sense, the structure at α = 13° on the stationary wing. Taken together, the foregoing visualizations suggest overall features

of the flow patterns, which are addressed herein using quantitative imaging of the instantaneous and averaged flow structure.

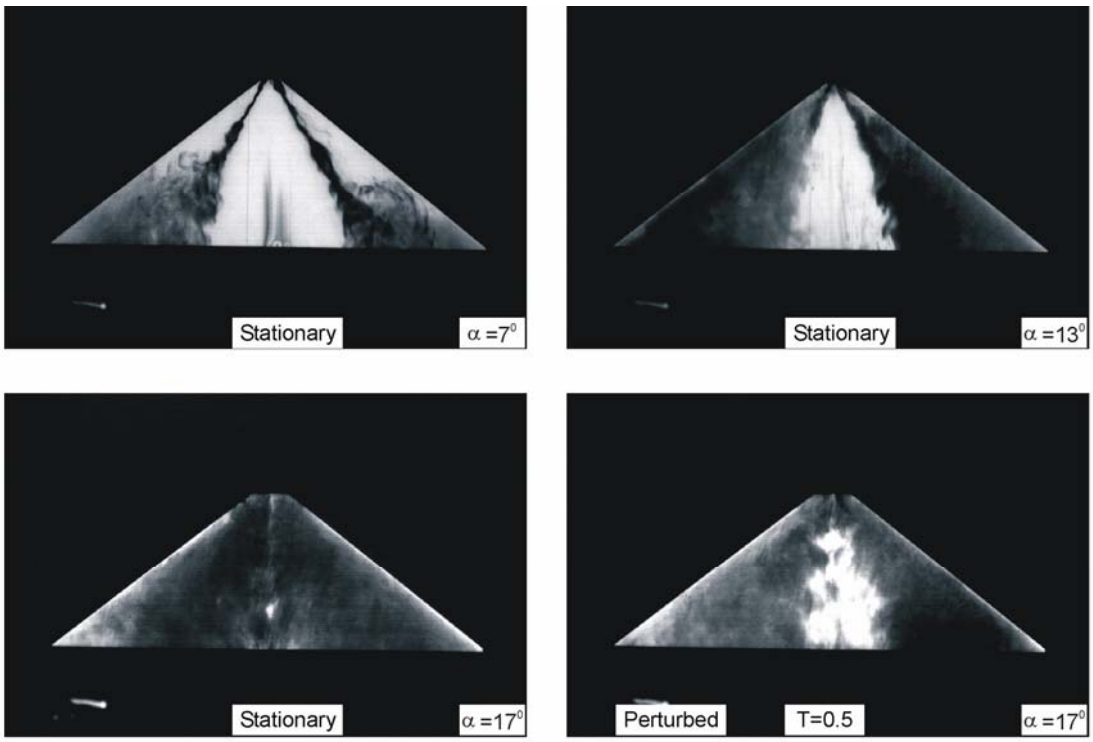


Figure 4.1.1. Dye visualization at three representative angles-of-attack. For images α = 7° and 13°, dye is injected through two discrete ports at the apex of the wing, while at α = 17°, dye is injected along the leading-edge on the windward side of the wing. For the perturbed wing, the perturbation amplitude and period are α_o = 1° and T = 0.5 sec.

Gursul et al. (2005) has stated that Yaniktepe and Rockwell (2004) identify three distinct stages in the breakdown process. In region I small scale undulations of the vortex core filament are evident. Gordnier and Visbal (2003) point out that this spiralling is associated with the vortex core motion driven by the shear layer instabilities and not with the onset of vortex breakdown. Therefore, the initiation of spiraling of the streakline may not be used to identify the onset of vortex breakdown. The beginning of region II marks the location of the onset of vortex breakdown. Region II is characterized by a small scale bubble or thickening of the vortex filament which is terminated at its downstream end by a pinch off region where the diameter again becomes small. This is followed in region III by an abrupt expansion of the breakdown region where the particles are diffused over a broad area covering the outboard half of the wing. Comparison of results of these manuscripts are shown in Figure 4.1.2.

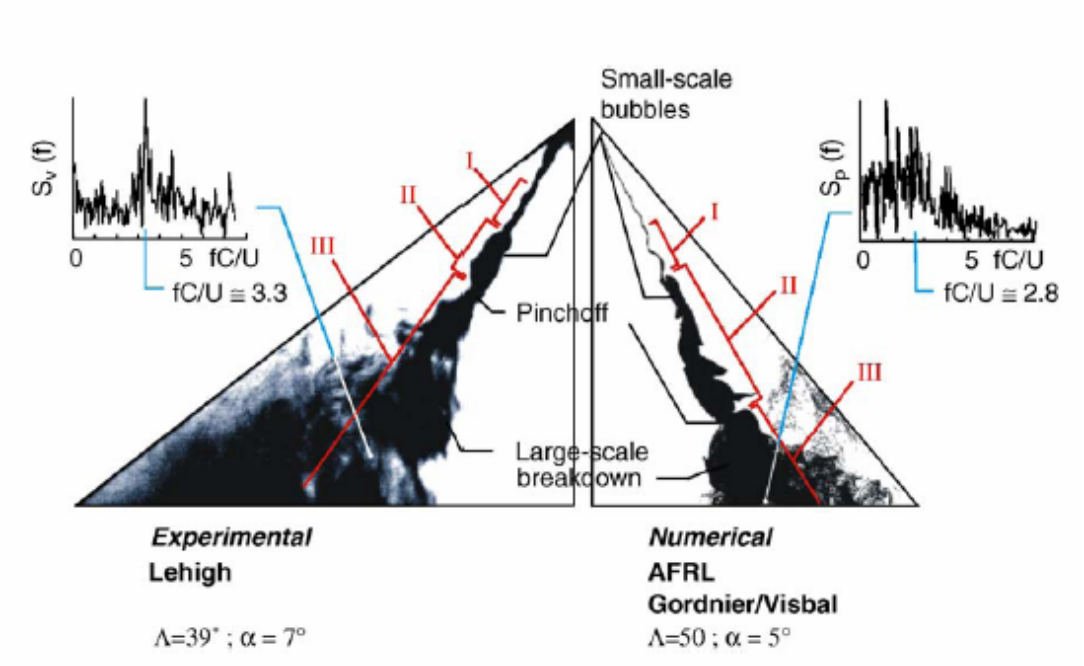


Figure 4.1.2. Comparison of dye visualization of Yaniktepe and Rockwell (2004) and the computational streakline of Gordnier and Visbal (2003)

4.1.2. Averaged Velocity and Streamline Topology

Figure 4.1.3 shows patterns of time-averaged velocity $< V >$ and streamlines $< \Psi >$ corresponding to the flow structure at x = 0.8 C. In this and subsequent Figures, the semi-span S corresponds to the local value of S at a given value of dimensionless chordwise distance s/C; it does not have a single value corresponding to the value of the semi-span at the trailing-edge x/C = 1. In Figure 4.1.3 and subsequent Figures, the fact that only a fraction of the local semi-span S is shown arises from the variable zoom during the image acquisition. Comparison with the dye visualization image of Figure 4.1.1 shows that the chordwise location x/C = 0.8 lies within the region. In Figure 4.1.3 and subsequent Figures, the fact that only a fraction of the local semi-span S is shown arises from the variable zoom during image acquisition.

Comparison with the dye visualization image of Figure 4.1.1 shows that the chordwise location x/C = 0.8 lies within the region of significant disruption of the dye marker at α = 7°, and is well downstream of the substantial widening of the dye marker at α = 13°. At α = 17° and 25° (not shown), dye simply floods the surface of the wing, which suggests that the region near the surface flow pattern on the wing is fully stalled. Remarkably, however, all of the patterns of Figure 4.1.3 show a definable time-averaged structure.

At α = 7° through 17°, an identifiable interface exists between a region of high velocity flow below the wing and very low velocity immediately adjacent to the wing. In other words, at this interface, this velocity field is characteristic of a separated free-shear layer. At α = 25°, the interface region has a different form, and the spatial extent of the very low velocity region is confined to a domain very close to the surface of the wing. Unlike cases at low angle-of-attack, the interface does not correspond to an abrupt decrease of velocity between the exterior flow and the region of flow closer to the wing. Rather, the magnitude of velocity is of the same order on either side of the interface.

The corresponding streamline topology, which is constructed from these averaged velocity fields, indicates a saddle point at α = 7°, which is designated by a

circular dot. It appears well below and slightly outboard of the leading-edge of the wing. Furthermore, the streamline pattern inside the major streamlines that connect to the saddle point does not exhibit a well-defined swirl pattern. All of these features of the streamline topology are distinctly different from those associated with wings having relatively high sweep angle, as characterized by Magness et al. (1993).

At α = 13°, the aforementioned saddle point has been displaced downward, and lies outside of the field of view. A well-defined swirl pattern exists. It does not emanate however, from the leading-edge of the wing. Rather, it appears to originate from a saddle point located at the position of the black dot. This displacement from the leading-edge of the wing is due to the extensively separated flow, evident by comparison with the dye visualization at α = 13° in Figure 4.1.1. A similar saddle point, which is displaced inboard from the leading-edge, is indicated by the black dot in the streamline topology at α = 17°. Finally, at α = 25°, an identifiable swirl pattern is barely evident and the entire streamline topology takes on an unconventional form, due to the highly stalled flow over the surface of the wing.

4.1.3. Patterns of Averaged Vorticity and Fluctuating Velocity

In Figure 4.1.4, patterns of time-averaged vorticity $<\omega>$ are compared with the root-mean-square of the transverse (vertical) velocity fluctuation w_{rms} normalized by the free-stream velocity U, i.e., w_{rms}/U, as well as with the Reynolds stress correlation $<v'w'>/U^2$, for angles-of-attack α = 7°, 13°, 17° and 25°.

In order to allow direct comparison, the minimum and incremental values of all contour patterns of averaged vorticity $<\omega>$ in Figure 4.1.4 are maintained the same at all values of α = 7°, 13°, 17° and 25°. Similarly, the same minimum and incremental values are maintained for the contours of w_{rms}/U and $<v'w'>/U^2$.

Consider, first of all, the patterns of averaged vorticity $<\omega>$ at α = 7° and 13°. They take the form of an elongated layer with one or two vorticity extrema. Comparison with Figure 4.1.3 shows that, along each of these layers, the maximum value of vorticity $<\omega>$ corresponds to the interface between regions of high and

low velocity in the corresponding plots of averaged velocity $< V >$ at $\alpha = 7°$ and 13°. That is, the elongated layers are characteristic of a free-shear layer as viewed in this crossflow plane. Furthermore, the pattern of $< \omega >$ at $\alpha = 17°$ in Figure 4.1.4 has a generally similar form, but the loci of maximum vorticity are at a less well-defined interface between higher and lower velocities. It is evident that, however, at this larger angle-of-attack, the peak value of vorticity is not as large as at $\alpha = 7°$ and 13°. Finally, at the largest angle-of-attack $\alpha = 25°$, the form of the vorticity pattern $< \omega >$ is fundamentally different. The elongated region of vorticity no longer appears to emanate from the leading-edge of the wing. Furthermore, the peak values of vorticity no longer occur at the interface referred to in the pattern of $< V >$ at $\alpha = 25°$ in Figure 4.1.3. Remarkably, the peak values of vorticity are further reduced from those at $\alpha = 17°$.

It is appropriate to compare the elongated layers of vorticity <ω> at, for example, α = 7º and 13º in Figure 4.1.4, with the corresponding patterns of streamline topology in Figure 4.1.3. The location of an extremum of vorticity is not always coincident with the focus (apparent center) of the streamline pattern and, furthermore, the spatial extent of the large-scale swirl pattern of streamlines is substantially larger than the thickness of the elongated vorticity layer. These observations are apparently due to the very rapidly distorting flow that separates from the leading-edge of the wing and, in fact, directly analogous patterns of averaged vorticity and streamline topology, including the lack of precise correspondence between them, that have been observed in the very near-wake of a cylinder, where the plane of observation is orthogonal to the axis of the separating shear layer. As shown, for example, by Akilli and Rockwell (2002), an elongated vorticity layer, which does not culminate in a single, large-scale vortical structure, is nevertheless associated with a pattern of streamline topology having a well-defined swirl pattern with a focus.

The aforementioned values of vorticity $< \omega >$ are related to the normalized component of vertical velocity fluctuation w_{rms}/U, at least for the lower values of angle-of-attack α = 7°, 13°, and 17°. For these values of α, the locations of

maximum values of w_{rms}/U can be tracked as a function of spanwise distance along each elongated pattern of w_{rms}/U. These maxima generally follow the peak values of $<\omega>$. That is, the largest velocity fluctuations occur in the region of maximum vorticity, and thereby at the interfaces in the patterns of $<V>$ shown in Figure 4.1.3.

In turn, the patterns of velocity fluctuation w_{rms}/U are associated with the Reynolds stress correlation $<v'w'>/U^2$, i.e., with the degree of turbulence production in the free shear flow, at least at angles-of-attack α = 7°, 13°, and 17°. The largest values of $<v'w'>/U^2$ tend to occur approximately at half the semi-span S, i.e., at 0.5 S for all values of angle-of-attack α = 7° through 17°. The loci of extrema of the correlation $<v'w'>/U^2$ are generally in accord with the maxima of w_{rms}/U. In fact, the peak magnitude of the correlation $<v'w'>/U^2$ increases with angle-of-attack α = 7° through 17°.

At the highest angle-of-attack α = 25°, the patterns have a fundamentally different form. The pattern of w_{rms}/U is substantially broader than at lower angle-of-attack and, moreover, the peak value is substantially lower than at α = 17°. Regarding the corresponding Reynolds stress correlation $<v'w'>/U^2$, its value is substantially lower than at α = 17°. This remarkable attenuation of the fluctuating velocity magnitude and the corresponding Reynolds stress correlation is associated with the radical change of the pattern of velocity $<V>$ and streamline topology $<\Psi>$ shown at α = 25° in Figure 4.1.3. In essence, the loss of identity of the shear layer interface and the elongated vorticity layer emanating from the leading-edge of the wing, which are present at lower angle-of-attack α = 7° through 17°, yield a substantial reduction in the magnitude of the fluctuating velocity field.

4.1.4. Instantaneous Patterns of Vorticity

The patterns of velocity fluctuation w_{rms}/U and Reynolds stress correlation $<v'w'>/U^2$ described in Section 4.1.3 are intimately related to the patterns of instantaneous vorticity and their evolution with time. Figure 4.1.5 shows two randomly selected patterns of instantaneous vorticity at each angle-of-attack α = 7°

through 25°. At α = 7°, the individual vorticity concentrations retain their identity along the surface of the wing. That is, interaction between concentrations is not evident. This pattern is also evident in Figure 4.1.4, in a smoothed version, due to the effects of time-averaging of fluctuations, or jitter, of the instantaneous locations of the vorticity concentrations. It is remarkably similar to that on a wing of low sweep angle (Λ = 50°) at low angle-of-attack (α = 5°) computed by Gordnier and Visbal (2003). In Figure 4.1.5, at α = 7°, the typical wavelength between these concentrations is λ/S = 0.25, in which S is the semi-span of the wing at the chordwise location of interest herein, x/C = 0.8. On the other hand, at α = 13°, smaller-scale vorticity concentrations, with a smaller wavelength λ/S = 0.15 are formed immediately after separation from the leading-edge of the wing. Note that these concentrations do not form directly from the edge, but are initially identifiable along the surface of the wing inboard of the edge. In fact, this feature is even more prevalent at high values of α = 17º and 25º. Further inboard, larger-scale clusters of vorticity appear. At α = 17°, the initially-formed concentrations also have a relatively small wavelength, which is not as clearly defined as at lower α. The change in the patterns of instantaneous vorticity ω at successive values of α = 7°, 13°, and 17° is associated with a substantial increase in both velocity fluctuation amplitude w_{rms}/U and Reynolds stress correlation $< v'w' > /U^2$, which is evident from cross-comparison of the images at α = 7°, 13°, and 17° in Figure 4.1.4.

On the other hand, at the highest angle-of-attack α = 25°, defined clusters of vorticity are first detectable at a significant distance inboard from the leading-edge. Such patterns are associated with relatively low values of the Reynolds stress correlation $< v'w' > /U^2$ and velocity fluctuation w_{rms}/U, evident at α = 25° in the images of Figure 4.1.4. The occurrence of large-scale stall at α = 25º therefore results in a reduction in level of the unsteadiness, relative to lower values of α where a well-defined separated shear layer, i.e., vorticity layer, is located adjacent to the surface of the wing.

4.1.5. Spectra Along Separated Vorticity Layer

As shown in Figure 4.1.4, the elongated vorticity layers from the leading-edge are associated with corresponding patterns of vertical velocity fluctuation amplitude w_{rms}/U, and at lower values of angle-of-attack α, the peak values of w_{rms}/U follow the peak values of averaged vorticity $< \omega >$. In Figure 4.1.6, for each value of angle-of-attack α, spectra of the transverse (vertical) velocity fluctuation were evaluated at successive locations along the locus of maximum w_{rms}/U. These locations are indicated by the solid black points on each of the patterns of w_{rms}/U for angles-of-attack $\alpha = 7°$, 13°, 17° and 25°.

At $\alpha = 7°$, the frequency f_o of the spectral peak is at $f_o = 3.4$ Hz, and the largest amplitude of this spectral peak occurs at the maximum of w_{rms}/U, which is well inboard of the leading-edge. Then, as the surface of the wing is approached, this peak is rapidly attenuated, and barely detectable. The form of these spectra is directly related to the patterns of instantaneous vorticity concentrations, as shown at $\alpha = 7°$ in Figure 4.1.5.

At $\alpha = 13°$, the spectral peak closest to the leading-edge, which is relatively broad, is initially centered at $f_o = 4.6$ Hz. For increasing distance along the vorticity layer, peaks at lower values of f_o are evident; they lie in the range $2.4 \leq f_o \leq 3.2$ Hz. This lowering of the peak frequency f_o is consistent with the occurrence of larger-scale vortical structures shown at $\alpha = 13°$ in Figure 4.1.5.

Similarly, at $\alpha = 17°$, the initial, broad spectral peak has a relatively high center frequency $f_o = 4.1$ Hz. Further along the layer, two peaks are evident at $f_o = 2.1$ and 3.2 Hz and, finally, a relatively low frequency component is apparent at $f_o = 0.5$ Hz, as the shear layer approaches the surface of the wing. This successive lowering of the values of f_o is again associated with the occurrence of larger-scale vortical structures along the shear layer.

At the highest angle-of-attack $\alpha = 25°$, a reasonably defined, somewhat broadband peak is detectable at a location well inboard of the leading-edge. This predominant peak is centered at $f_o = 3.4$ Hz, and moves to a lower value of $f_o = 2.5$

Hz further along the layer. At this high angle-of-attack, it is apparent that the occurrence of larger-scale vortical structures along the separated vorticity layer still plays a role in shifting the broadly defined peak at f_o to lower frequencies.

Viewing the patterns of spectra at all values of α in Figure 4.1.6, it is evident that, at the smallest angles-of-attack $\alpha = 7°$ and 13°, the eventual reattachment of the shear layer to the surface of the wing, evident in patterns of averaged velocity of Figure 4.1.3 and vorticity of Figure 4.1.4, is associated with attenuation of the predominant spectral peak. At a sufficiently high angle-of-attack, $\alpha = 17°$, this tendency towards reattachment is associated with the appearance of a very low frequency. At $\alpha = 25°$, such reattachment does not occur and a defined, but relatively broadband, peak persists.

The dimensionless frequencies of the spectral peaks at f_o can be expressed as f_oC/U. For the spectra of Figure 4.1.6, the identifiable spectral peaks in the early stages of development of the shear layer are in the range $3.3 \leq f_o \leq 4.6$ Hz, which correspond to $3.39 \leq f_oC/U \leq 4.73$. Further along the separated layer, where larger-scale clusters of vorticity occur, the range of values is lower, i.e., $0.5 \text{ Hz} \leq f_o \leq 3.2$, which correspond to $0.51 \leq f_oC/U \leq 3.29$. This range of f_oC/U is remarkably similar to the band of identifiable frequencies in a spectrum computed by Gordnier and Visbal (2003), in the region downstream of vortex breakdown on a wing of low sweep angle $\Lambda = 50°$.

As indicated in the citations in Section 1. *Introduction*, several physical mechanisms may contribute to unsteadiness of the flow structure on a delta wing. Menke, Yang and Gursul (1999), as well as works of Gursul (1994) cited therein, provide a classification of types of unsteadiness for wings having relatively large values of sweep angle $\Lambda = 65°$ to 75°. Most relevant to our present considerations is the occurrence of: (i) vortex shedding, typically when the vortex breakdown location reaches the apex of the wing ($0.25 \leq f_o/C/U \leq 0.6$); (ii) unsteadiness associated with the helical mode of instability of vortex breakdown ($1.0 \leq f_o/C/U \leq 4$); and (iii) the small-scale Kelvin-Helmholtz instability of the shear layer separating from the leading-edge of the wing ($6 \leq f_o/C/U \leq 30$). For a wing having a relatively low

sweep angle, e.g., $\Lambda = 38.7°$ of the present study, this type of detailed classification is not available.

As indicated in the foregoing images, a classical vortex core, marked by an approximately circular region of vorticity, does not exist in the images of the vorticity layer formed from the leading-edge. It is therefore questionable that one can speak of a helical mode instability of vortex breakdown on wings of such low sweep. In fact, for the wing of relatively low sweep angle $\Lambda = 38.7°$ investigated herein, it is apparent from the dye visualization at, for example, $\alpha = 7°$ in Figure 4.1.1, that a well-defined spiral, or bubble mode of vortex breakdown, does not occur. For all values of α considered herein, the crossflow planes lie within regions of vortex breakdown and stall, and maximum amplitudes of the spectra occur well inboard of the leading-edge. For the present purposes, vortex breakdown is simply defined as a severe disruption of the core of the vortex, as evident in the dye visualization of Figure 4.1.1 at $\alpha = 7º$. This type of apparent breakdown may be associated with either jitter of the nominally stationary vortical substructures or unsteadiness associated with the fundamental or subharmonics of the inherent instability of the shear layer separating from the leading-edge.

4.1.6. Effect of Controlled Perturbations on Averaged and Instantaneous Structure

Preliminary experiments indicated that, at sufficiently high angle-of-attack, i.e., $\alpha = 17°$, the flow structure was particularly sensitive to small amplitude perturbations. On this basis, the delta wing was subjected to perturbations about its midchord. The amplitude $\Delta\alpha$ of these perturbations was kept small at $\Delta\alpha = 1°$, while the period T of the perturbation was varied. The smallest period of oscillation was $T = 0.5$, i.e., $f = 2$ Hz, which lies in the lower range of frequency $0.5 \leq f_o \leq 3.15$ of the self-excited instability, shown in the spectra of Figure 4.1.6. In fact, this value of the perturbation period corresponds to the frequency range of the coalesced, or merged, small-scale vortical structures indicated at $\alpha = 17°$ in Figure 4.1.5. More

specifically, $T = 0.5$ corresponds to the subharmonic of the highest frequency $f_o \cong 4$ Hz in the initial region of the shear layer, as shown in Figure 4.1.6. In addition, larger values of $T = 1.0$, 1.5 and 2.0 sec were applied, with $T = 2.0$ corresponding to $f = 0.5$ Hz, which is the lowest low frequency in the spectrum at the location furthest from the leading-edge along the vorticity layer, as shown in Figure 4.1.6.

Patterns of time-averaged velocity $< V >$ and $< \Psi >$ are shown in Figure 4.1.7. It is evident that the streamline topology undergoes a fundamental transformation, relative to the topology on the stationary wing, evident by comparison of the top two images of Figure 4.1.7. That is, the topology is characteristic of a typical leading-edge vortex and, in fact, comparison with the topology at $\alpha = 13°$ for the stationary wing in Figure 4.1.3, shows a close similarity to the pattern of $T = 0.5$ in Figure 4.1.7. As the period of excitation is increased to values of $T = 1.0$ and 1.5, the topology relaxes towards that of the stationary wing, i.e., the center of the spiral streamline pattern moves further inboard and becomes less defined.

These changes in the patterns of velocity $< V >$ and the streamline $< \Psi >$ topology are associated with corresponding alterations of the patterns of averaged vorticity $< \omega >$, velocity fluctuation amplitude w_{rms}/U and Reynolds stress $< v'w' > / U^2$, as indicated in Figure 4.1.8. Comparing, first of all, the patterns of $< \omega >$, it is evident that the perturbation at T = 0.5 results in a radically increased level of peak $< \omega >$, as well as an increase in the degree of organization of the distribution of $< \omega >$, relative to the pattern of $< \omega >$ for the stationary wing. At larger values of perturbation period, T = 1.0 and 1.5, this peak vorticity level decreases, and the ordered nature of the pattern is less apparent.

The increase in level of averaged vorticity $< \omega >$ at $T = 0.5$ is accompanied by a substantial increase in the peak values of the velocity fluctuation in w_{rms}/U and Reynolds stress correlation $< v'w' > / U^2$, relative to the case of the stationary wing. At the highest value $T = 1.5$, these peak values have decreased significantly, relative to those at $T = 0.5$.

The patterns of instantaneous vorticity associated with the perturbation at T = 0.5 are shown in Figure 4.1.9. It is evident that in presence of the perturbation, a relatively large-scale cluster of vorticity is formed, due to the coalescence of a number of small-scale concentrations of vorticity. This larger-scale vorticity cluster forms closer to the leading-edge of the wing than the cluster on the stationary wing. The physical mechanism for enhancement of the averaged structure described in the foregoing therefore involves more rapid development of patterns of coalesced vorticity.

Gursul et al. (2005) has explained briefly within the Figure 4.1.10. that it shows the flow visualization pictures for various forcing frequencies for amplitude of 1 deg. pitching oscillations. It is seen that the same effects, including the reattachment of shear layers and vortex re-formation, are observed with increasing frequency. A direct comparison, of which forcing mechanism (symmetric versus antisymmetric) is more efficient, is not possible as the leading-edge velocity perturbations are vastly different in their geometric form. Nevertheless, the results show that symmetric perturbations also promote reattachment and vortex reformation. They also stated that Yaniktepe and Rockwell (2004) showed that, for even lower sweep angle of $\Lambda = 38.7^{o}$, the effect of small perturbations (1^{o} pitching oscillations) is substantial as shown in Fig. 4.1.7. for $\alpha = 17^{o}$, which produces stalled flow for the stationary wing. The most effective frequency of excitation (T=0.5) corresponded to the subharmonic of the broadband fluctuations in the region of the shear layer closest to the leading-edge in this case. The optimum period T = 0.5, which corresponded to fC/U = 2.06, was also the smallest period of oscillations tested in these experiments. It is seen that forcing at this frequency produces a flow pattern characteristic of a typical leading-edge vortex.

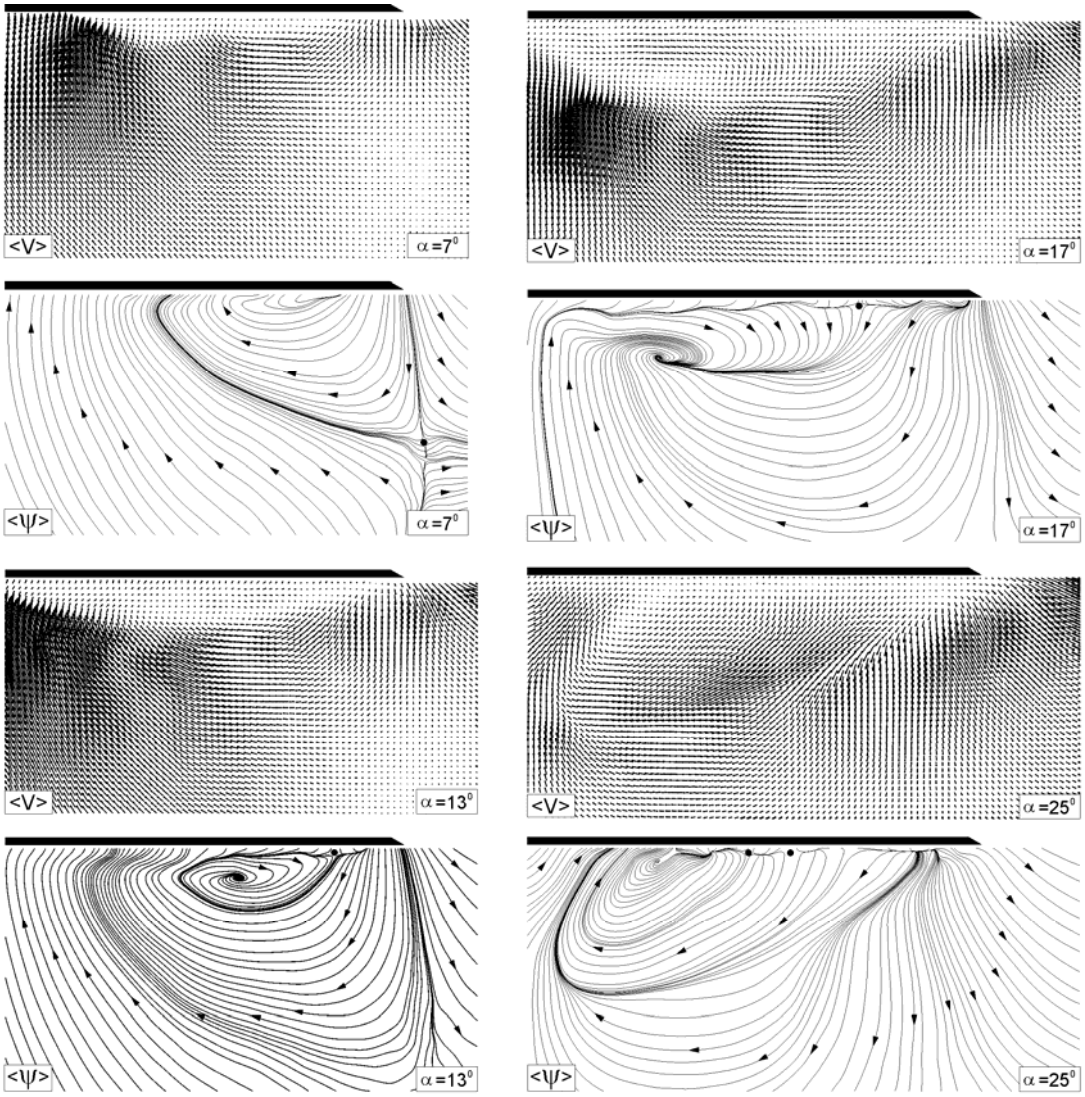


Figure 4.1.3 Patterns of averaged velocity $< V >$ and streamline $< \Psi >$ topology at four values of angle-of-attack α = 7°, 13°, 17° and 25°. Laser sheet is located at *x/C* = 0.8. Spanwise extent of wing corresponds to 0.82 *S* at α = 7° and 13° and 0.94 S at α = 17° and 25°, in which *S* is the semi-span of the delta wing at the location of the laser sheet, *x/C* = 0.8.

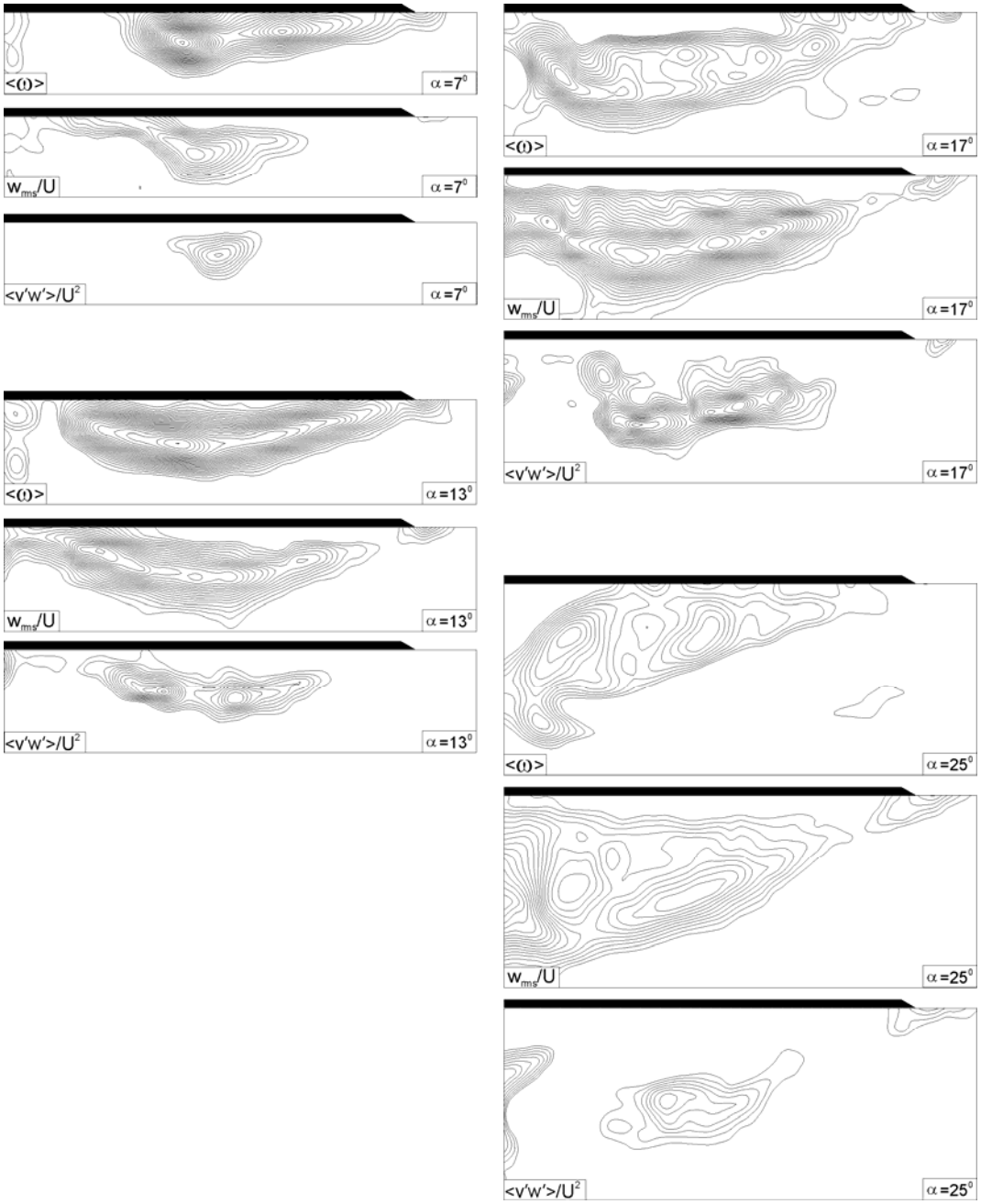


Figure 4.1.4. Patterns of averaged vorticity $<\omega>$, contours of constant vertical (transverse) velocity fluctuation w_{rms}/U and Reynolds stress correlation $<v'w'>/U^2$. Angles-of-attack are α = 7°, 13°, 17° and 25°. Laser sheet is located at x/C = 0.8. For contours of averaged vorticity, minimum and incremental values are $[<\omega>]_{min}$ = –0.3 sec^{-1} and $\Delta[<\omega>]$ = –0.15 sec^{-1}. For contours of constant velocity fluctuation, are $[w_{rms}/U]_{min}$ = 0.025 and $\Delta[w_{rms}/U]$ = 0.005. For contours of constant Reynolds stress correlation, $[<v'w'>/U^2]_{min}$ = –0.0004 and $\Delta[<v'w'>/U^2]$ = –0.0002. Spanwise extent of wing corresponds to 1.0 *S*, in which *S* is the semi-span of the delta wing at the location of the laser sheet *x/C* = 0.8.

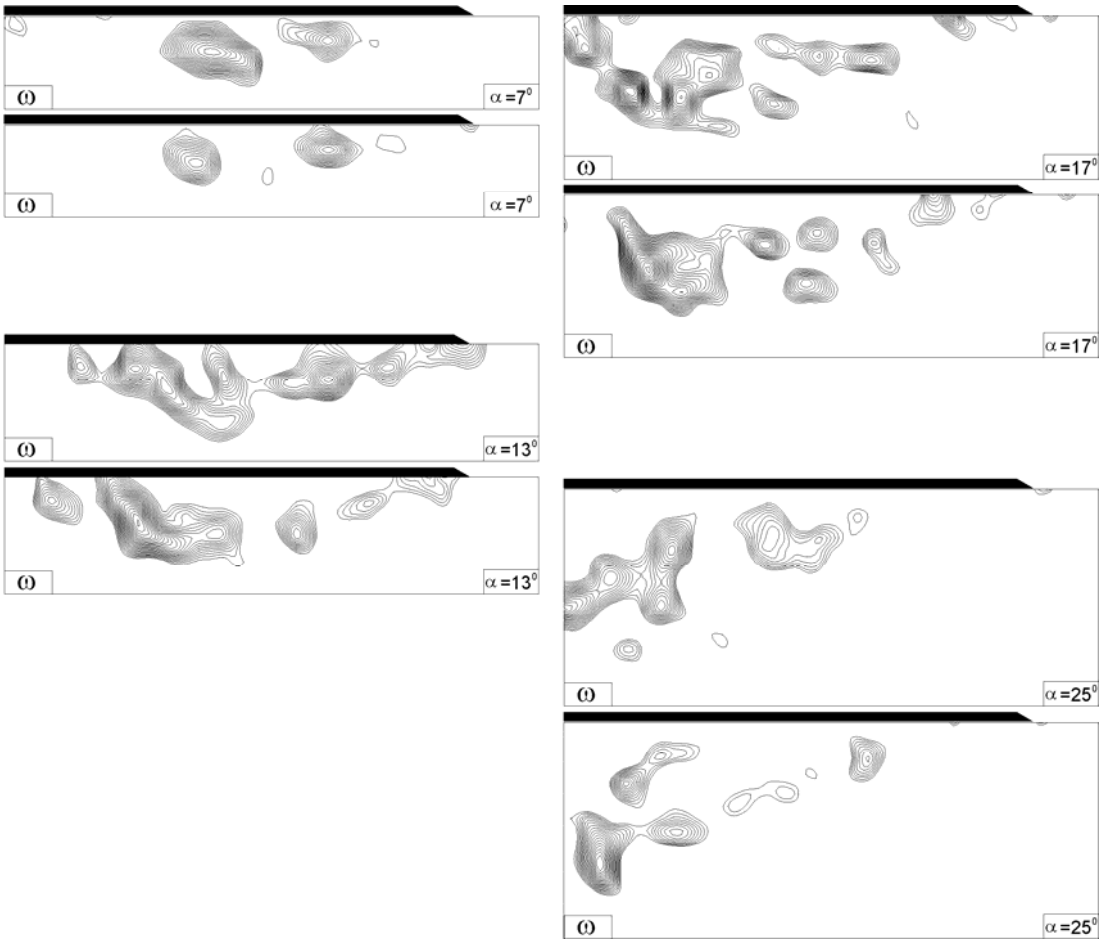


Figure 4.1.5. Patterns of instantaneous vorticity ω at two randomly selected instants from a cinema sequence. Angles-of-attack are α = 7°, 13°, 17° and 25°. Minimum and incremental values are $\omega_{min} = -1.5$ sec^{-1} and $\Delta\omega = -0.25$ sec^{-1}. Spanwise extent of wing corresponds to 1.0 S, in which S is the semi-span of the delta wing at the location of the laser sheet x/C = 0.8.

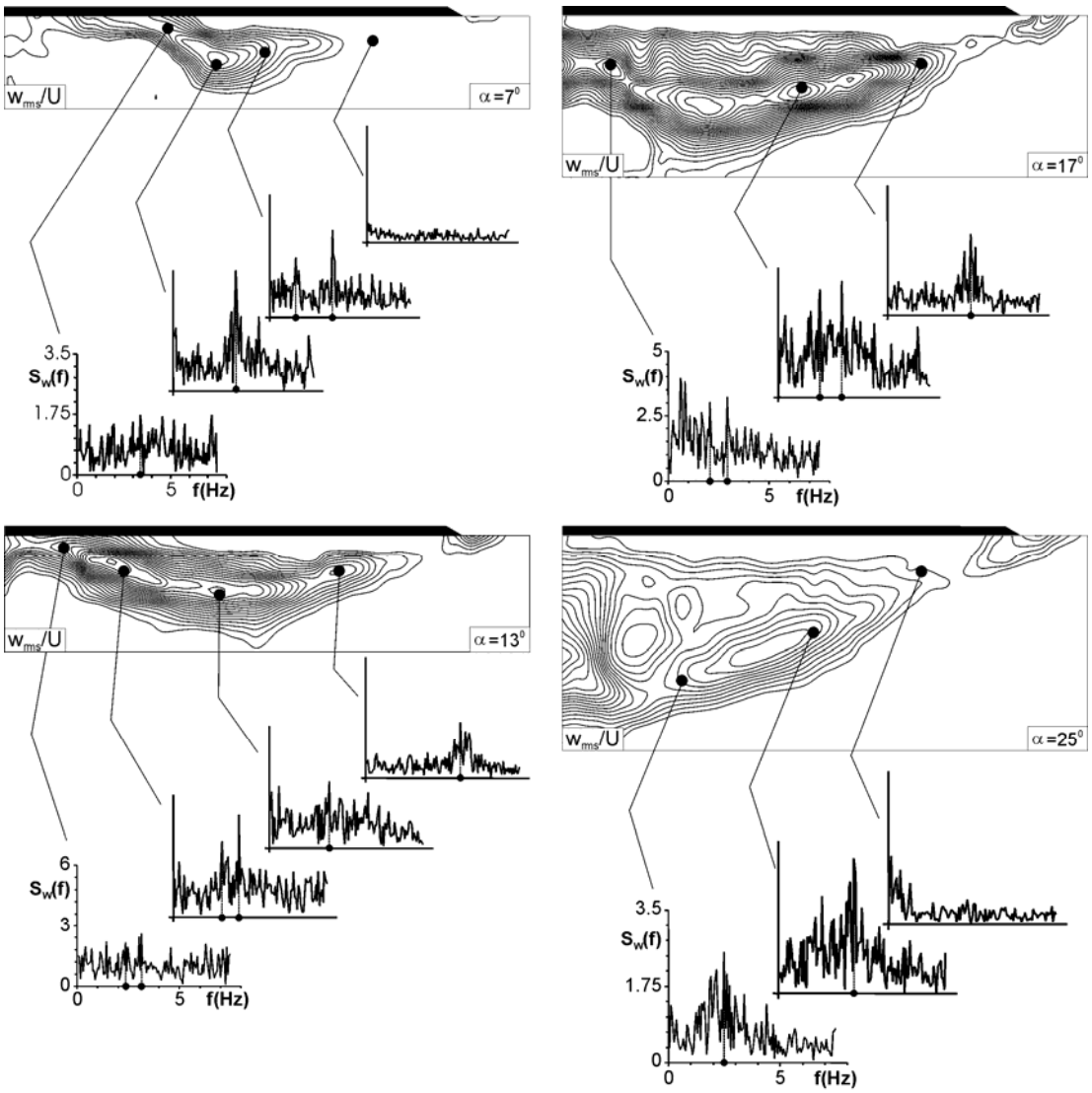


Figure 4.1.6. Spectra S_w of velocity fluctuation at selected locations in separated shear layer. Each spectrum is referenced to the indicated location in the pattern of constant contours of w_{rms}/U. Parameters for these contour levels are given in Figure 4.1.4. Spanwise extent of wing corresponds to 1.0 S, in which S is the semi-span of the delta wing at the location of the laser sheet, $x/C = 0.8$

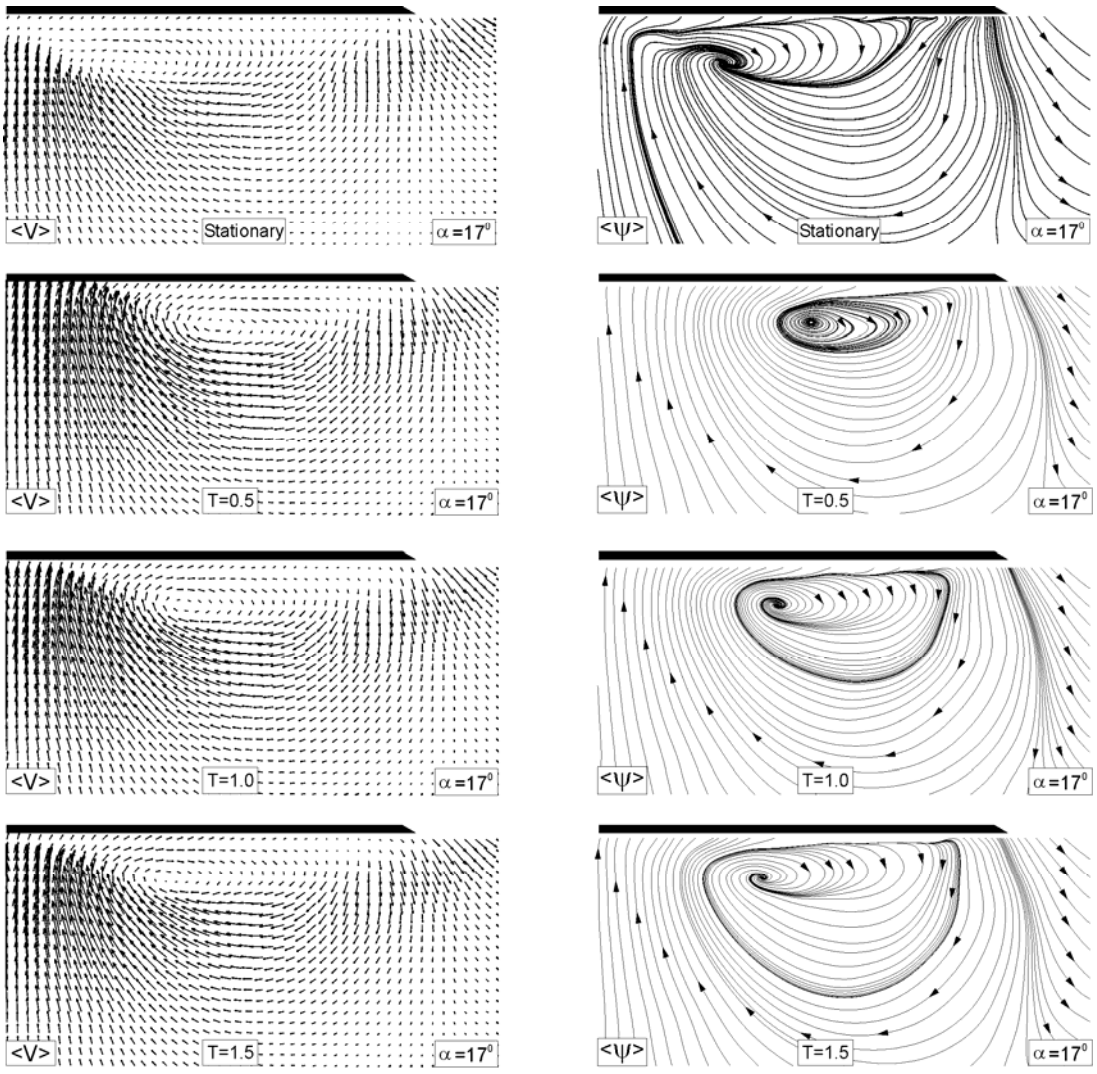


Figure 4.1.7. Effect of small perturbations of wing on time-averaged patterns of velocity $< V >$ and streamlines $< \Psi >$, relative to the case of he stationary wing. Perturbation amplitude is $\alpha_o = 1°$ and mean angle-of-attack is $\overline{\alpha} = 17°$. Perturbation is applied according to $\alpha(t) = \overline{\alpha} + \alpha_o \sin(2\pi t/T)$. Values of perturbation period T are $T = 0.5$, 1.0 and 1.5 sec. Spanwise extent of wing corresponds to 1.0 S, in which S is the semi-span of the delta wing at the location of the laser sheet, $x/C = 0.8$.

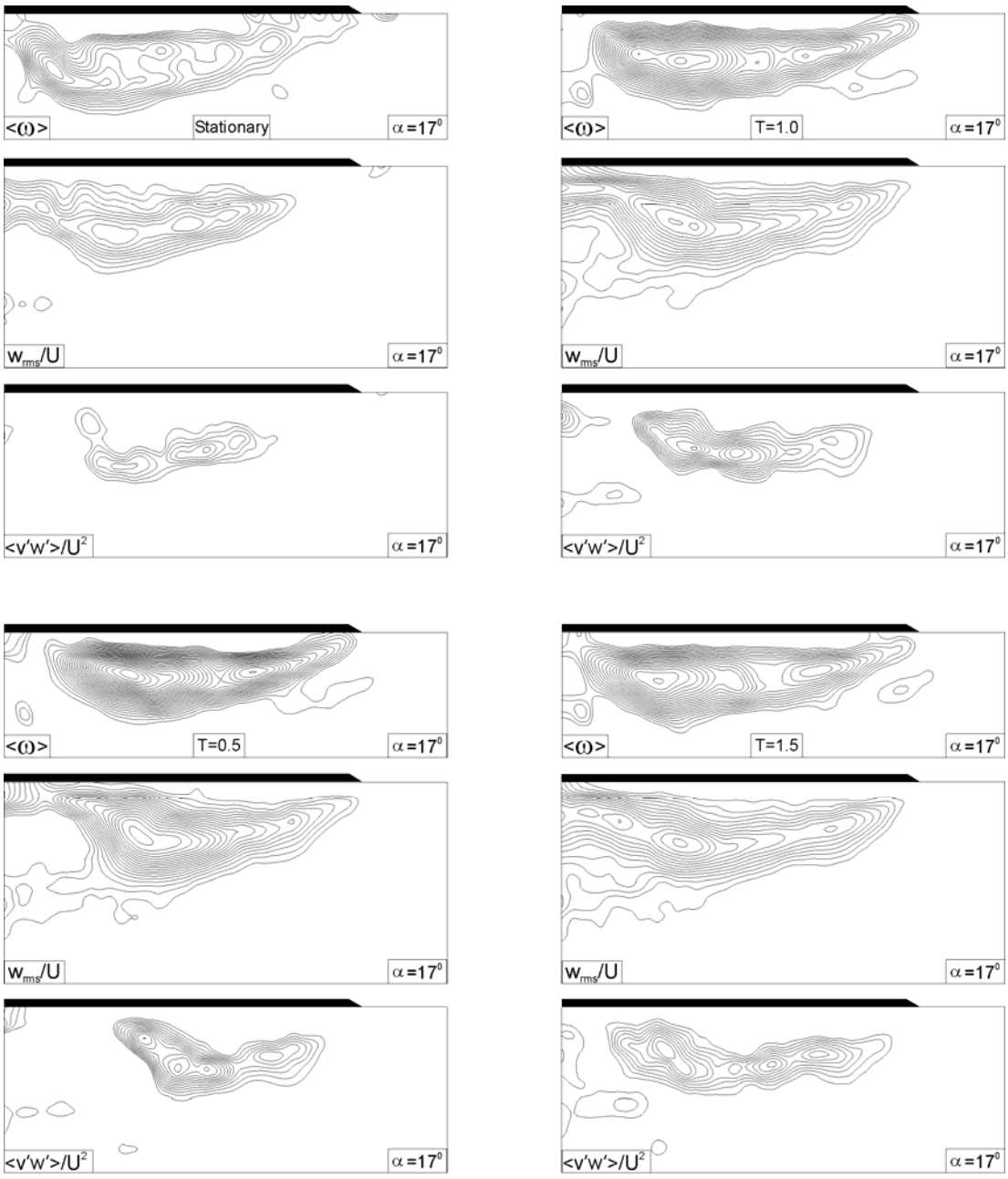


Figure 4.1.8. Consequence of small-amplitude perturbation on patterns of averaged vorticity $< \omega >$, root-mean-square of vertical (transverse) velocity fluctuation w_{rms}/U and Reynolds stress correlation $< v'w' > / U^2$. For patterns of vorticity, $< \omega >_{min}$ = –0.4 sec^{-1} and $\Delta[< \omega >]$ = –0.2 sec^{-1}. For contours of constant w_{rms}/U, $[w_{rms}/U]_{min}$ = 0.04 and $\Delta[w_{rms}/U]$ = 0.01. For contours of constant Reynolds stress correlation, $[< v'w' > / U^2]_{min}$ = –0.001 and $\Delta[< v'w' > / U^2]$ = –0.0005. Spanwise extent of wing corresponds to 1.0 *S*, in which *S* is the semi-span of the delta wing at the location of the laser sheet x/C = 0.8.

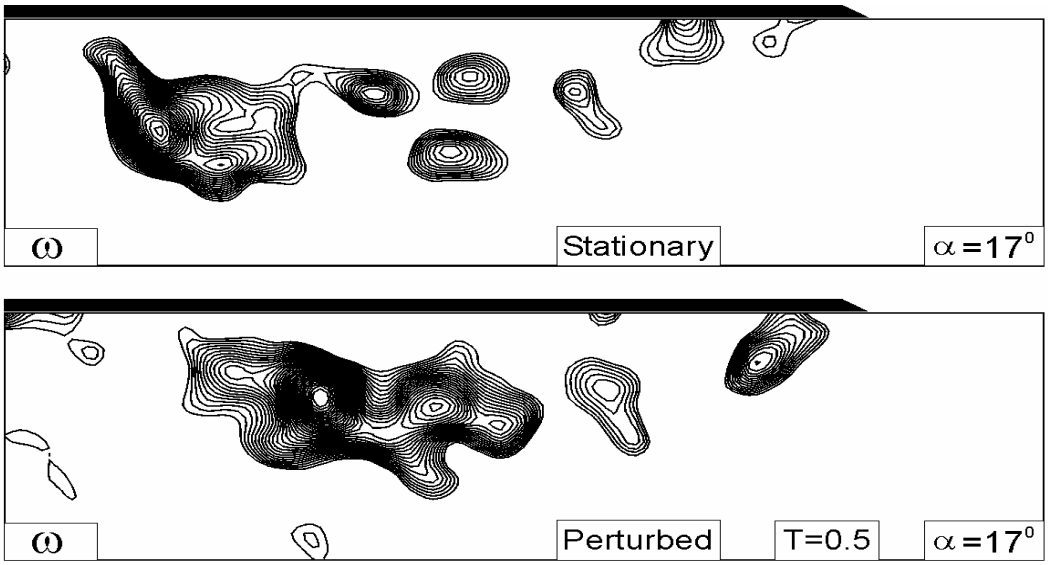


Figure 4.1.9. Comparison of representative patterns of instantaneous vorticity ω for the stationary wing and the wing subjected to small amplitude perturbations according to $\alpha(t) = \overline{\alpha}$ sine (ωt) in which $\overline{\alpha}$ 17°, $\alpha_o = 1°$ and $\omega = 2\pi t/T$. Minimum and incremental values of vorticity are $\omega_{min} = -1.5$ sec^{-1} and $\Delta\omega = -0.25$ sec^{-1}. Spanwise extent of wing corresponds to 1.0 S, in which S is the semi-span of the delta wing at the location of the laser sheet $x/C = 0.8$.

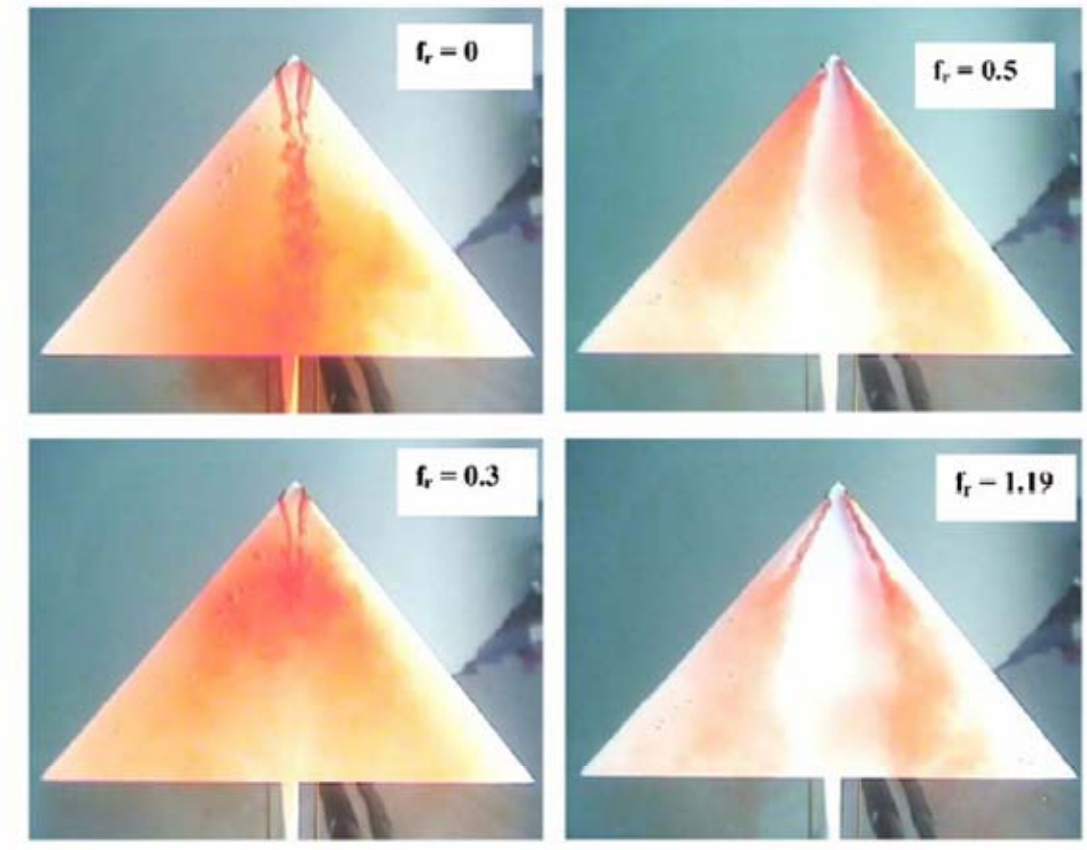


Figure 4.1.10. Flow visualization for a stationary and small amplitude ($\Delta\alpha = 1^o$) pitching wing for various reduced frequencies fC/U, $\alpha = 25^o$, $\Lambda=50^o$ (Gursul et al. (2005)).

4.2. Flow Structure on Diamond and Lambda Planforms: Trailing Edge-Region

4.2.1. Dye Visualization of Flow Patterns

Representative patterns of the flow, visualized by dye injection, are shown in Figure 4.2.1. At the lowest angle of attack angle-of-attack α = 7°, the dye was injected from two localized ports located at the apex of the wing. These ports were positioned to identify the locus of the vortex with the largest circulation formed from the leading-edge. Substantial distortions of the dye marker are evident well upstream of the trailing-edge of each wing; in an approximate sense, this distortion sets in at about $x/C' = 1.0$, corresponding to the coordinates given in Figure 3.2.6. These distortions, or undulations, are highly nonstationary, and are similar to the undulations prior to the onset of vortex breakdown calculated numerically by Gordnier and Visbal (2003) on a delta wing of low sweep angle.

At the higher angle of attack $\alpha = 13^o$, the dye was injected along the windward side of the leading-edge. The central portion of each wing is unmarked by dye, as it is continuously swept away by the streamwise velocity adjacent to the wing surface. On the other hand, exterior to this region, the dye is distributed over a large portion of the wing surface.

At higher angles of attack $\alpha = 17^o$ and 25^o considered in this investigation, the dye flooded the entire surface of the wing, and therefore these images are not shown.

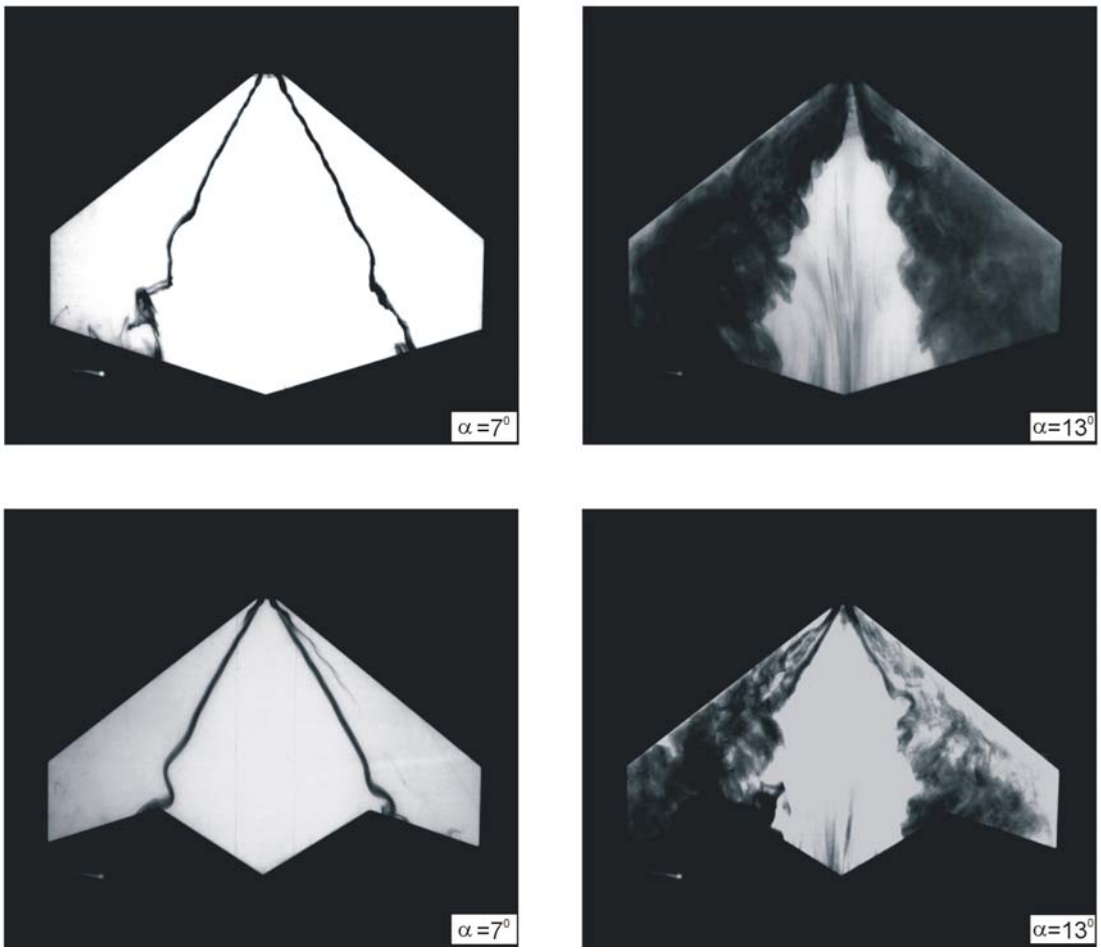


Figure 4.2.1. Dye visualization at angles-of-attack $\alpha = 7°$ and 13°. At $\alpha = 7°$, dye is injected from two localized ports at the apex of the wing, while at $\alpha = 13°$, it is injected along the leading-edge on the windward side.

4.2.2. Patterns of Averaged Velocity and Streamline Topology

Velocity patterns. Figure 4.2.2 shows patterns of averaged velocity <V> at angles-of-attack α = 7°, 13°, 17° and 25°. The patterns for the diamond and lambda planforms are directly compared at each angle-of-attack. At α = 7°, a common feature of the flow structure on both planforms is existence of a well-defined, small-scale swirl pattern at the leading-edge. Furthermore, both wings exhibit relatively narrow, elongated patterns of velocity vectors, with a recirculation flow towards the leading-edge of the wing. For the case of the lambda planform, the pattern is significantly distorted, apparently due to the gap occurring in the wing segment.

At α = 13°, the intense, small-scale swirl pattern located at the leading-edge, which was predominant at α = 7°, no longer exists. For each wing, well-defined swirl patterns are evident, however, at the interface between: (i) the recirculating flow that returns to the leading-edge region; and (ii) the flow exterior to this region. Furthermore, it is evident that the scale of the recirculation zone is smaller for the lambda planform.

At α = 17°, small-scale swirl patterns are again evident at the interface between the elongated recirculation zone and the exterior flow. The predominant pattern for the lambda planform is closer to the leading-edge than that for the diamond planform. This relative position of the swirl pattern is also evident at α = 13°.

Finally, for the angle-of-attack α = 25°, a well-defined, elongated swirl pattern no longer exists. Rather, flow is away from the wing surface towards the interface with the exterior flow. The overall spatial extent of this grossly separated flow pattern is approximately the same for both the diamond and lambda planforms.

Streamline Topology. Corresponding patterns of streamline topology, based on the averaged velocity patterns of Figure 4.2.2, are shown in Figure 4.2.3. At α = 7º, for the diamond planform, the streamlines form a small-scale limit cycle immediately adjacent to the leading-edge, while for the lambda planform, a localized

swirl pattern occurs in this region. It is evident that the focus (apparent center) of both streamline patterns is located very close to the leading-edge.

Furthermore, at α = 7º, a saddle point, i.e., the locus of an apparent intersection of streamlines, is located outboard of the leading-edge of the lambda planform; no such saddle occurs for the diamond planform. These differences indicate that the trailing-edge configuration of the planform has a global influence on the streamline topology. A common feature of the streamline topology of both planforms, however, is the flow adjacent to the surface of the wing towards the leading-edge; this return flow occurs over a relatively small width, in accord with the location of the interface of the corresponding patterns of averaged velocity $< V >$ shown at $\alpha = 7°$ in Figure 4.2.2. Just inboard of the leading-edge, this return flow merges with the small-scale swirl pattern at the leading-edge to form a system of convergent streamlines known as a bifurcation line; it has not been observed previously in the cross-sectional topology of wings of either large or small sweep angle.

At $\alpha = 13°$, foci are no longer evident at the leading-edge of either planform, and the streamline topology reverts to a more classical form, which involves a single-large-scale swirl inboard of the leading-edge. For the lambda planform, the focus (apparent center) of this pattern is located closer to both the leading-edge and the surface of the wing. Moreover, the saddle point evident at $\alpha = 7°$ in the outboard region still persists at this angle-of-attack, although it is located further from the surface of the wing.

At $\alpha = 17°$, the overall characteristics of the patterns at $\alpha = 13°$ are generally retained. On the other hand, at $\alpha = 25°$, the streamline patterns are indicative of a highly separated region adjacent to the surface of the wing, and it is not possible to identify a single, well-defined, large-scale swirl pattern.

The patterns of the averaged velocity $< V >$ and streamline topology $< \Psi >$ shown in Figure 4.2.2 and Figure 4.2.3 are associated with distinctive patterns of averaged vorticity $< \omega >$ and velocity fluctuations w_{rms}/U, which are addressed in the next section.

4.2.3. Patterns of Averaged Vorticity and Fluctuating Velocity

The images of Figures 4.2.4a and 4b show a direct comparison of the averaged vorticity $< \omega >$ and root-mean-square velocity w_{rms}/U at angles-of-attack α = 7°, 13°, 17°, and 25°, for both the diamond and lambda planforms.

Consider the patterns of averaged vorticity $< \omega >$ at α = 7° in Figures 4.2.4a. Both planforms exhibit a cluster of concentrated vorticity at the leading-edge, which is associated with the localized swirl pattern of velocity shown at α = 7° in Figures 4.2.2, and the focus of the streamline topology at the leading-edge at α = 7º in Figures 4.2.3. Furthermore, the patterns of vorticity are relatively elongated and contain two identifiable cells, or local concentrations of vorticity, designated as *a* and *b*, in addition to the vorticity concentrations appearing at the leading-edge. These substructures are similar in form to those identified in the numerical simulation of Gordnier and Visbal (2003) on a simple delta wing of low sweep angle. The corresponding patterns of transverse velocity fluctuation w_{rms}/U are generally similar for both planforms. The peak values are $[w_{rms}/U]_{max}$ = 0.12 and 0.13 for the diamond and lambda planforms respectively.

At α = 13°, the region of highly-concentrated vorticity in the vicinity of the leading-edge becomes even more pronounced, relative to that at α = 7°, for both planforms. These concentrations at α = 13º are, however, displaced further from the edge than those at α = 7º. For this reason, they are not detectable in the corresponding streamline topology of Figures 4.2.3. Furthermore, the vorticity layers appear as relatively elongated, and have a substantially larger spanwise extent and width than at α = 7°. Within these large-scale elongated layers, a number of smaller-scale concentrations of vorticity are evident at both α = 7º and 13º. They are more clearly defined, however, for the lambda planform, and for purposes of simplicity in describing their existence, individual structures are designated for this planform at α = 13º and at α = 17°. The predominant, distinctive concentrations at α = 13º are indicated as *a*, *b*, and *c*. The corresponding patterns of root-mean-square velocity w_{rms}/U occupy a relatively large spatial extent, relative to the vorticity layer.

Generally speaking, the maximum values of w_{rms}/U approximately correspond to the outer edge of the averaged patterns of vorticity $< \omega >$. The peak value of velocity fluctuation is significantly high, i.e., $[w_{rms}/U]_{max} = 0.24$ and 0.20 respectively for the diamond and lambda planforms.

Patterns corresponding to higher angles-of-attack $\alpha = 17°$ and 25° are shown in Figures 4.2.4b. At $\alpha = 17°$, the patterns of averaged vorticity $< \omega >$ exhibit a generally similar, large-scale, elongated form as at $\alpha = 13°$. The pronounced concentration of vorticity adjacent to the leading-edge persists for both planforms. Furthermore, identifiable concentrations of vorticity are evident in the large-scale, elongated layer. The most prominent are designated as *a*, *b*, *c* and *d* on the lambda planform. The respective patterns of velocity fluctuation w_{rms}/U occupy a still larger spatial extent than at $\alpha = 13°$. The peak values are generally at the same spatial position as at the outer region of each of the large-scale patterns of averaged vorticity $< \omega >$. The peak values of the velocity fluctuation are $[w_{rms}/U]_{max} = 0.24$ and 0.22 respectively for the diamond and lambda planforms.

For the highest angle-of-attack $\alpha = 25°$, the patterns of averaged vorticity $< \omega >$ take on a fundamentally different form. They are displaced a substantial distance from the surface of the wing and, moreover, contain identifiable concentrations of smaller-scale vorticity, specified as *a*, *b*, *c* and *d*. The locations of these smaller-scale concentrations are generally coincident with the peak values of velocity fluctuation w_{rms}/U. The peak values are $[w_{rms}/U] = 0.24$ and 0.2 respectively for the diamond and lambda planforms. It is apparent that the layers of vorticity shown in Figures 4.2.4b are formed at the interface between the highly-separated region and the exterior flow indicated in the patterns of averaged velocity $< V >$ at $\alpha = 25°$ in Figure 4.2.2. That is, this layer of relatively high vorticity exists adjacent to a large-scale region of separated flow.

4.2.4. Patterns of Averaged Vorticity and Streamline Topology: A Comparison

Certain of the patterns of averaged streamline topology shown in Figures 4.2.3 suggests existence of a single, large-scale leading-edge vortex, especially the patterns corresponding to the diamond planform at α = 13° and 17°. This type of pattern, however, must be interpreted in conjunction with the corresponding pattern of averaged vorticity $< \omega >$, as shown in Figures 4.2.4a and 4b. The comparisons of Figures 4.2.5 involve superposition of patterns of averaged vorticity $< \omega >$ and averaged streamline topology $< \Psi >$ at α = 17° for the diamond and lambda planforms. As emphasized previously, the vorticity layer exhibits a narrow, elongated form, in contrast to the classical, nearly circular pattern of vorticity which occurs on highly swept wings at sufficiently large angle-of-attack. For the diamond planform, the focus (apparent center) of the streamline pattern lies approximately midway along the elongated layer of vorticity. For the lambda planform, however, the focus is actually closer to the leading-edge of the wing. In an overall sense, these streamlines pattern do not indicate the presence of the well-defined, smaller-scale concentrations of vorticity.

The aforementioned coexistence of an elongated vorticity layer and a single spiral pattern of streamlines (with a single focus) appears to be an inherent feature of rapidly distorting flows separating from a solid boundary. For the case of vortex formation in the very near-wake of a cylinder, Akilli and Rockwell (2002) observe conceptually similar patterns of streamline topology and vorticity layers. In this region, the boundary layer from the cylinder separates to form the elongated free shear layer.

4.2.5. Patterns of Instantaneous Vorticity

Patterns of instantaneous vorticity are shown relative to instantaneous velocity vectors in Figure 4.2.6. In the left column, these patterns are compared at an angle-of-attack α = 7º, along with the corresponding pattern of the averaged velocity <V>, while in the right column, they are compared for α = 25º. Generally speaking,

the identifiable clusters of vorticity are associated with well-defined swirls of patterns of velocity vectors.

In order to indicate the degree of variability of the instantaneous patterns of vorticity, Figures 4.2.7a shows two random images at each angle-of-attack α, and for both the diamond and lambda planforms. Angles-of-attack α = 13º and 17º are represented in Figures 4.2.7a, while α = 17º and 25º are shown in Figures 4.2.7b. All patterns exhibit, from one instant to the next, significant variability in the precise location and level of the vorticity concentrations. Nevertheless, a quasi-ordered structure is apparent in each of the images and, furthermore, it is possible to discern, in an approximate sense, the spacing between identifiable concentrations of vorticity. For each of the sets of instantaneous images, at each value of angle-of-attack α and each planform, the spacing between concentrations is, in most cases, roughly commensurate with the spacing between the time-averaged patterns of substructures *a*, *b*, *c* and *d* shown in Figures 4.2.4a and 4b. During the averaging process that yields the patterns of Figures 4.2.4a and 4b, the instantaneous patterns of Figures 4.2.7a and 7b are, in effect, smeared due to the variation in spatial position of the patterns of vorticity concentrations over the entire time sequence of instantaneous images. As a result, the peak values of vorticity and the patterns of Figures 4.2.4a and 4b are typically much lower than the peak values in the corresponding instantaneous images.

4.2.6. Spectra of Fluctuating Velocity

The organized patterns of instantaneous vorticity shown in Figures 4.2.7a and 7b are associated with definable spectral components of the velocity fluctuation w. These spectra $S_w(f)$ are shown in Figure 4.2.8 for α = 7° and 25°. Each spectrum is referenced to a specified location in the corresponding pattern of constant contours of root-mean-square velocity fluctuation w_{rms}/U. At α = 7°, for the diamond planform, a well-defined spectral component emerges just inboard of the leading-edge; its frequency is f = 0.49 Hz. Further along the separated layer, a higher frequency component occurs; its value is f = 1.49 Hz and it coexists with the aforementioned

component at f = 0.95 Hz. For the lambda wing, organized spectral components are also detectable. They have values in the range f = 0.77 to 1.37 Hz.

As the vorticity layer tends to reattach to the surface of both lambda and diamond planforms, the degree of organization, as well as the peak amplitude of the spectral component, both decrease. In fact, for the diamond planform, the organized component is nearly entirely attenuated.

For the highest angle-of-attack $\alpha = 25°$ (diamond planform), an organized spectral component is clearly detectable at a significant distance from the leading-edge. It has a value f = 0.95 Hz. This spectral component persists along the separated layer, and at the furthest location from the leading-edge, components at f = 0.71 and 0.95 Hz are evident. For the lambda planform, at the location closest to the leading-edge, the spectral component is f = 1.43 Hz, and at locations further along the layer, a single, well-defined component no longer occurs. Rather, the general peak is relatively broadband. The center frequencies of these rather broad distributions of peaks are indicated and have spectral components in the range f = 0.83 to 1.31 Hz.

For the diamond planform, the identifiable spectral peaks in Figure 4.2.8 are in the range $0.71 \leq f \leq 0.95$ Hz, which corresponds to $2.69 \leq fC/U \leq 3.60$. For the lambda planform, the identifiable spectral peaks are in the range $0.77 \leq f \leq 1.43$ Hz, which corresponds to $2.13 \leq fC/U \leq 3.97$. For the case of a simple delta wing, Yaniktepe and Rockwell (2004) found values of dimensionless frequency, based on spectral analysis, extending over the range of $0.51 \leq fC/U \leq 3.29$ and, for a simple delta wing of sweep angle $\Lambda = 50^{o}$, Gordnier and Visbal (2003) computed a band of frequencies in the surface pressure spectrum extending over the approximate range $1 \leq fC/U \leq 4.5$. Taken together, all of the foregoing results suggest that the organized unsteadiness associated with undulations or breakdown of the vortex core extend approximately over the range $0.5 \leq fC/U \leq 4.5$ for wings having relatively low sweep angle. Remarkably, this range of frequencies approximates frequencies associated with the helical mode of instability of vortex breakdown of wings having relatively

high sweep angle $1.0 \leq fC/U \leq 4$, as assessed by Menke et al. (1999) and earlier works cited therein.

Using the type of approach that lead to the spectra shown in Fig. 4.2.8, it was possible to employ the cinema sequence of PIV images, in order to undertake both autospectral and cross-spectral analysis, thereby yielding representations at a large number of points throughout the plane of the flow field. Figure 4.2.9 shows a representative set of contours at $\alpha = 7°$. Focuses on the predominant spectral component $f_o = 1$ Hz. At a large number of points over the plane of the flow field, contours of constant spectral peak $< S_w(f_o) >$ could be constructed. They are designated in the middle of the schematic in the plot of Figure 4.2.9, which also shows a representative pattern of instantaneous velocity, in order to provide a sense of the flow unsteadiness from the leading-edge. These contours show two sets of maxima, the predominant one closer to the leading-edge. Of particular interest for the unsteady surface loading is not only the amplitude of the fluctuating velocity field adjacent to the surface, but also its phase variation, as a function of distance from the leading-edge.

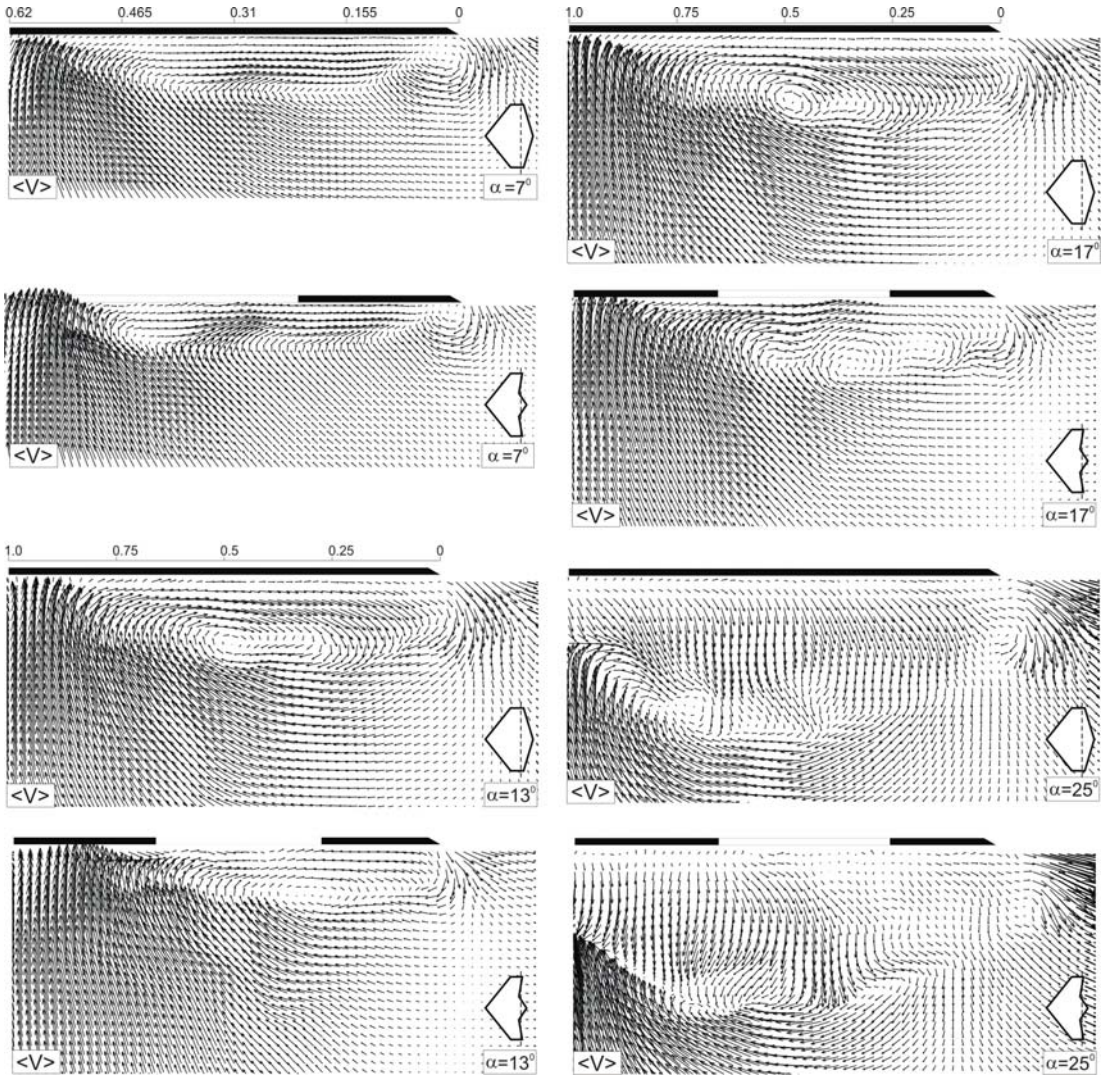


Figure 4.2.2. Patterns of time-averaged velocity $< V >$ at α = 7°, 13°, 17° and 25°. For both the diamond and lambda planforms, laser sheet is located at $x/C' = 1.4$, immediately downstream of abrupt change of sweep angle. Scale shown above planform cross-section is y/S, in which y/S = 1.0 corresponds to plane of symmetry of wing; S is the semi-span at $x/C' = 1.4$.

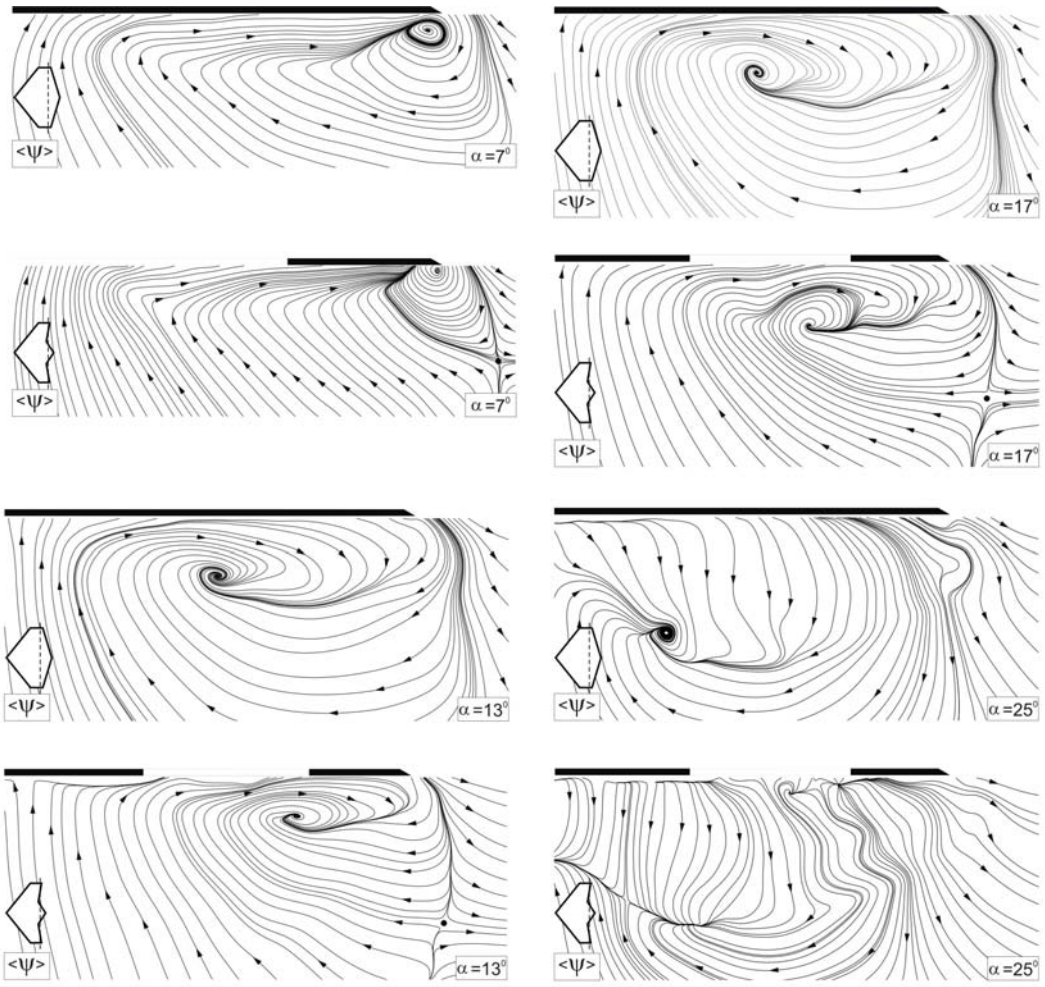


Figure 4.2.3. Patterns of time-averaged streamline $< \Psi >$ topology at angles-of-attack α = 7°, 13°, 17° and 25° for the diamond and lambda planforms. For both planforms, the laser sheet is located at $x / C' = 1.4$, immediately downstream of abrupt change of sweep angle. Spanwise extent of each planform cross-section is same as in Figure 4.2.2.

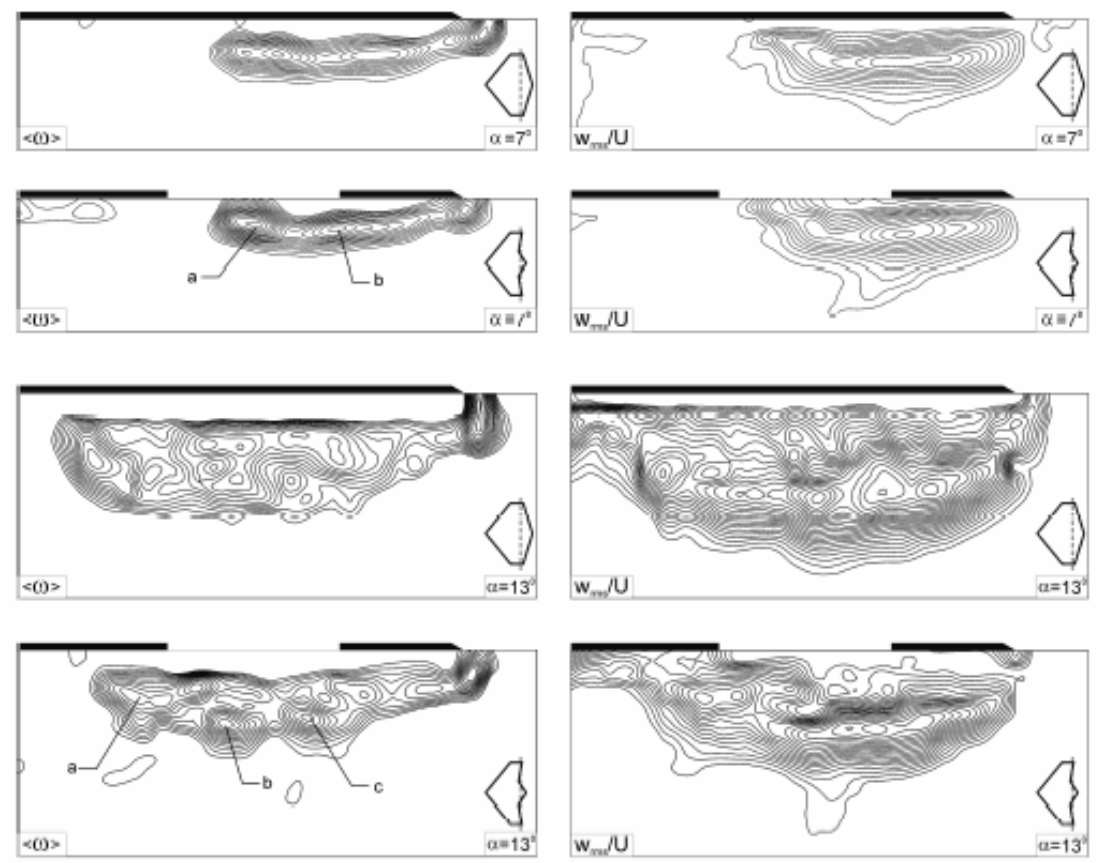


Figure 4.2.4a. Patterns of time-averaged vorticity $< \omega >$ and corresponding patterns of root-mean-square velocity fluctuation w_{rms}/U (normal to the wing). At angle-of-attack $\alpha = 7°$, minimum and incremental values of vorticity contours are $[< \omega >]_{min} = -0.2\ sec^{-1}$ and $\Delta[< \omega >] = -0.15\ sec^{-1}$. At $\alpha = 13°$, $[< \omega >]_{min} = -0.35\ sec^{-1}$ and $\Delta[< \omega >] = -0.15\ sec^{-1}$. For patterns of root-mean-square velocity, minimum and incremental values at $\alpha = 7°$ are $[w_{rms}/U]_{min} = 0.02$ and $\Delta[w_{rms}/U] = 0.01$. For $\alpha = 13°$, $[w_{rms}/U]_{min} = 0.04$ and $\Delta[w_{rms}/U] = 0.01$. For both the diamond and lambda planforms, laser sheet is located at $x/C' = 1.4$, immediately downstream of abrupt change of sweep angle. In each image, spanwise extent of planform cross-section corresponds to the semi-span S of the wing at $x/C' = 1.4$.

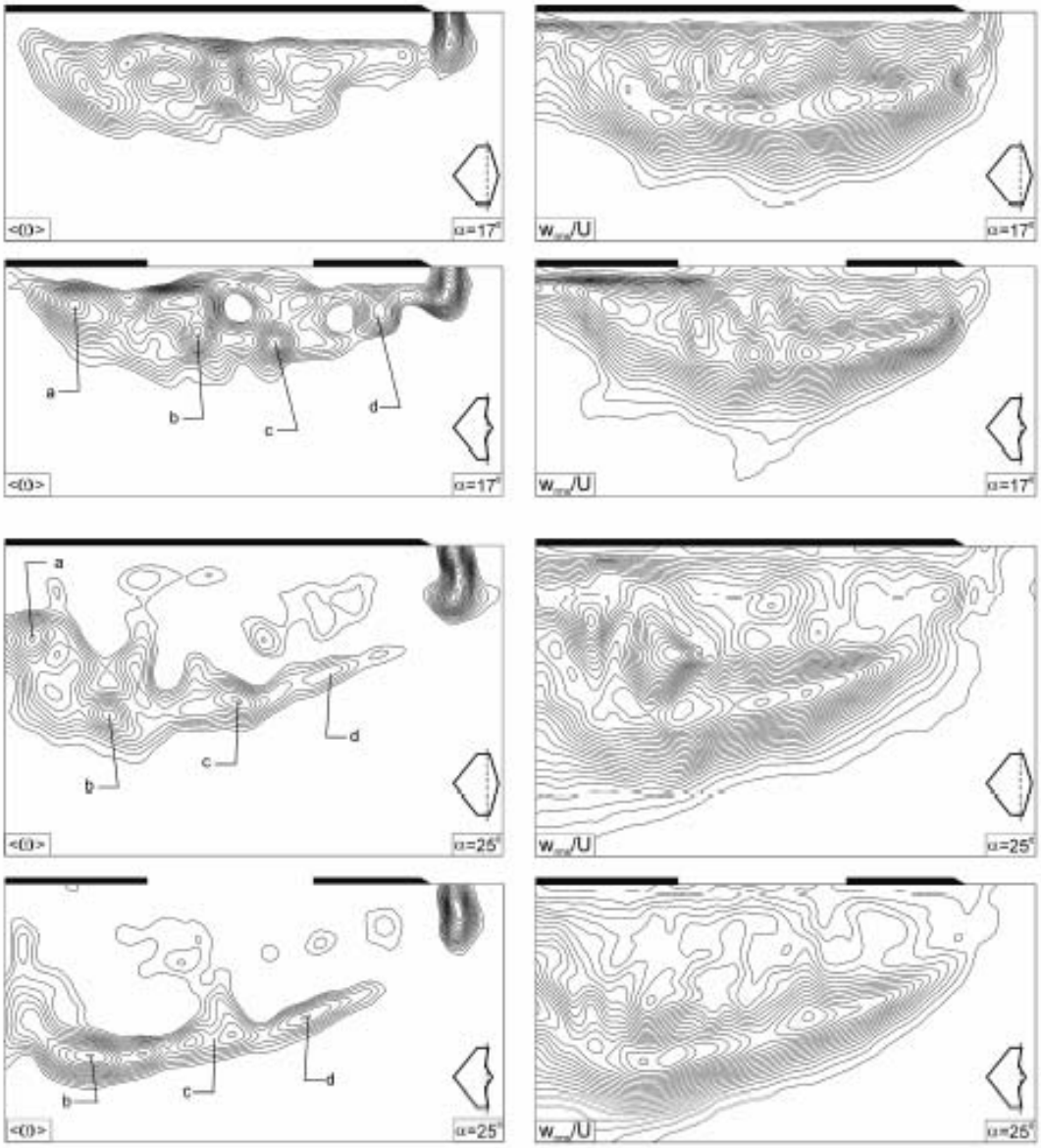


Figure 4.2.4b. Patterns of time-averaged vorticity $< \omega >$ and corresponding patterns of root-mean-square velocity fluctuation w_{rms}/U (normal to the wing). At angle-of-attack $\alpha = 17°$, minimum and incremental values of vorticity contours are $[< \omega >]_{min} = -0.35\ sec^{-1}$ and $\Delta[< \omega >] = -0.15\ sec^{-1}$. At $\alpha = 25°$, $[< \omega >]_{min} = -0.2\ sec^{-1}$ and $\Delta[< \omega >] = -0.15\ sec^{-1}$. For contours of root-mean-square vertical velocity, at $\alpha = 17°$, $[w_{rms}/U]_{min} = 0.03$ and $\Delta[w_{rms}/U] = 0.01$. For $\alpha = 25°$, $[w_{rms}/U]_{min} = 0.02$ and $\Delta[w_{rms}/U] = 0.01$. For both the diamond and lambda planforms, laser sheet is located at $x/C' = 1.4$, immediately downstream of abrupt change of sweep angle. In each image, spanwise extent of planform cross-section corresponds to the semi-span S of the wing at $x/C' = 1.4$.

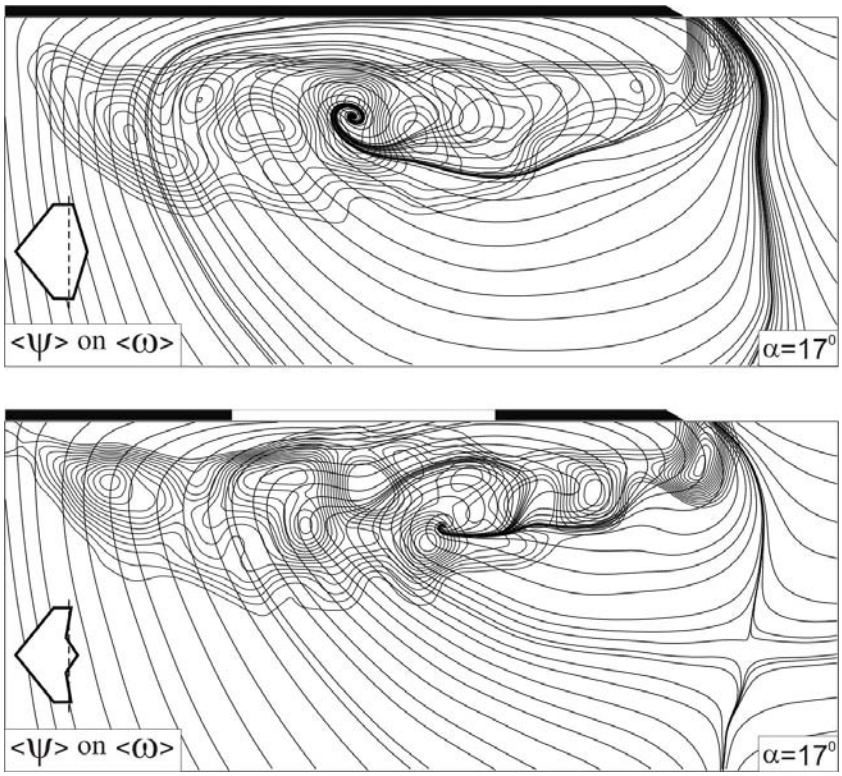


Figure 4.2.5. Superposition of patterns of averaged vorticity $< \omega >$ and streamline $< \Psi >$ topology at $\alpha = 17°$ for the diamond and lambda planforms. The laser sheet is located at $x / C' = 1.4$.

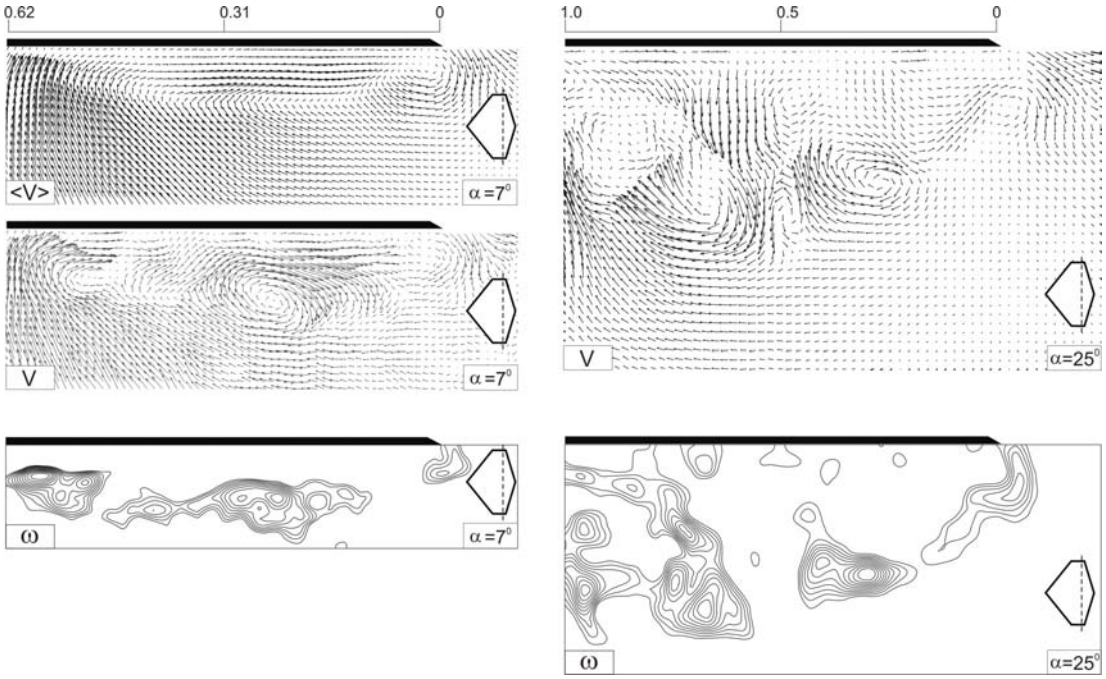


Figure 4.2.6. Comparison of patterns of instantaneous velocity V and vorticity ω at angles-of-attack α = 7° and 25° for the diamond planform. At α = 7°, minimum and incremental values of vorticity are $\omega_{min} = -1.5$ sec^{-1} and $\Delta\omega = -0.5$ sec^{-1}. At α = 25°, minimum and incremental values of vorticity are $\omega_{min} = -0.5$ sec^{-1} and $\Delta\omega = -0.5$ sec^{-1}. For both the diamond and lambda planforms, laser sheet is located at $x/C' = 1.4$, immediately downstream of abrupt change of sweep angle. Spanwise extent of each planform cross-section extends from y/S = 0 to 0.62 (α = 7º) and to 1.0 (α = 25º).

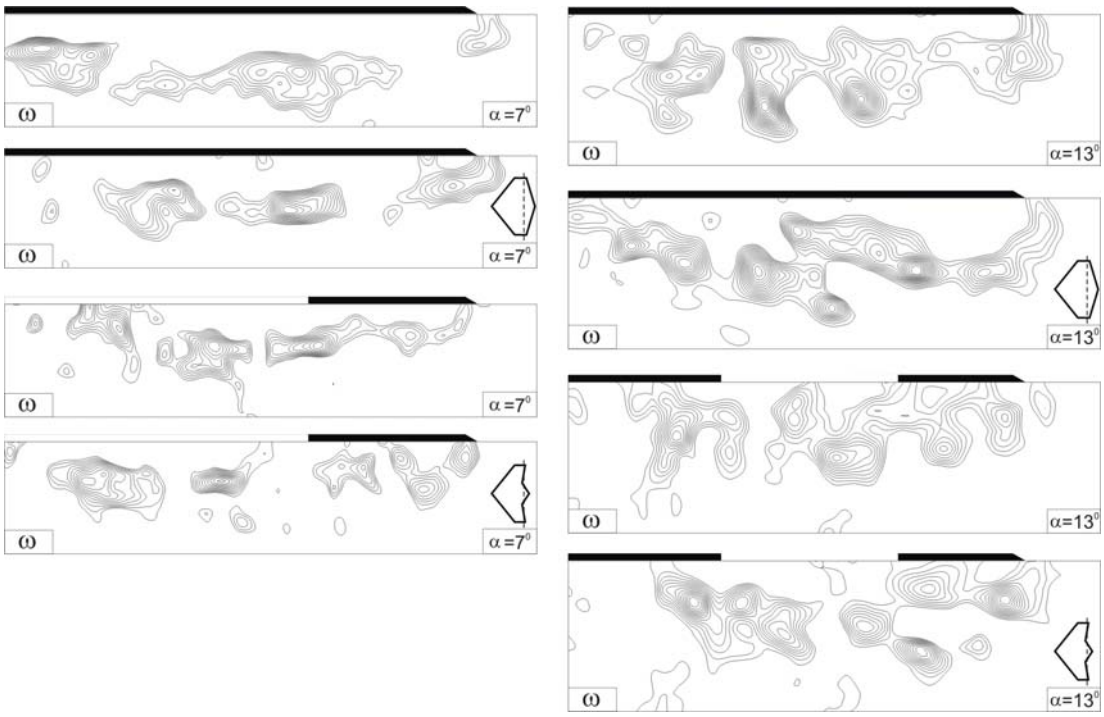


Figure 4.2.7a. Patterns of instantaneous vorticity ω at angles-of-attack α = 7° and 13° for the diamond and lambda planforms. At α = 7º, values of minimum and incremental levels of vorticity are $\omega_{min} = -1.5$ sec^{-1} and $\Delta\omega = -0.5$ sec^{-1}. At α = 13º, values of minimum and incremental levels of vorticity are $\omega_{min} = -0.5$ sec^{-1} and $\Delta\omega = -0.5$ sec^{-1}. For both the diamond and lambda planforms, laser sheet is located at $x / C' = 1.4$, immediately downstream of abrupt change of sweep angle. At α = 7º (diamond and lambda planforms), spanwise extent of planform cross-section extends from y/S = 0 (leading-edge) to y/S = 0.62. For all other images, it extends from y/S = 0 to y/S = 1.0, where S is the semi-span at $x / C' = 1.4$.

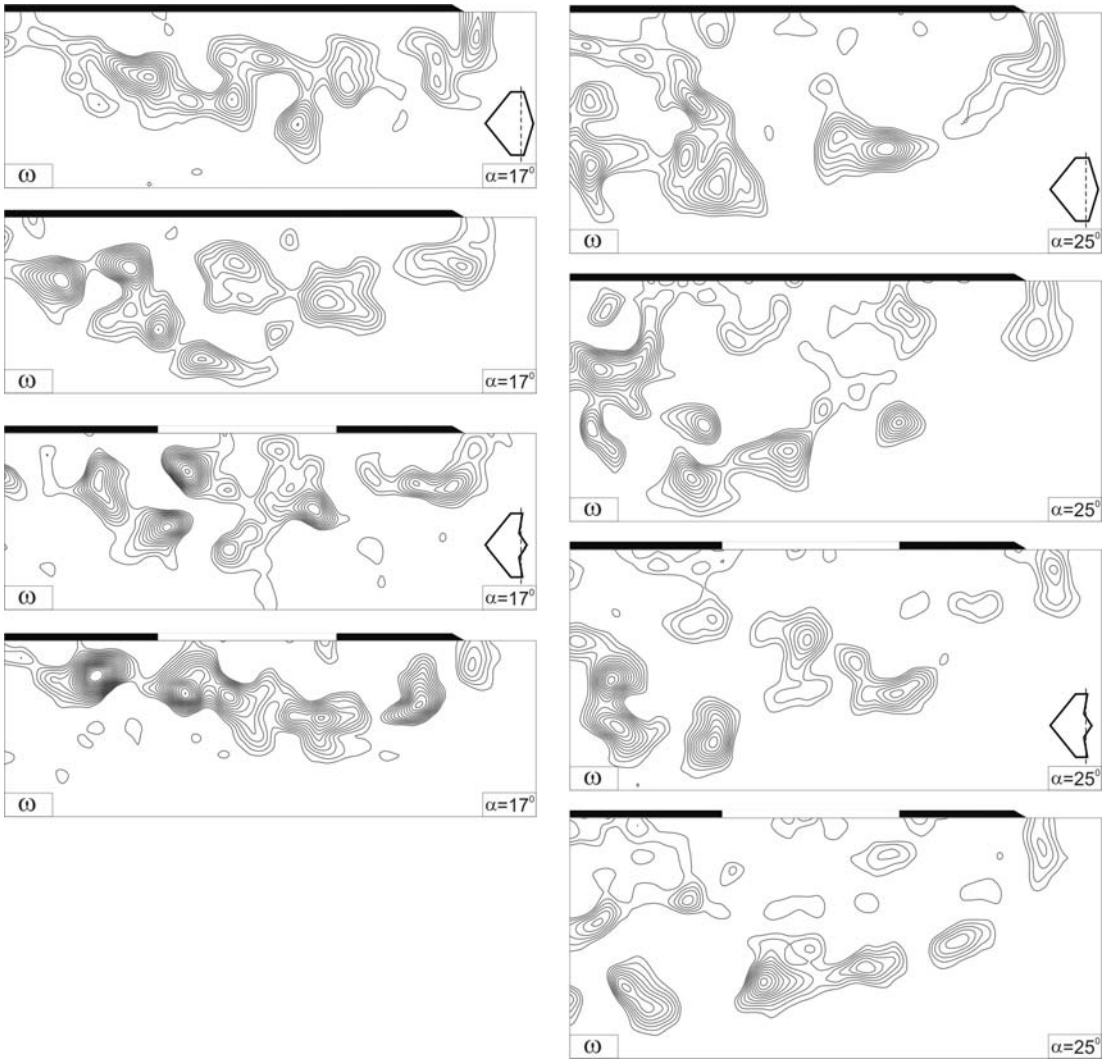


Figure 4.2.7b. Patterns of instantaneous vorticity ω at angles-of-attack $\alpha = 17°$ and 25° for the diamond and lambda planforms. Values of minimum and incremental levels of vorticity are $\omega_{min} = -0.5$ sec^{-1} and $\Delta\omega = -0.5$ sec^{-1}. For both the diamond and lambda planforms, laser sheet is located at $x / C' = 1.4$, immediately downstream of abrupt change of sweep angle.

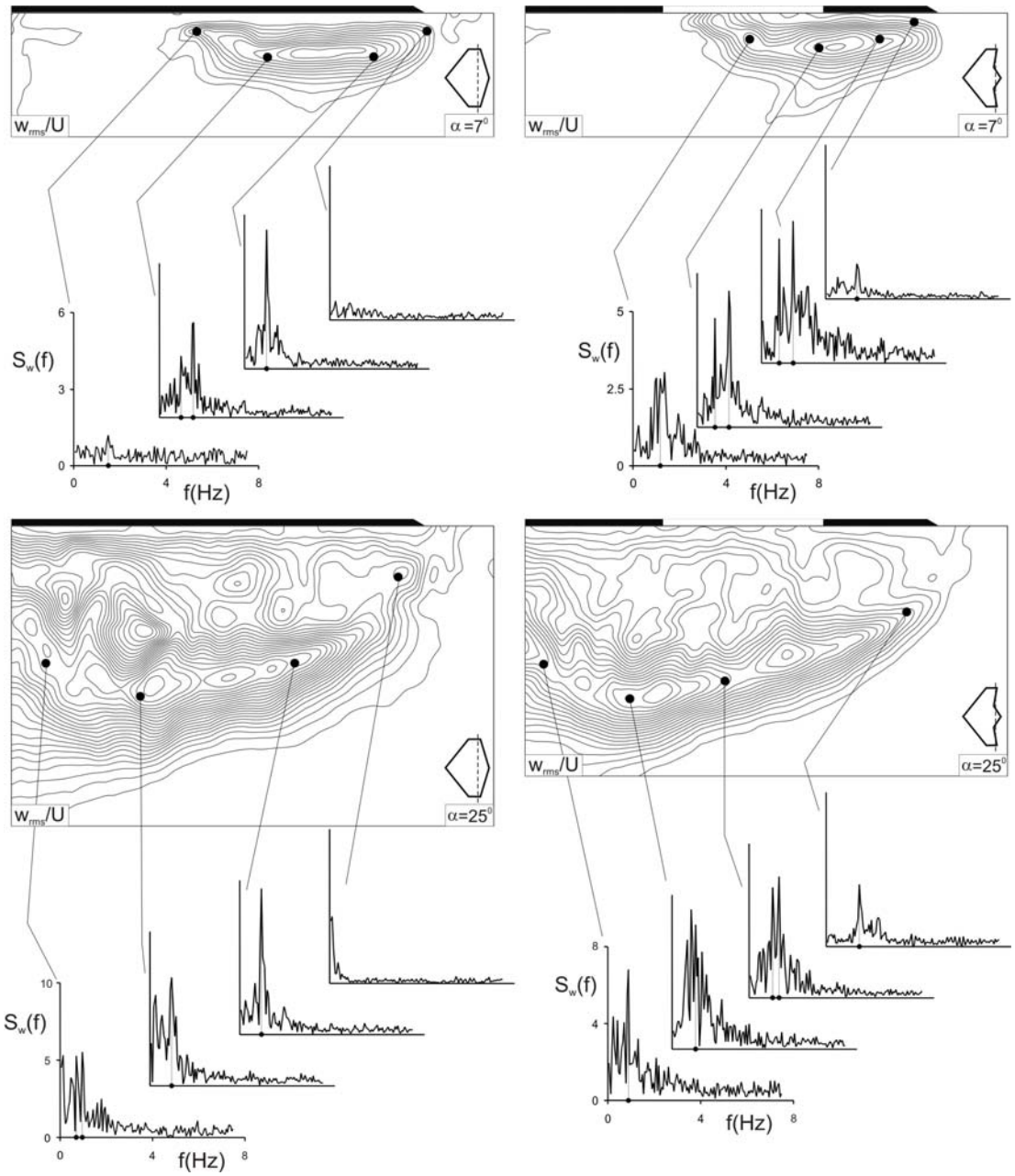


Figure 4.2.8. Spectra $S_w(f)$ of the vertical velocity fluctuation w at locations corresponding to maxima of the root-mean-square value of the transverse (vertical) velocity fluctuation w_{rms}/U at angles-of-attack α = 7° and 25° for the diamond and lambda planforms. The laser sheet is located at $x / C' = 1.4$.

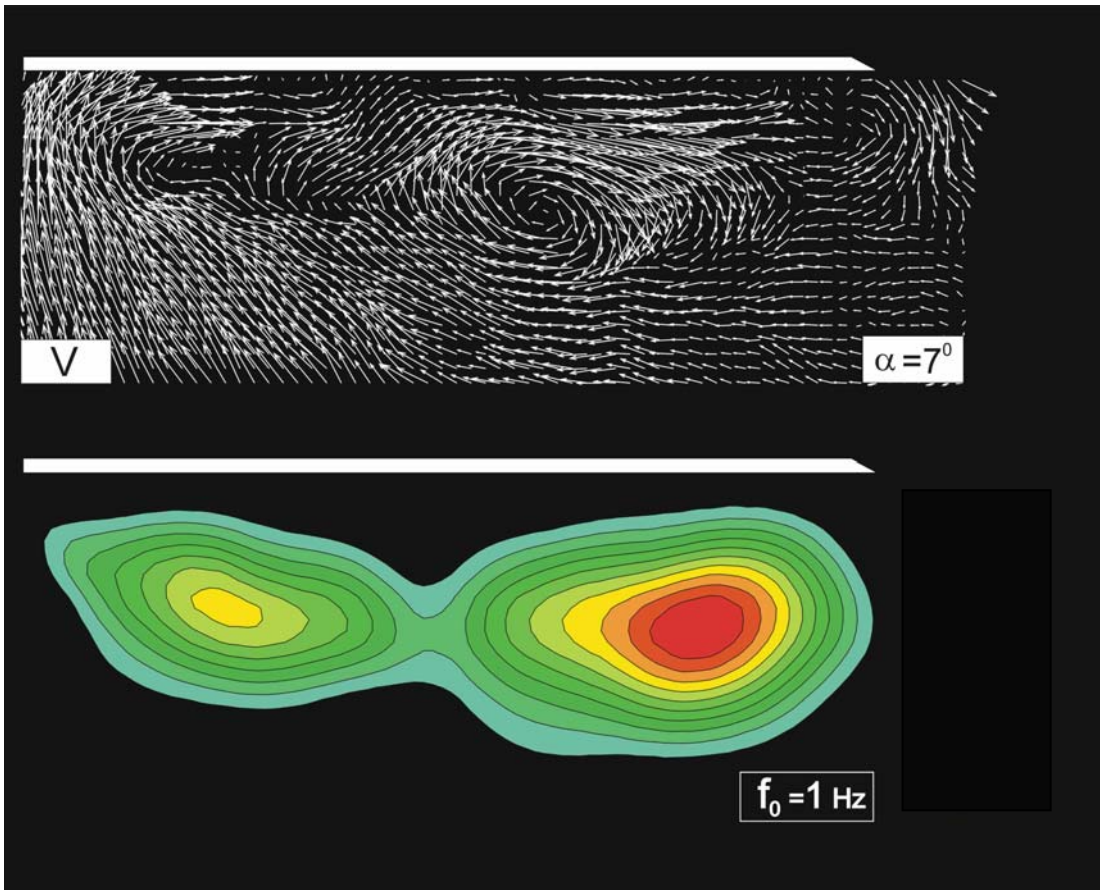


Figure 4.2.9. Global representations of peak spectral amplitude $\langle S_w(f_o) \rangle$ at $\alpha = 7°$. The laser sheet is located at $x / C' = 1.4$. for the diamond planforms.

4.3. The Effect of Reynolds Number on the Vortex Breakdown Location

Aircraft maneuverability is the key element in the successful missions accomplishment of a combat aircraft. Delta wing vortex dynamics and the effects on aircraft performance have become an important role. Several variables influence delta wing vortex dynamics. Some of these variables include angle-of-attack, leading edge geometry, wing thickness, sweep angle, freestream conditions and Reynolds number. Reynolds number has to be defined more precisely due to the effect of vortex breakdown location. Vortex breakdown phenomenon is the most important source of buffeting, causing large structural vibrations and severe fatigue damage on an aircraft.

Hebbar et al. (2000) investigated an experimental study of the vortical flow over a double-delta wing model. They observed that the influence of flow Reynolds number on the vortical flow structure. They have found that the strake and wing vortex trajectories tend to move outboards (away from the centerline chord) and closer to the model surface as the flow Reynolds number is increased. The intertwining or coiling-up features of vortex interaction phenomenon dominant in low speed flow patterns gradually disappear at higher Reynolds numbers. And they have also observed the vortex breakdown location, which is characterized by a forward movement towards the apex of the model as the flow Reynolds number is increased. These results are shown in Fig. 3.

Ol and Gharib (2001) compared the flow structure on wings having sweep angles of $\Lambda = 50^o$ and 65^o, using a technique of stereo imaging. Based on patterns of averaged velocity and vorticity in the crosflow plane, they show that the low sweep angle of $\Lambda = 50^o$ exhibits distinctive features, especially at higher angle-of-attack, due to the earlier onset of vortex breakdown and a large-scale collapse of the rolled-up, leading-edge vortex structure. They investigated the $\Lambda = 65^o$ wing normalized velocity profiles for two different Reynolds number at $\alpha = 15^o$.

Fritzelas (1996) has studied the influence of Reynolds number on the high-incidence flow over double-delta wings in his master science thesis. Gursul, Taylor

and Wooding (2002) point out several interesting features of dye-visualized vortex cores on wings of various planforms having relatively low sweep angle.

Taylor et al. (2003) has studied an investigation into vortex structure over a nonslendar delta wing with leading edge sweep, Λ=50 deg. This investigation has included sensitivity of vortex structure to Reynolds Number.

In this section, an experimental study of the vortical flow over a delta wing model was employed in the recirculating water channel at four Reynolds number of 5 000, 7 500, 10 000, and 12 500, using dye-injection technique. The overall of the study was to determine the influence of flow Reynolds number on vortex breakdown location.

Figure 4.3.1.a) is a typical flow visualization photograph showing the vortical flow pattern generated on the model surface at 7^o angle of attack and this Figure illustrates the situation of the vortex breakdown location at Re = 5 000. As can be seen from this Figure, vortex breakdown location of the wing vortices remains outside the wing surface (far downstream of the trailing-edge).

It is seen from the fig. 4.3.1.b) that the location of vortex breakdown moves a little inside the wing surface (just downstream of the trailing-edge). Vortex breakdown location for this case of Re = 7 500 occurs earlier than Re = 5 000 shown in a). Breakdown is developed no further upstream than the midchord of the wing for both cases.

On the other hand, vortex breakdown location moves upstream and remains well inside the wing surface at Re = 10 000 seen in fig. 4.3.1.c). Increasing the Reynolds number causes the movement of vortex breakdown location to the apex of the wing. And the location of the vortex breakdown occurs further upstream than midchord of the wing.

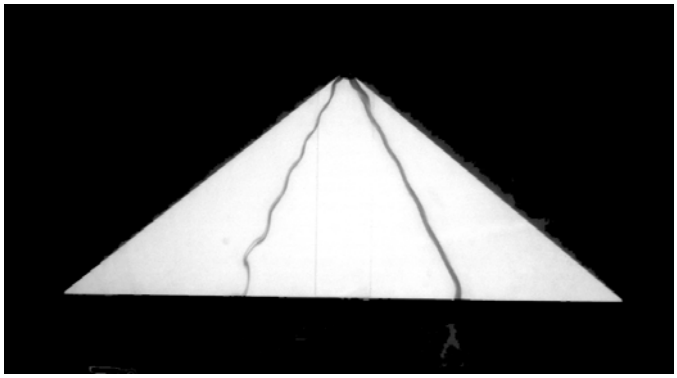
Beside this, with further increase in Reynolds number to 12 500, similar flow visualization like fig. 4.3.1.c) is observed in fig. 4.3.1.d) although the effect is much less dramatic. The flow behavior at two higher Reynolds number is almost similar and the rate of upstream movement of breakdown point is a decreasing function of Reynolds number.

The structure of the flow was very similar to the experimental results of Hebbar et al. (2000) shown in Figure 4.3.2. and especially Taylor et al. (2003) shown in Figure 4.3.3. Taylor et al. (2003) concluded that as Reynolds number was reduced, the trajectory of the primary vortex shifted towards the center-line of the wing, and at very low Reynolds number only a very weak vortex structure was observed. They pointed out that vortex breakdown of the leading edge vortices was delayed significantly. They also concluded that as Reynolds number is increased the flow approaches an asymptotic state, with further increase in the Reynolds number resulting in only small variations in the trajectory of the leading edge vortices. These conclusion are very close to this investigation. In our cases, Fig. 4.3.3.a) through d) clearly indicates that, as the flow Reynolds number increases, the breakdown location moves upstream. To summarize, the flow treatment for Re = 10 000 and 12 500 was very similar whereas the cases of Re = 5 000 to 7 500 were quite distinct.

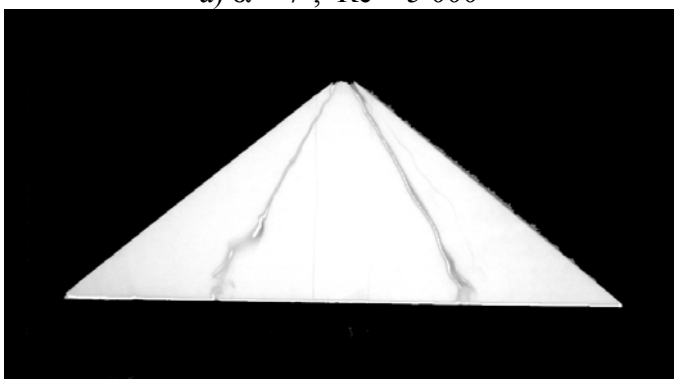
Generally,

(1) The vortex breakdown location characterized by a forward movement through the apex of the wing as the flow Reynolds number is increased. Also, limited observation for Re>10 000 doesn't indicate any noticeable change on vortex breakdown location.

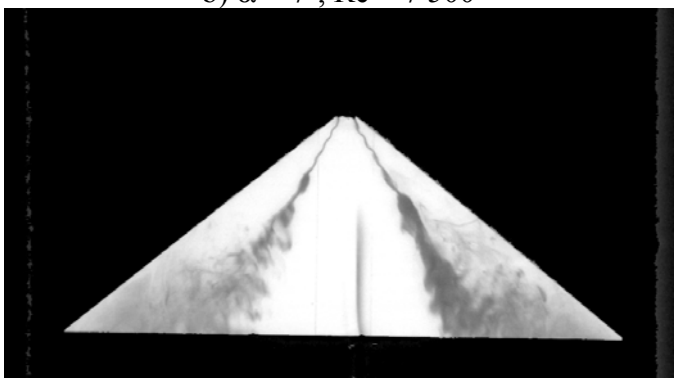
(2) At low flow Reynolds number, such as Re =5 000 and 7 500, considerable effects occur on the flow pattern and vortex breakdown location.



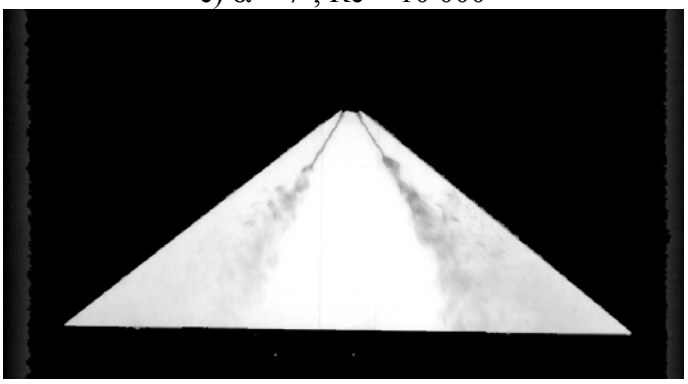
a) $\alpha = 7^o$, Re = 5 000



b) $\alpha = 7^o$, Re = 7 500



c) $\alpha = 7^o$, Re = 10 000



d) $\alpha = 7^o$, Re = 12 500

Figure 4.3.1. Flow visualization at angle-of-attack, $\alpha = 7^o$, Re = 5 000 ~12 5000

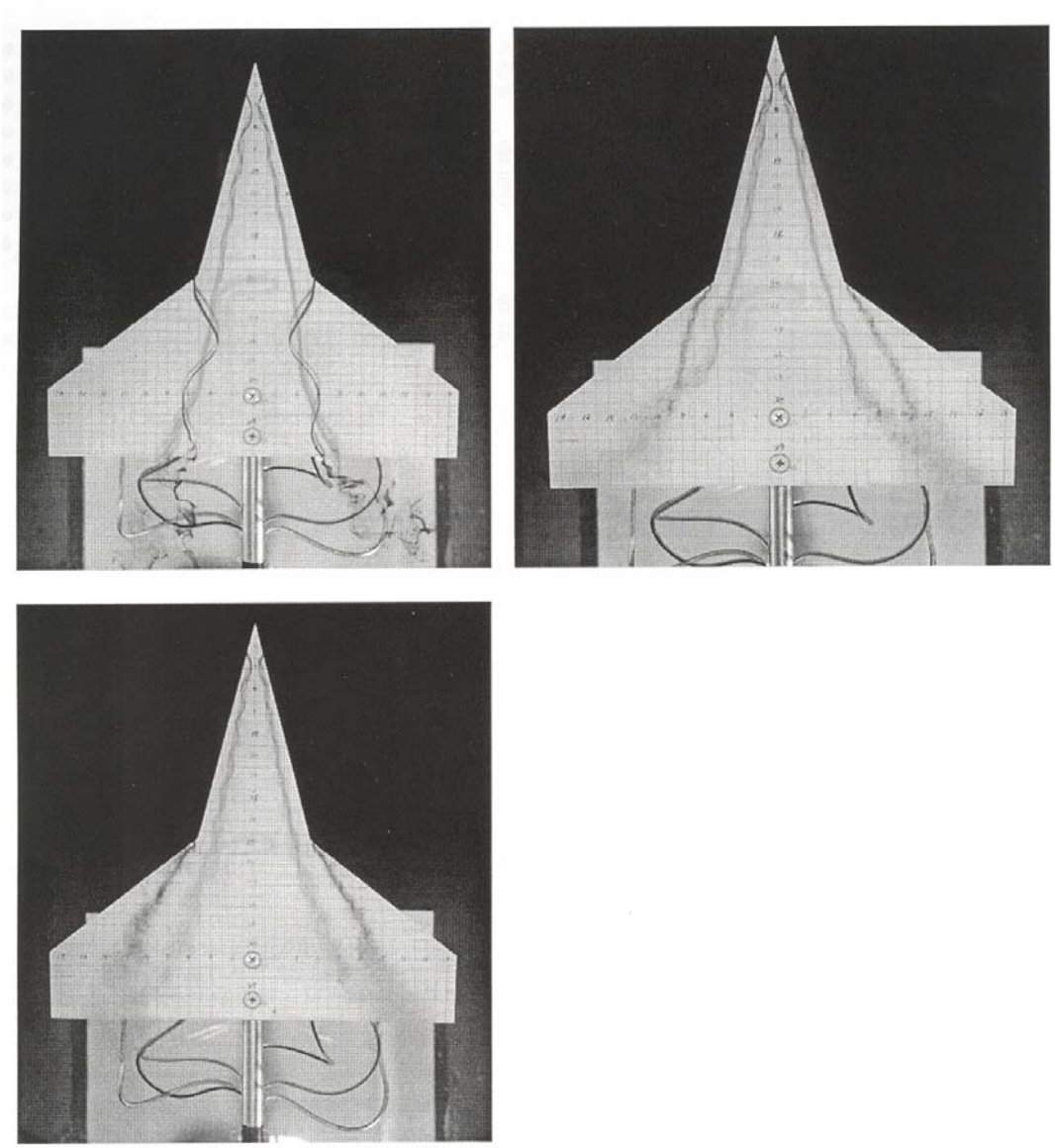


Figure 4.3.2. Strake and wing vortex core trajectories at angle-of-attack, $\alpha = 10$ and Re = 15000, 45 000, 75 000 (from Hebbar et al. (2000)).

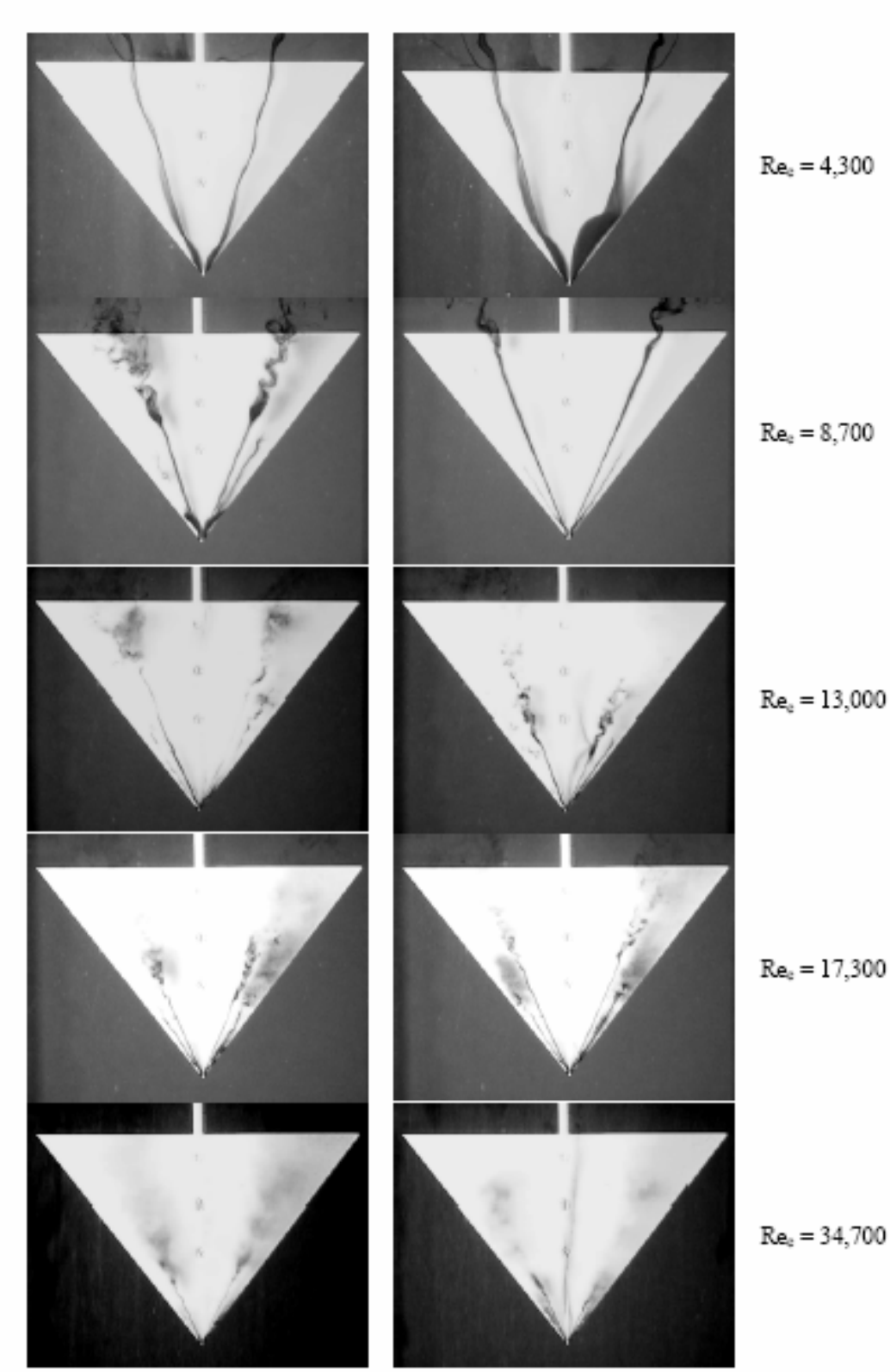


Figure 4.3.2. Extremes of vortex breakdown location Λ= 50 deg. wing at α = 7.5 deg. for selected numbers (from Ref. Taylor et al. (2003)).

5. CONCLUSIONS AND SUGGESTIONS

5.1 Summary of Primary Findings

5.1.1 Flow Structure on a Delta Wing of Low Sweep Angle

The flow structure on a delta wing of low sweep angle exhibits a number of distinctive characteristics, relative to the extensively investigated case of a slender, highly-swept delta wing. Emphasis in the present investigation has been on crossflow planes where vortex breakdown and stall phenomena occur; these phenomena are known to be important origins of unsteady buffet loading of the wing. The primary features of the flow structure, and the potential for their control, are summarized in the following:

The time-averaged flow structure shows a number of distinctive features relative to the structure on wings of relatively high sweep angle. Patterns of averaged velocity show a relatively narrow elongated region of low velocity immediately adjacent to the surface of the wing, which is bounded by a higher speed region. The interface between these two domains of the velocity field represents a region of high shear, and thereby the locus of unsteady events. The corresponding streamline topology exhibits a saddle point that is located outboard of the leading-edge of the wing. At sufficiently high angle-of-attack, the separation streamline from the leading-edge loses its identity. Patterns of averaged vorticity show an elongated layer parallel to the surface of the wing at sufficiently low angle-of-attack, a well-defined, dual vortex substructure system is established. The aforementioned patterns of vortical structures and stall are expected to be a function of Reynolds number. Separation of the shear layer from the leading-edge will be influenced by the existence of small-scale Kelvin-Helmholtz instabilities, of varying scale and circulation, as the Reynolds number is altered. Furthermore, the onset of stall from the surface of the wing may also be a function of Reynolds number. These issues await further investigation.

Unsteadiness of the flow structure is represented by patterns of root-mean-square velocity fluctuation w_{rms}/U normal to the surface of the wing, as well as Reynolds stress correlation $\langle v'w' \rangle / U^2$, both of which are essentially coincident with maxima of the averaged vorticity $\langle \omega \rangle$ of the separated layer. Peak values of these fluctuation quantities occur well inboard of the leading-edge of the wing and their peak magnitudes continue to increase with increasing angle-of-attack up to a moderately high value of α. Then, at sufficiently high angle-of-attack where substantial stall occurs, the peak value is actually decreased.

The instantaneous structure of the flow is represented by patterns of instantaneous vorticity, which take the form of well-defined concentrations. At sufficiently low angle-of-attack, these individual concentrations of vorticity retain their identity, while at moderate and moderately-high values of angle-of-attack, both smaller-scale and larger-scale concentrations are evident. These patterns of instantaneous vorticity concentrations allow physical interpretation of the spectral content of the unsteadiness. Most of the spectral peaks along the separated vorticity layer are relatively broadband and attain maximum amplitude well inboard of the leading-edge. When the averaged vorticity layer deflects towards the surface of the wing near its plane of symmetry, the spectral peaks become small or undetectable. At relatively low angle-of-attack, the same spectral peak persists along the vorticity layer, while at moderate and moderately-high angle-of-attack, the predominant spectral peak is successively lowered with increasing distance inboard of the leading-edge, where larger-scale clusters of vorticity are evident.

When the wing is subjected to small-amplitude perturbations, substantial alterations of both the instantaneous and time-averaged structure were observed. The most effective frequency of excitation corresponds to the subharmonic of the broadband fluctuations in the region of the shear layer closest to the leading-edge, though this criterion is not necessarily universal for other geometric and flow parameters.

5.1.2 Flow Structure on Diamond and Lambda Planforms: Trailing Edge - Region

The abrupt change in sweep angle, which is characteristic of both diamond and lambda planforms, along with the different trailing-edge configurations of these planforms, yields distinctive features of the flow patterns, relative to the case of a simple delta wing.

The streamline topology for both the diamond and lambda planforms shows, at low angle of attack, a focus (apparent center) of a spiral pattern of streamlines at, rather than inboard of, the leading-edge. At moderate angles-of-attack this focus shifts inboard of the leading-edge, and at high-angle-attack, where a large-scale separated zone occurs adjacent to the wing surface, the pattern of streamline topology loses its ordered definition. Furthermore, the occurrence of saddle points (apparent intersection of streamlines) is influenced by a global effect of the trailing-edge configuration. For the lambda planform, a saddle point is located outboard of the leading-edge; for the diamond planform, it is absent.

Corresponding patterns of vorticity show, at all values of angle of attack, a high concentration of vorticity in either the vicinity of, or even at, the leading-edge. In the limiting case of low angle-of-attack, this concentration is nearly centered at the edge, while at larger angles-of-attack, it is displaced significantly away from the edge. Furthermore, well-defined vortical substructures are identifiable in the elongated layers of time-averaged vorticity adjacent to the surface of the wing. These substructures appear to be analogous to those about the periphery of the single, large-scale region of vorticity on a wing of high sweep angle. Corresponding images of instantaneous vorticity show that the elongated layer of average vorticity is actually made up of well-defined vorticity concentrations, whose spacing is very approximately commensurate with those of time-averaged patterns. The spatial positions of these instantaneous vorticity concentrations exhibit substantial modulation from one instantaneous image to the next.

Contours of constant root-mean-square velocity fluctuation adjacent to the wing have extrema that are generally coincident with the outer regions of the

elongated, time-averaged vorticity layers. The spectral content of these fluctuations, evaluated from space-time imaging, shows well-defined peaks, which are associated with the aforementioned modulation of instantaneous vorticity patterns. For extreme, values of low and high angle-of-attack, the dimensionless frequencies of the spectral peaks lie in the range of $2.13 \leq fC/U \leq 3.97$.

5.2 Suggestions for Future Studies

In the present experimental investigation, unsteady pressure or force measurement on the surface of the UCAV planforms were not performed. In order to provide further insight into the induced loading from the unsteady processes of vortex breakdown and stall, unsteady pressure or force must be studied. Critical locations should be determined on the basis of preliminary flow visualization, as well as quantitative representations of the time histories of the surface and exterior streamline patterns. It is anticipated that these locations will correspond to the region immediately downstream of the onset of vortex breakdown, as well as the wake-like regions further downstream.

Another major issue for the suggestions of the investigation should be critically assessed techniques of control/attenuation of the unsteady flow structure, which serves as the genesis of buffeting of aerodynamic surfaces. That is, suitable control of the onset of vortex breakdown and/or the onset and development of large-scale stall regions can fundamentally alter the buffet loading of the wing surface.

Irrespective of the type of control/attenuation technique employed, it is critical to maintain the overall performance characteristics of the aircraft, i.e. to minimize changes in the steady and unsteady lift and moment characteristics.

Most control techniques employed for delta wing configurations have been for relatively large sweep angles and simplified trailing and leading-edges. Blowing or unsteady blowing/suction through the surface of the wing should be applied at a location close to the surface, which gives rise to the development of stall in order to get attenuation of the extent of both the regions of stall and vortex breakdown.

The perturbing of wing cases was studied in the present investigation. Finally, the flow structure over the wing subjected to a pitching motion of a simple sinusoidal or ramp-type with different periods should be studied in order to retard or attenuate the onset of vortex breakdown and stall phenomena.

LIST OF REFERENCES

AKILLI, H. and ROCKWELL, D., 2002. Vortex Formation from a Cylinder in Shallow Water. Physics of Fluids, Vol. 14, No. 9, September, pp. 2957-2967.

AKILLI, H., SAHIN, B. and ROCKWELL, D., 2001. Control of Vortex Breakdown by a Transversely-Oriented Wire. Physics of Fluids, Vol.13, No.2, pp.452-463.

BEAN, D. E. and WOOD, N. J., 1996. Experimental Investigation of Twin Buffeting and Suppression. Journal of Aircraft, Vol. 33, No. 4, pp. 761-767.

BENJAMIN, T. B., 1962. Theory of the Vortex Breakdown Phenomenon. Journal of Fluid Mechanics, Vol. 14, pp. 593-629.

BEUTNER,T. J., BAUST, H. N., and MEYERS, J. F., 1995. Doppler Global Velocimetry Measurements of a Vortex-Tail Interaction. Proceedings of the 7th International Symposium on Flow Visualization, Seattle, Washington, ed. J. P. Crowder, Begell House Inc. NY, pp. 418-423.

BREITSAMTER, C. and LASCHKA, B., 1994. Turbulent Flow Structure Associated with Vortex-Induced Fin Buffeting. AIM Journal of Aircraft, Vol. 31, No. 4, pp. 773-781.

BREITSAMTER, C. and LASCHKA, B., 1998. Fin Buffet Pressure Evaluation Based on Measured Flow Field Velocities. AIAA Journal of Aircraft, Vol. 35, No. 5, pp. 806-815.

BROWN, D., LEE, B. H. K. and TANG, F. C., 1990. Some Characteristics and Effects of the F/A-18 Lex Vortices. Vortex Flow Aerodynamics, AGARD CP 494, pp. 30-1-30-20.

BROWN, G. L. and LOPEZ, J. M., 1990. Asymmetric Vortex Breakdown. Part H Physical Mechanisms. Journal of Fluid Mechanics, Vol.221, pp. 553-576.

CANBAZOGLU, S., LIN, J.-C., WOLFE, S. and ROCKWELL, D., 1995 "Buffeting of Fins: Distortion of Incident Vortex. AIAA Journal, Vol. 33, No. 11, November, pp. 2144-2150.

CHAPMAN, G. T. and YATES, L. A., 1991. Topology of Flow Separation on Three-Dimensional Bodies. Applied Mechanics Review, Vol. 44, No. 7, pp. 329-345.

CHONG, M. S. and PERRY, A. E., 1986.Synthesis of Two- and Three-Dimensional Separation Bubbles. Australasian Fluid Mechanics Conference, 9th, Auckland, New Zealand, December 8-12, Proceedings (A88-3256 12-34).

CIPOLLA, K., and ROCKWELL, D., 1998a. Instantaneous Crossflow Topology on a Delta Wing in Presence of Vortex Breakdown. AIAA Journal of Aircraft, Vol. 35, No. 2, pp. 218-223.

CIPOLLA, K., and ROCKWELL, D., 1998b. Small-Scale Vortical Structures in Crossflow Plane of a Rolling Delta Wing. AIAA Journal, Vol. 36, No. 12, pp. 2276-2278.

DALLMANN, U., HILGENSTOCK, A. and REIDELBAUCH, S., 1990. On the Footprints of Three-Dimensional Separated Vortex Flows around Blunt Bodies. AGARD-CP-494.

DELERY, J. M., 1994. Aspects of Vortex Breakdown. Progress in Aerospace Sciences, Vol. 30, pp. 1-59.

ELKHOURY, M., YAVUZ, M. M. and ROCKWELL, D., 2005. Near-Surface Topology of a Unmanned Combat Air Vehicles Planform: Reynolds Number Dependence. Journal of Aircraft, Vol. 42, No. 5, September/October, 2005, 1318-1330.

ELKHOURY, M. and ROCKWELL, D., 2004. Visualized Vortices on Unmanned Combat Air Vehicles Planform: Effect of Reynolds Number. Journal of Aircraft, Vol. 41, No. 5, pp. 1244-1246.

ERICKSON, G. E., HALL, R. M., BANKS, D. W., DEL FRATE, J. H., SCHREINER, J. A., HANLEY, R. J. and PULLEY, C. T., 1989. Experimental Investigation of the F/A-18 Vortex Flows at Subsonic Through Transonic Speeds, Invited Paper. AIAA Paper 89-2222, July-August.

ESCUDIER, M., 1988. Vortex Breakdown: Observations and Explanations. Progress in Aerospace Sciences, Vol. 25, pp. 189-229.

FRITZELAS, A. E., 1996. A water Tunnel Investigation of The Influence of Reynolds Number on The High-Incidence Flow Over Double-Delta Wings. MS thesis in Aeronautical Engineering, U. S. Naval Postgraduate School, Monetary, CA, USA,.

FALER, J. H., and LEIBOVICH, S., 1978. An Experimental Map of the Internal Structure of a Vortex Breakdown. Journal of Fluid Mechanics, Vol 86, pp. 313-335.

FISHER, D. F, DEL FRATE, J. H. and RICHWINE, D. M., 1989. In-Flight Flow Visualization Characteristics of the NASA F-18 High Alpha Research Vehicle at High Angles of Attack. SAB paper 892222,

DEL FRATE, J. H., FISHER, D. F. and ZUNIGA, F. A., In-Flight Flow Visualization and Pressure Measurements at Low Speeds on the NASA F-18 High Alpha Research Vehicle. NASA-Ames Research Center, Dryden Flight Research Facility, P. 0. Box 273, Edwards, CA 93523-0273.

GAD-EL-HAK, M., and BLACKWELDER, R. F., 1985. The Discrete Vortices from a Delta Wing. AIAA Journal, Vol. 23, No. 6, pp. 961-962.

GAD-EL-HAK, M., and BLACKWELDER, R. F., 1986. Control of the Discrete Vortices from a Delta Wing. AIAA Journal, Vol. 25 No. 8, pp. 1042-1049.

GARG, A. K. and LEIBOVICH, S., 1979. Spectral Characteristics of Vortex Breakdown Flowfields. Physics of Fluids, Vol. 22, No. 11, November, pp. 2053-2064.

GEE, K., MURMAN, S. M., and SCHIFF, L. B., 1995.Computational Analysis of F/A-18 Tail Buffet. AIAA Paper 95-3440.

GORDNIER, R., and VISBAL, M. R., 1991. Numerical Simulation of the Unsteady Vortex Structure over a Delta Wing. AIAA Paper 91-1811.

GORDNIER, R., and VISBAL, M. R., 1994. Unsteady Vortex Structure over a Delta Wing. Journal of Aircraft, Vol. 31, pp. 243-248.

GORDNIER, R. E., and VISBAL, M. R., 1995. Instabilities in the Shear Layer of Delta Wings. AIAA Paper 95-2281.

GORDNIER, R. E. and VISBAL, M. R., 1997. Numerical Simulation of the Impingement of a Streamwise Vortex on a Plate. AIAA Paper No. 97-17812, 8th AIAA Fluid Dynamics " Conference, June 29-July 2, Snowmass Village, CO.

GORDNIER, R. E, and VISBAL MR., 2003. Higher-order compact difference scheme applied to the simulation of a low sweep delta wing flow. AIAA 2003-

0620, 41st AIAA Aerospace Sciences Meeting and Exhibit, 6–9 January 2003, Reno, NV.

GU, W., ROBINSON, O. and ROCKWELL, 1993. Control of Vortices on a Delta Wing by Leading-Edge Injection. AIAAJournal, Vol. 32, No. 7, pp. 1177-1186, 1993.

GUPTA AK, LİLLEY DG, and SYRED N., 1984. Swirl flows, energy and engineering science series. London: Abacus Press.

GURSUL, I., 1994. Unsteady Flow Phenomena Over Delta Wings at High Angle-of-Attack. AIAA Journal, Vol. 32, No. 2, February, pp. 225-231.

GURSUL, I. and YANG, H., 1994b. Vortex Breakdown Over a Pitching Delta Wing. AIAA Paper No. 94-0536, 32nd Aerospace Sciences Meetining and Exhibit, January 10-13, Reno, NV.

GURSUL, I. and YANG, H., 1995. On Fluctuations of Vortex Breakdown Location. Physics of Fluids, Vol. 7, No. 1, January, pp. 229-231.

GURSUL, I., GORDNİER, R. and VISBAL, M., 2005. Unsteady aerodynamics of nonslender delta wings Progress in Aerospace Sciences 41, pp.515–557.

GURSUL, I., TAYLOR, G., and WOODING, C. L., 2002. Vortex Flows over Fixed-Wing Micro Air Vehicles. AIAA Paper 0648.

HELIN, H. E. and WATRY, C. W., 1994. Effects of Trailing-Edge Entrainment on Delta Wing Vortices. AIAA Journal, Vol. 32, pp. 802-804.

HEBBAR, S. K., PLATZER, M. F., and FRITZELAS, A. E., 2000. Reynolds Number Effects on The Vortical Flow Structure Generated by a Double-Delta Wing. Experiments in Fluids, Vol. 28, pp. 206-216.

HONKAN, A., and ANDREOPOULOS, J., 1997. Instantaneous Three-Dimensional Vorticity Measurements in Vortical Flow over a Delta Wing. AIAA Journal, Vol. 35, No. 10, October, 1997, pp. 1612-1620.

HORNUNG, H. and PERRY, A. E., 1984. Some Aspects of Three-Dimensional Separation. Part I: Streamsurface Bifurcations. Zeitschrift fuer Flugwissenschaftern und Weltraumforschunt, Vol. 8, pp. 77-87.

HUNT, J. C. R., ABELL, C. J., PETERKA, J. A. and WOO, H., 1978. Kinematical Studies of the Flows around Free or Surface-Mounted Obstacles; Applying

Topology to Flow Visualization. Journal of Fluid Mechanics, Vol. 86, pp. 179-200.

HUNECKE, K., 1987. Modern Combat Aircraft Design, Naval Institute Press, Annapolis. Maryland, pp. 24-27, 51-59.

HUTTSELL, L. J., TINAPPLE, J. A. and WEYER, R. M., 1997. Investigation of Buffet Loading on a Scaled F-15 Twin Tail Model. AGARD Strucutres and Materials Panel Workshop, October, Denmark.

JEFFERIES, R. and ROCKWELL, D., 1996. Interactions of a Vortex with an Oscillating -J-Leading-Edge. AIAA Journal, Vol. 34, No. 11, pp. 2448-2450.

KANDIL, O. A., SHETA, E. F., and MASSEY, S. J., 1995. Buffet Responses of a Vertical Tail in Vortex Breakdown Flows. AIAA Paper No. 95-3464.

KOMERATH, N. M., LIOU, S. G., SCHWARTZ, R. J. and KIM, J. M., 1992a. Flow Over a Twin-Tailed Aircraft at Angle of Attack, Part I: Spatial Characteristics. Journal of Aircraft, Vol. 29, No. 3, pp. 413-420.

KOMERATH, N. M., LIOU, S. G., SCHWARTZ, R. J. and KIM, J. M., 1992b. Flow Over a Twin-Tailed Aircraft at Angle of Attack, Part II: Temporal Characteristics. Journal of Aircraft, Vol. 29, No. 4, pp. 553-558.

LAMBOURNE, N.C., and BRYER, D.W., 1961. The Bursting of Leading-Edge Vortices – Some observations and Discussion of the Phenomenon. ARC R&M 3282.

LAN, C. E., and LEE, I. G., 1986. Investigation of Empennage Buffeting. NASA CR-179246, January.

LEE, B. H. K., 1979. A Theoretical Study of the Response of a Wing to Quasi-Stationary Correlated Noise Inputs. LTR-HA-38, National Research Council of Canada, May.

LEE, B. H. K., 1980. A Method for the Prediction of Wing Response to Non-Stationary Buffet Load. LR-601, NRC No. 18629, National Research Council of Canada, July.

LEE, B. H. K., 1984. A Method for Predicting Wing Response to Buffet Loads. Journal of Aircraft, Vol. 21, No. 1, pp. 85-87.

LEE, B. H. K., 2000. Vertical Tail Buffeting of Fighter Aircraft. Progress in

Aerospace Sciences, Vol. 36, pp. 193-279.

LEE, B. H. K., and BROWN, D., 1992. Wind-Tunnel Studies of F/A-18 Tail Buffet. Journal of Aircraft, Vol. 29, No. 1, pp. 146-152.

LEE, B. H. K., BROWN, D., ZIGELA, L. M. and POIREL, D., 1990. Wind Tunnel Investigation and Flight Tests of Tail Buffet on the CF-18 Aircraft. Aircraft Dynamic Loads Due to Flow Separation, Paper 1 (Sorrento, Italy), pp. 1-1-1-26 (AGARD CP-483).

LEE, B. H. K. and DUNLAVY, S., 1992. Statistical Prediction of Maximum Buffet Loads on the F/A-18 Vertical Fin. Journal of Aircraft, Vol. 29, No. 4, pp. 734-736.

LEGENDRE, R., 1956. Separation de 1'ecoulement Laminaire Tritiamensionnel. Rech. Aero.,Vol 54, pp. 3-8.

LEIBOVICH, S., 1978. Structure of Vortex Breakdown. Annual Review of Fluid Mechanics, Vol. 10, pp. 221-246.

LEIBOVICH, S., 1984. Vortex Stability and Breakdown: Survey and Extension. AlAA Journal, Vol. 22, pp. 1192-1206. ,

LIGHTHILL, M. J., 1963. In Laminar Boundary Layers (Ed. L. Rosenhead). pp. 48-88, Oxford University Press.

LIN, J.-C. and ROCKWELL, D., 1994. Cinematographic System for High-Image-Density Particle Image Velocimetry. Experiments in Fluids, Vol. 17, pp. 110-118,1994.

LIN, J.-C., and ROCKWELL, D., 1995. Transient Structure of Vortex Breakdown on a Delta Wing. AIAA Journal, Vol. 33, pp. 5-12.

LIN, J.-C., and ROCKWELL, D., 1999. Cinema PTV and Its Application to Impinging Vortex Systems. Journal of Fluids Engineering, Vol. 121, No. 4, December, pp. 720-724.

LIN, J.C. and ROCKWELL D., 2001. Organized oscillations of initially turbulent flow past a cavity. AIAA Journal, 39, 6, 1139-1150.

LIN, J.C.,1994. NFILVB Software, Fluid Mechanics Lab, Lehigh University.

LIN, J.C.,1996. NWENSAV2 software, Fluid Mechanics Lab, Lehigh University.

LOPEZ, J. M. and PERRY, A. D., 1992. Axisymmetric Vortex Breakdown. Part 3.

Onset of Periodic Flow and Chaotic Advection. Journal of Fluid Mechanics, Vol. 234, pp. 449-471.

LOWSON, M. V., 1988. The Three-Dimensional Vortex Sheet Structure on Delta Wings. In Fluid Dynamics of Three-Dimensional Turbulent Shear Flows and Transition, October, Agard-CP-438, paper11.

MAGNESS, C, ROBINSON, O., and ROCKWELL, D., 1992. Unsteady Crossflow on a Delta Wing Using Particle Image Velocimetry. AIAA Journal of Aircraft, Vol. 29, No. 4, pp. 707- Tp1 709.

MAGNESS, C., ROBINSON, O., and ROCKWELL, D., 1993a. Laser-Scanning Particle Image Velocimetry Applied to a Delta Wing in Transient Maneuver. Experiments in Fluids, Vol. 15, No. 3, pp. 159-167.

MAGNESS, C., ROBINSON, O., and ROCKWELL, D., 1993b. Instantaneous Topology of the Unsteady Leading-Edge Vortex at High Angle of Attack. AIAA Journal, Vol. 31, No. 8, pp. 1384-1391.

MARTIN, C. A., and THOMPSON, D. H., AGARD CP 497 "Scale Model Measurements of Fin Buffet Due to Vortex Bursting on F/A-18".

MABEY, D. G., 1973. Beyond the Buffet Boundary. Aeronautical Journal, Vol. 11, No. 148, pp. 201-214.

MAYORI, A., and ROCKWELL, D., 1994. Interaction of a Streamwise Vortex with a Thin Plate: A Source of Turbulent Buffeting. AIAA Journal, Vol. 32, pp. 2022-2029.

MENKE, M., and GURSUL, I., 1997. Unsteady Nature of Leading Edge Vortices. Physics of Fluids, Vol. 9, No, 10, pp. 2610-2616.

MENKE, M., YANG, H., and GURSUL, I., 1996. Further Experiments on Fluctuations of Vortex Breakdown Location. AIAA Paper No. 96-0205, 34th Aerospace Sciences Meeting and Exhibit, January 15-18, Reno, NV.

MENKE, M., YANG, H., and GURSUL, I., 1999. Experiments on the Unsteady Nature of Vortex Breakdown over Delta Wings. Experiments in Fluids, Vol. 27, pp. 262-272.

MITCHELL, A., MOLTON, P., BARBERIS, D., and DELERY, J., 2000. Characterization of Vortex Breakdown by Flow Field and Surface Measurements. AIAA Paper 2000-0788.

MITCHELL, M. A., and DELERY, J., 2001. Characterization of Vortex Breakdown by Flow Field and Surface Measurements. Progress in Aerospace, pp.385-418.

MIAU, J. J., KUO, K. T., LIU, W H., HSIEH, S. J., CHOU, J. H., and LIN, C. L., 1995. Flow Developments Above 50-deg Sweep Delta Wings with Different Leading-Edge Profiles. Journal of Aircraft, Vol. 32, No. 4, pp. 787-794.

NEWLAND, D. E., 1993. Random Vibrations, Spectral and Wavelet Analysis. 3rd Edition, Longman Group Ltd., England.

OL, M. V., and GHARIB, M., 2001. The Passage Toward Stall of Nonslendar Delta Wings at Low Reynolds Number. AIAA Paper 2001-2843..

OL, M. V., and GHARİB, M.. 2003. Leading-Edge Vortex Structure of Nonslender Delta Wings at Low Reynolds Number. AIAA Journal, Vol. 41, No. 1, 2003, pp. 16-26.

OZGOREN, M., SAHIN, B., and ROCKWELL, D., 2001. Perturbations of a Delta Wing: Control of Vortex Breakdown and Buffeting. Journal of Aircraft, Vol.38, No.6, pp.1040-1050.

OZGOREN, M., SAHIN, B., and ROCKWELL, D., 2002a. Vortex Structure on a Delta Wing at High Angle-of-Attack", AIAA Journal, Vol.40, No.2, pp.285-292.

OZGOREN, M., SAHIN, B., and ROCKWELL, D., 2002b. Vortex Breakdown from a Pitching Delta Wing Incident Upon a Plate: Flow Structure as the Origin of Buffet Loading. Journal of Fluids and Structures, Vol.16, No.3, pp.295-316.

PAYNE, F.M., NG, T.T., NELSON, R.C., and SCHIFF, L.B., 1988. Visualization and Wake Surveys of Vortical Flow Over Delta Wing. AIAA Journal, Vol. 26, No. 2, pp. 137-143.

PEAKE, D. J., and TOBAK, M., 1982. Three-Dimensional Separation and Reattachment. AGARD-LS-121.

PERRY, A. E., and CHONG, M. S., 1987. A Description of Eddying Motions and Flow Patterns Using Critical-Point Concepts. Annual Review of Fluid

Mechanics, Vol. 19, pp. 125-155.

RANQUE GJ., 1933. J Phys Radium, 4:112S-5S.

REYNOLDS, G. A., and ABTAHI, A. A., 1989. Three-Dimensional Vortex Development, Breakdown and Control. AIAA-89-0998, March.

REDINIOTİS, O. K., KLUTE, S. M., HOANG, N. T. and TELIONIS, D. P., 1994. Pitch-Up Motions of Delta Wings. AIAA Journal, Vol. 32, No. 4, pp. 716-725.

RILEY, A. J., and LOWSON, M. V., 1998. Development of a Three-Dimensional Free Shear Layer. Journal of Fluid Mechanics, Vol. 369, pp. 49-89.

RIZK, Y. M., and GEE, K., 1992. Unsteady Simulation of Viscous Flow Field Around F-18 Aircraft at Large Incidence. Journal of Aircraft, Vol. 29, pp. 986-992.

RIZZETTA, D. P., 1996. Numerical Simulation of the Interaction Between a Leading-Edge Vortex in a Vertical Tail. AIAA Paper No, 96-2012, 27th AIAA Fluid Dynamics Conference, June 17-20, New Orleans, LA.

ROCKWELL, D., 1998. Vortex-Body Interactions. Annual Review of Fluid Mechanics, Vol. -J-30, pp. 199-229.

ROCKWELL, D., 2000. Imaging of Unsteady Separated Flows: Global Interpretation with Particle Image Velocimetry. Experiments in Fluids, Supplement, pp. S255-S273.

ROOS, F. W., and KEGELMAN, J. T., 1990. Recent Explorations of Leading-Edge Vortex Flowfields", NASA High-Angle-of-Attack Technology Conference. NASA Langley Research Center, Hampton, VA, October 30-November 1.

RUSAK, Z, WANG, S., and WHITING, C. H., 1998. The Evolution of a Perturbed Vortex in a Pipe to Axisymmetric Vortex Breakdown. Journal of Fluid Mechanics, Vol. 366, pp. 211-237.

SAHIN, B., AKILLI, H., LIN, J.-C., and ROCKWELL, D., 2001. Vortex Breakdown-Edge Interaction: Consequence of Edge Oscillations. AIAA Journal, Vol.39, No.5, pp.865-876.

SARPKAYA, T., 1971a. On Stationary and Traveling Vortex Breakdowns. Journal of Fluid Mechanics, Vol. 45, No. 3, pp. 545-559.

SARPKAYA, T., 1971b. Vortex Breakdown in Swirling Conical Flows. AIAA

Journal, Vol. 9, No, 9, pp. 1792-1799.

SARPKAYA, T., 1974. Effect of the Average Pressure Gradient on Vortex Breakdown. AIM Journal, Vol. 12, No. 5, pp. 602-607.

SARPKAYA, T., 1995. Vortex Breakdown and Turbulence. AIAA paper, No:95-0433.

SELLERS, W. L., MEYERS, J. F., and HEPNER, T. E., 1988. LDV Surveys over a Fighter Model at Moderate to High Angles of Attack. Society of Automotive Engineers TP Series Paper 88-1448, October.

SHAH, G. H., 1991. Wind-Tunnel Investigation of Aerodynamic and Tail Buffet Characteristics of Leading-Edge Extension Modification to F/A-18", AIAA Paper No. 91-2889. AIAA Atmospheric Flight Dynamics Conference, August 12-14, New Orleans, Louisiana.

SHIH, C., and DING, Z., 1996. Trailing-Edge Jet Control of Leading-Edge Vortices of a Delta Wing. AIAA Journal, Vol. 34, No. 7, pp. 1447-1457.

SQUIRE, L. C., 1962. The Motion of a Thin Oil Sheet Under the Boundary Layer on a Body. AGARDOgraph 70.

SU, W., LIU, M., and LIU, Z., 1990. Topological Structures of Separated Flows about a Series of Sharp-Edged Delta Wings at Angles of Attack up to 90°", Topological Fluid Mechanics (eds. H. K. Moffatt and A. Tsinober). Proceedings of the IUTAM Symposium, Cambridge, August 13-18, 1989.

SWITHENBANK J., and CHİGİER NA., 1969. Vortex mixing for supersonic combustion. 21st International Symposium on Combustion, p. 1154-62.

SYRED, N., and BEER JM., 1974. Combustion in swirling flows: a review. Combustion and Flame, 23:143-201.

TAYLOR, G. S., SCHNORBUS, T., and GURSUL, I., 2003. An Investigation of Vortex Flows over Low Sweep Delta Wings. AIAA-2003-4021, AIAA Fluid Dynamics Conference, 23-26 June, Orlando, FL.

TAYLOR, G. and GURSUL, I., 2004. Unsteady Vortex Flows and Buffeting of a Low Sweep Delta Wing. AIAA-2004-1066, 42nd Aerospace Sciences Meeting and Exhibit, January 3-8, Reno, NV.

TRIPLET, W. E., 1983. Pressure Measurements on Twin Vertical Tails in Buffeting

Flow. Journal of Aircraft, Vol. 20, No. 11, pp. 920-925.

TOWFIGHI, J., and ROCKWELL, D., 1993. Instantaneous Structure of Vortex Breakdown on a Delta Wing Via Particle Image Velocimetry., AIAA Journal, Vol. 31, pp. 1160-1162.

VISBAL, M. R., and GORDNIER, R. E., 2003. On the Structure of the Shear Layer Emanating from a Swept Leading Edge at Angle of Attack. AIAA Paper No. 2003-4016, 33rd Fluid Dynamics Conference and Exhibit, 23-26 June, 2003, Orlando, FL.

VISBAL, M. R., 1995. Computational and Physical Aspects of Vortex Breakdown on Delta Wings. AIAA Paper, No.95-0585.

WANG, S., and RUSAK, Z., 1997. The Dynamics of a Swirling Flow in a Pipe and Transition to Axisymmetric Vortex Breakdown. Journal of Fluids Mechanics, Vol. 340. pp. 177-223.

WASHBURN, A. E., and VISSER, K. D., 1994. Evolution of Vortical Structures in the Shear Layer of Delta Wings. AIAA Paper No. 94-2317.

WEBER R., BOYSAN, F., SWITHENBANK J., and ROBERTS PA., 1986. Computation of near field aerodynamics of swirling expanding flows. 21st International Symposium on Combustion, pp. 1435-43.

WENTZ, W. H., and ARID KOHLMAN, D. L., 1971. Vortex Breakdown on Slender, Sharp-Edged Wings. Journal of Aircraft, Vol. 8, No. 3, March.

WERLE, H., 1974. Le Tunnel Hydrodynamique au Service de la Recherche Aerospatiale. ONERA Publication No. 156.

WERLE, H., 1960. Sur leclatement des tourbillons d'apex d'une aile delta aux faibles vitesses. La Recherche Aeronautique No. 74, Janvier–Fevrier,.

WOLFE, S., CANBAZOGLU, S., LIN, J.-C., and ROCKWELL, D., 1995. Buffeting of Fins; An Assessment of Surface Pressure Loading. AJAA Journal, Vol. 33, No. 11, pp. 2232-2235.

YANIKTEPE, B., and ROCKWELL D., 2004. Flow structure on a delta wing of low sweep angle. AIAA Jornal, 42(3):513–23.

YAVUZ, M., ELKHOURY, M., and ROCKWELL, D., 2004. Near-Surface Topology and Flow Structure on a Delta Wing. AIAA Journal, Vol. 42, No. 2, pp. 332-340.

ZIMMERMAN, N. H., FERMAN, M. A., YURKOVICH, R. N., and GERSTENKORN, G., 1987. Prediction of Tail Buffet Loads for Design Applications. Report NADC-88-434-60, July.

ZIMMERMAN, N. H., FERMAN, M. A., YURKOVICH, R. N., and GERSTENKOM, G., 1989. Prediction of Tail Buffet Loads for Design Applications. AIAA Paper 89-1378, April.

ÖZ GEÇMİŞ

Bülent YANIKTEPE 18 Ağustos 1975 yılında OSMANİYE'nin Bahçe kazasında doğdu. 1992 yılında SAKARYA Hendek Lisesinden mezun olduktan sonara 1993 yılında Çukurova Üniversitesi Makine Mühendisliği Bölümünü kazandı. Makine Mühendisliği Bölümünden 1998 yılında mezun oldu. Aynı yıl, Makine Mühendisliği Bölümünde Yüksek Lisans öğrenimine başladı ve aynı bölümde Araştırma Görevlisi olarak çalışmaya başladı. Yüksek lisans öğrenimini 2000 yılında tamamlayarak aynı bölümde doktora öğrenimine başladı. Doktora tez çalışmalarının deneylerini yapmak üzere 2001-2002 yılları arasında Amerika Birleşik Devletleri, Lehigh Üniversitesi, Makine Mühendisliği ve Mekanik Bölümü Akışkanlar Mekaniği Laboratuarında ziyaretçi araştırmacı olarak çalışmalarda bulundu.

Çukurova üniversitesinden ayrılarak 2004 yılında Sanayi ve Ticaret Bakanlığı Sanayi Araştırma ve Geliştirme Genel Müdürlüğünde Mühendis olarak çalışmaya başladı. Bakanlıkta ülkemizi temsilen Bilim ve Araştırma, İşletmeler ve Sanayi Politikaları fasıllarında müzakere heyetine katıldı. İşletmeler ve Sanayi Politikaları faslında Avrupa Birliği Komisyon heyetine "Yenilikçilik" başlığında bir sunum yaptı. Teknoparklar, üniversite sanayi işbirliği, yenilikçik, araştırma ve geliştirme, Avrupa Birliğinde araştırma ve geliştirme ve yenilikçilik konularında uzman olarak halen Sanayi ve Ticaret Bakanlığında çalışmaktadır.

APPENDIX A

Vorticity Evaluation

For 2-D flows, the out-of-plane component of vorticity is given by:

$$\Omega = \frac{1}{2}\left(\frac{\partial v}{\partial x} - \frac{\partial u}{\partial y}\right)$$

The most common way to compute this expression numerically is to approximate the partial derivatives with finite difference. Using central differences at an interior point to leads to:

$$\Omega_{ij} = \frac{1}{2}\left(\frac{v(i+1, j) - v(i-1, j)}{2\delta_x} - \frac{u(i, j+1) - u(i, j-1)}{2\delta_y}\right)$$

Any computation involving derivatives is very sensitive to noises that are the primary reason to try to smooth out the velocity field before computation of the vorticity, strain rate or similar gradient quantities.

Another way around the noise problem for the particular case of the computation of vorticity is to use a self-smoothing method derived from the Stokes theorem. This the so-called circulation method that the user can choose to compute the vorticity in NFILVB.

The stokes theorem can be formulated as:

$$\iint \left(\vec{\nabla} \times \vec{u}\right) d\vec{s} = \oint \vec{u} d\vec{l}$$

Assuming that the vorticity is constant all over the unit surface formed by the four grid cells surrounding a given point, the vorticity a that point is given by:

$$\Omega = \frac{1}{4\delta_x \delta_y} \oint \vec{u} d\vec{l}$$

where the integral is the circulation of the velocity around the path formed by the sides of the unit surface.

APPENDIX B

Bilinear Interpolation

To fill the gaps left in the data grid by the interrogation system NFILVB is using a bilinear least square fit technique.

Knowing the data values u_1,….., u_n at the N nearest neighbor location of a point where the data u is missing, the idea is to find a value for u that does not deviate too much from these values. To realize this goal, in a least square technique, one has to minimize the merit function:

$$\chi^2 = \sum_{k=1}^{N} \frac{|u_k - u|^2}{\sigma_k}$$

As suggested by Adrian et al., NFILVB is applying this method to a linear model of the 2 components of velocity:

$u=a_0+a_1x+a_2y$

$v=b_0+b_1x+b_2y$

using the 5 nearest neighbors of a missing data. The standard way to deal with the measurement errors σ_k, on each data u_k, when they are not known, is to set them to 1. The minimum of the merit function:

$$\chi^2 = \sum_{k=1}^{5} |u_k - (a_0 + a_1 x + a_2 y)|^2$$

occurs when:

$$\frac{\partial \chi^2}{\partial a_0}(x_k, y_k) = \frac{\partial \chi^2}{\partial a_1}(x_k, y_k) = \frac{\partial \chi^2}{\partial a_2}(x_k, y_k) = 0 \quad \text{for k=1,……..,5}$$

This is a linear system of 15 equations and 3 unknowns that is solved using the Singular Value Decomposition (SVD) technique described in the Numerical Recipes books.

Gaussian Smoothing

To reduce the measurement noises in the velocity data from PIV, a local weighted averaging technique is used in NFILVB. The weights used are Gaussian:

$$u(x_i, y_j) = \sum_{m=-4}^{4} \sum_{k=-4}^{4} w_{km} u(x_{i-k}, y_{j-m})$$

where:

$$w_{km} = \frac{\omega_{km}}{\sum_{k=-4}^{4} \sum_{m=-4}^{4} \omega_{km}}$$

and $\omega_{km} = e^{\frac{2(k^2+m^2)}{\sigma^2}}$

The parameter σ is the smoothing parameter that the user is asked for when running NFILVB. It controls how fast the Gaussian ω is decaying and therefore, determines the contributions of the surrounding points to the average value.

APPENDIX C

Averaged Flow Structure

Calculation of the averaged quantities was performed according to the equations listed in the flowing table. Each averaged parameter was calculated at each spatial coordinate (x,y) by considering the average of all instantaneous values (x,y). The terminology for each of the averaged parameters and the dimensionless equation employed to determine the averaged parameter as follows:

<V> ≡ averaged (or mean) total velocity

$$< V > \equiv \frac{1}{N}\sum_{n=1}^{N} V_n(x,y)$$

<u> = averaged value of streamwise component of velocity

$$< u > \equiv \frac{1}{N}\sum_{n=1}^{N} u_n(x,y)$$

<v> = averaged value of transverse component of velocity

$$< v > \equiv \frac{1}{N}\sum_{n=1}^{N} v_n(x,y)$$

<ω> = mean value of vorticity

$$< \omega > \equiv \frac{1}{N}\sum_{n=1}^{N} \omega_n(x,y)$$

u_{rms} = root-mean-square of u component fluctuation

$$u_{rms} \equiv < u >_{rms} \equiv \left[\frac{1}{N}\sum_{n=1}^{N} \left[u_n(x,y) - < u(x,y) > \right]^2 \right]^{1/2}$$

v_{rms} = root-mean-square of v component fluctuation

$$v_{rms} \equiv < v >_{rms} \equiv \left[\frac{1}{N} \sum_{n=1}^{N} \left[v_n(x,y) - < v(x,y) > \right]^2 \right]^{1/2}$$

$< u'v' >$ = averaged value of Reynolds stress correlation

$$< u'v' > = \frac{1}{N} \sum_{n=1}^{N} \left[u_n(x,y) - < u(x,y) > \right] \left[v_n(x,y) - < v(x,y) > \right]$$

APPENDIX D

Spectral Analysis

In order to estimate spectra from measured data, the obvious method is to estimate the appropriate correlation function first and than Fourier transform this function to obtain the required spectrum. Until the late 1960s, this approach was the basis of practical calculation procedures which followed the formal mathematical route by which spectra are defined as Fourier transform of correlation functions. Newland (1993)

From the book of Newland (1993), spectral density functions of random process can be defined as the fourier transforms of corresponding auto- and cross-corrleation fuctions. Therefore if $R_{xx}(\tau)$ and $R_{xy}(\tau)$ are auto and cross-corrlation functions, the auto-and cross-spectral density can be defined as

$$S_{xy}(\bar{\omega}) = \frac{1}{2\pi}\int_{-\infty}^{\infty} R_{xy}(\tau) e^{-i\bar{\omega}\tau} d\tau \qquad 1$$

$$S_{yx}(\bar{\omega}) = \frac{1}{2\pi}\int_{-\infty}^{\infty} R_{xy}(\tau) e^{-i\bar{\omega}\tau} d\tau \qquad 2$$

and their accompanying transform relations which are

$$R_{xx}(\tau) = \frac{1}{2\pi}\int_{-\infty}^{\infty} S_{xy}(\omega) e^{i\omega\tau} d\omega \qquad 3$$

$$R_{yx}(\tau) = \frac{1}{2\pi}\int_{-\infty}^{\infty} S_{yx}(\omega) e^{i\omega\tau} d\omega$$

Due to cross-corrlelation functions are related by $R_{xy}(\tau) = R_{yx}(-\tau)$, equ. 1 becomes in the form of

$$S_{xy}(\omega) = \frac{1}{2\pi}\int_{-\infty}^{\infty} R_{yx}(-\tau) e^{-i\omega\tau} d\tau \text{ and substituting } \tau' = -\tau$$

$$S_{xy}(\omega)=\frac{1}{2\pi}\int_{-\infty}^{\infty}R_{yx}(\tau')e^{-i\omega\tau'}d\tau' \qquad 4$$

is obtained.

Since FFT originally works with complex data to write equ. 4 in the complex form, let x(t) is a fuction of time, with period T,

$$x(t)=a_o+\sum_{k=1}^{\infty}\left(a_k\cos\frac{2\pi kt}{T}+b_k\sin\frac{2\pi kt}{T}\right) \qquad 5$$

where a_0 and a_k and b_k are constont Fourier coefficients given by

$$a_0=\frac{1}{T}\int_{-T/2}^{T/2}x(t)dt$$

$$a_{\substack{k\\k\geq 1}}=\frac{2}{T}\int_{-T/2}^{T/2}x(t)\cos\frac{2\pi kt}{T}dt \qquad 6$$

$$b_{\substack{k\\k\geq 1}}=\frac{2}{T}\int_{-T/2}^{T/2}x(t)\sin\frac{2\pi kt}{T}dt$$

Substituting 6 into 5 for a_0=0

$$x(t)=\sum_{k=1}^{\infty}\left\{\frac{2}{T}\int_{-T/2}^{T/2}x(t)\cos\frac{2\pi kt}{T}dt\right\}\cos\frac{2\pi kt}{T}+\sum_{k=1}^{\infty}\left\{\frac{2}{T}\int_{-T/2}^{T/2}x(t)\sin\frac{2\pi kt}{T}dt\right\}\sin\frac{2\pi kt}{T}$$

Next substituting for $\omega_k=\frac{2\pi k}{T}$ and $\Delta\omega=\frac{2\pi}{T}$

$$x(t)=\sum_{k=1}^{\infty}\left\{\frac{\Delta\omega}{\pi}\int_{-T/2}^{T/2}x(t)\cos\omega_k tdt\right\}\cos\omega_k t+\sum_{k=1}^{\infty}\left\{\frac{\Delta\omega}{\pi}\int_{-T/2}^{T/2}x(t)\sin\omega_k tdt\right\}\sin\omega_k t$$

when the period $T \to \infty, \Delta\omega \to d\omega$ and the $\sum$ becomes an integral with the limits $\omega = 0$ *to* $\omega = \infty$. In this case

$$x(t) = \int_{\omega=0}^{\infty} \frac{d\omega}{\pi} \left\{ \int_{-\infty}^{\infty} x(t) \cos \omega_k t dt \right\} \cos \omega_k t + \int_{\omega=0}^{\infty} \frac{d\omega}{\pi} \left\{ \int_{-\infty}^{\infty} x(t) \sin \omega_k t dt \right\} \sin \omega_k t$$

or putting

$$A(\omega) = \frac{1}{2\pi} \int_{-\infty}^{\infty} x(t) \cos \omega t dt \qquad 7$$

$$B(\omega) = \frac{1}{2\pi} \int_{-\infty}^{\infty} x(t) \sin \omega t dt$$

gives $x(t) = 2\int_{0}^{\infty} A(\omega) \cos \omega t d\omega + 2\int_{0}^{\infty} B(\omega) \sin \omega t d\omega \qquad 8$

The terms $A(\omega)$ and $B(\omega)$ defined by equ. 7 are the components of the Fourier transform of x(t) and equ. 8 is a representation of x(t) by a Fourier integral of inverse Fourier transform.

To write equations 7 and 8 in complex form making use of the result that

$$e^{i\theta} = \cos\theta + i \sin\theta \qquad 9$$

Defining

$X(\omega) = A(\omega) - iB(\omega)$ equations may be combined to give

$$X(\omega) = \frac{1}{2\pi} \int_{-\infty}^{\infty} x(t) (\cos \omega t - i \sin \omega t) dt$$

$$= \frac{1}{2\pi} \int_{-\infty}^{\infty} x(t) e^{-i\omega t} dt \qquad 10$$

from equation 9. The latter equation is the formal definition of $X(\omega)$ which is called the fourier transform of x(t).

If we return to equation 4 according to equations 9 and 10,

$$S_{xy}(\omega) = A(\omega) - iB(\omega)$$

and

$$S_{yx}(\omega) = C(\omega) - iD(\omega)$$

where $A(\omega)$, $B(\omega)$, $C(\omega)$ and $D(\omega)$ are real functions of ω.

The amplitude of the any signal is calculated

$$\text{Amplt}^2 = A^2 + B^2 \qquad 11$$

Phase = arctan(B/A)